Spring 5-15-2019

Modeling Mechanisms Behind Force Generation By Actin Polymerization

Seyed Fowad Motahari
Washington University in St. Louis

WASHINGTON UNIVERSITY IN ST. LOUIS

Department of Physics

Dissertation Examination Committee:
Anders Carlsson, Chair
Phillip Bayly
Ram Dixit
Zohar Nussinov
Ralf Wessel

Modeling Mechanisms Behind Force Generation By Actin Polymerization

written by

Fowad Motahari

A dissertation presented to
The Graduate School
of Washington University in
partial fulfillment of the
requirements for the degree
of Doctor of Philosophy

May 2019

Saint Louis, Missouri

Contents

List of Figures

Acknowledgements

I wish to sincerely thank those who made this accomplishment possible for me. I am grateful to the Washington University in St. Louis for providing the opportunity to pursue this degree in an excellent environment. To the Professors on my dissertation committee, I am extremely grateful for their participation, and their instructive suggestions during meetings. To the staff at Physics department, I owe many thanks and appreciations. To my friends and colleagues at Physics department and in St. Louis, I saw myself among a second family in the past several years and for that I am forever grateful to you all. My own family, in spite of the physical distances, had been a source of love, energy, and inspiration; and I am beyond thankful for their everlastingly appreciated support and presence. Lastly, I wish to sincerely thank my advisor, Professor Carlsson, for his invaluable supervision of my training as a doctoral candidate, for the exciting research and knowledge that he familiarized me with, and for the many conversations that he had with me patiently about my career path.

Seyed Fowad Motahari,
Washington University in St. Louis,
May 2019

ABSTRACT OF THE DISSERTATION

Modeling Mechanisms Behind Force Generation By Actin Polymerization

by

Fowad Motahari

Doctor of Philosophy in Physics

Washington University in St. Louis, 2019

Professor Anders Carlsson, Chair

Actin polymerization is the primary mechanism for overcoming the large turgor pressure that opposes endocytosis in yeast. While generation of pushing forces by actin polymerization is fairly well understood, it is not clear how actin polymerization produces pulling forces. In order to understand this process, it is necessary to simulate polymerization of filaments having various types of interactions with the membrane. Since existing methodologies in the literature do not treat such problems correctly, we develop a thermodynamically consistent methodology for treating polymerization of filaments having arbitrary interaction potentials with the membrane. Then I perform stochastic simulations for a system of 144 semiflexible actin filaments in a square array, treating all subunits explicitly. Each filament interacts with the membrane via an interaction potential that has both attractive and repulsive components. The crucial protein Sla2, which binds actin filaments to the membrane, is assumed to slow the growth of the filaments near the array center by having a strongly attractive potential. The (de)polymerization rates are potential-dependent and thus vary with the filament-membrane gap. We model the elasticity of the actin network by linear springs connecting adjacent filaments to each other. The simulation results show that the outer filaments push on the membrane, while the inner filaments pull on it. I calculate the force distribution for various model parameters, including the potential depths, the free filament on- and off-rates, the numbers of fast- and slow-

growing filaments, and the network rigidity. Under the most favorable conditions, the total pulling force is the sum of the stall forces of all the pushing filaments. The filament-membrane detachment occurs for softer gels with weaker central bindings, and it propagates like a crack in brittle regime. The steady-state force distributions are flat over the pulling and pushing regions, indicating the uniform polymerization rates across the pulling and pushing regions after reaching steady-state.

Chapter 1

Introduction

Biopolymers in eukaryotic cells are responsible for creating a cytoplasmic mesh with both viscous and elastic properties. This intracellular network functions as the internal transport system for cargos and organelles, as well as the structural support to sustain and transfer physical forces crucial in many important phenomena. Examples of such phenomena that depend on such force generation include division of a fertilized egg past its single cell stage, cell shape changes during embryonic growth, migration of white blood cells upon invasion of intruding micro-organisms, and membrane deformation and vesicle scission during endocytosis. This thesis describes a particular mechanism of force generation by cytoplasmic meshworks.

1.1 Endocytosis in yeast

Endocytosis is an important cellular mechanism driven by a self-assembled macromolecular machine of over 50 different proteins in tens to hundreds of copies, to internalize extracellular materials packaged into a vesicle that is pinched off after fully entering the cytoplasm. Figure 1.1 shows the stages of progression of the clathrin-mediated endocytosis process in yeast, from the initial formation of the endocytic patch by the arrival of specific coat and adaptor proteins such as Clathrin, Sla2, and Las17, to the inward progression of the membrane regulated by the forces from actin polymerization. Actin monomers in the cytoplasm polymerize to form actin filaments.

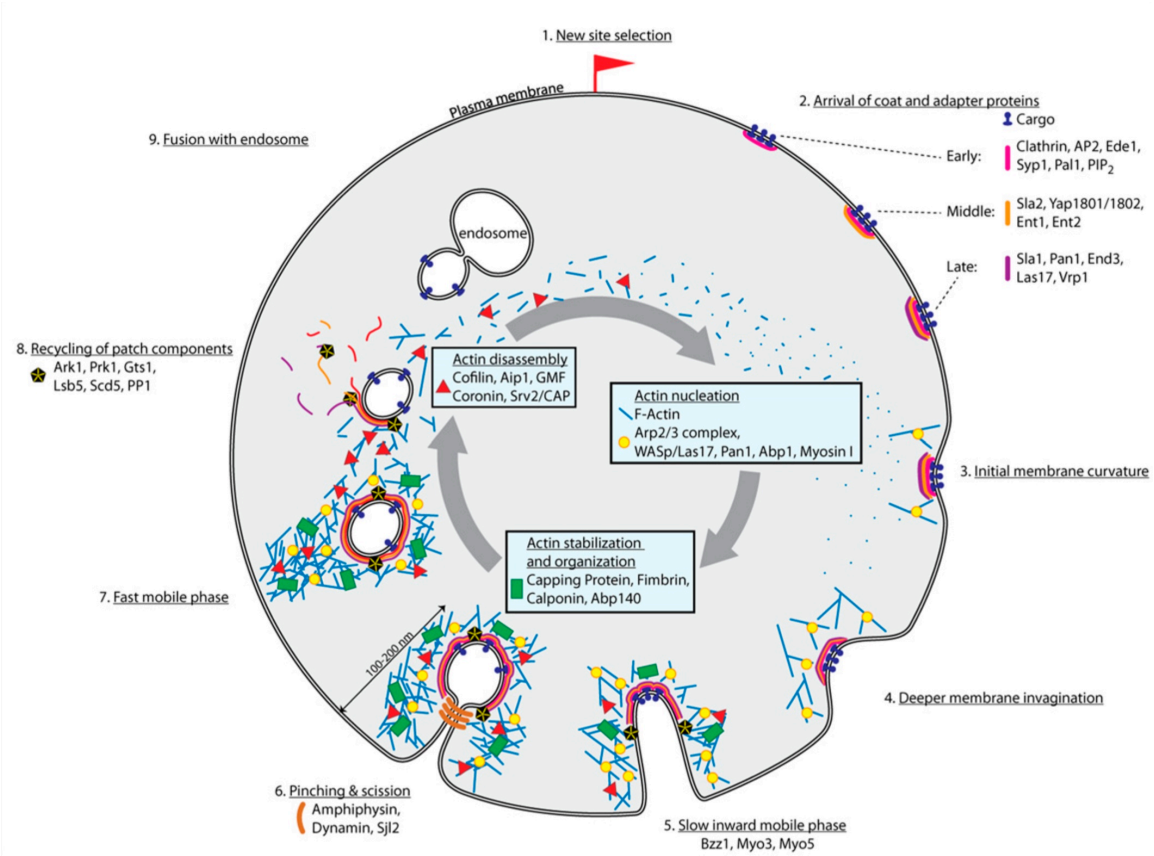

Figure 1.1: Different stages of progression of the endocytic patch, from initial site selection by the arrival of specific coat and adaptor proteins, to the formation of initial curvature and the invagination growth caused by the retrograde motion of the actin network attached to the center of the endocytic patch, followed by scission and uncoating of the internalized vesicle. Figure is taken from Ref. [1].

Polymerization of these actin filaments and their interconnected network growth is known to be required for endocytosis in yeast [1].

In clathrin-mediated endocytosis in yeast, membrane inward deformation requires a power house of protein machinery to produce very large forces at the order of nano-Newtons, to overcome the large outward pushing turgor pressure, the membrane tension, and the membrane bending stiffness at the endocytic site [2]. In mammalian cells, where turgor pressure is small, actin polymerization is still required for endocytosis, in cases of high membrane tension [3, 4] or tight substrate attachments [5].

Actin polymerization is also required for the uptake of viral particles via endocytosis [6, 7, 8]. Trafficking of viral components to the assembly sites is thought to be

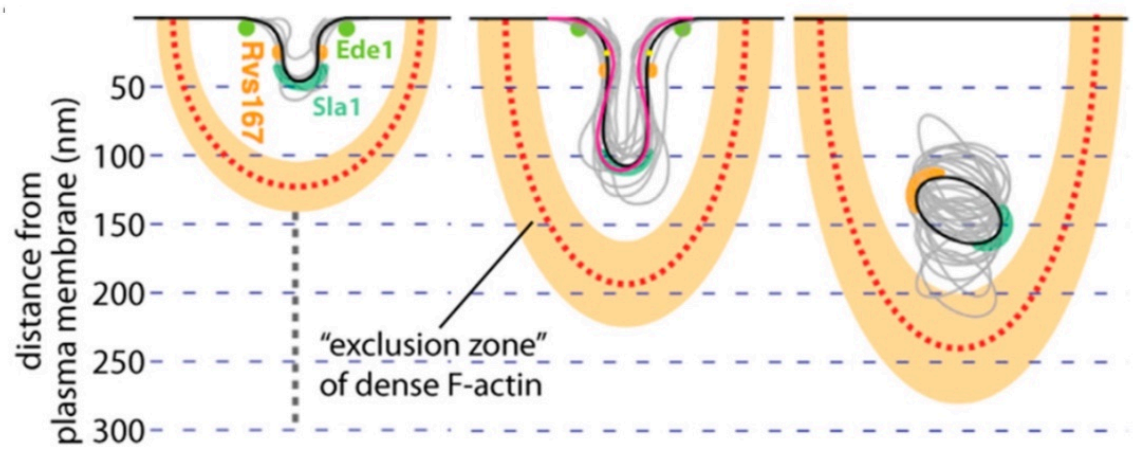

Figure 1.2: Ribosome-free zone surrounding the tip of the invagination indicates actin polymerization in this region. The dashed gray lines indicate the depth of the Ribosome-free zone. Figure is taken from Ref. [1].

affected by the growth and force exertion of the actin network near the plasma membrane [9]. The effect can be both positive and negative; but a clear understanding of the role of the cytoskeleton in various stages of viral assembly is yet to be understood.

A ribosome-free-zone with diameter $\approx 200\ nm$ (Figure 1.2) is observed in time-resolved EM experiments, to surround the plasma membrane invaginations in endocytosis. This zone is where actin filaments polymerize and form a cross-linked actin network. This elastic actin medium can be represented by an "actin gel" with characteristic elasticity parameters (such as Young's modulus), and additionally be treated in discrete analysis with stochastic calculations for every single filament.

Actin filaments grow subunit by subunit. In the presence of an Arp2/3 (Actin Related Protein) complex, branching and nucleation of a new filament from the base (where Arp2/3 is located) can occur. This new filament is called a daughter filament, growing with a constant 70° angle orientation from the direction of its mother filament [10]; see Figure 1.3. It is experimentally shown that actin filaments at endocytic patches form an Arp2/3 branched network that assemble, move, and disassemble rapidly [11]. Figure 1.4 shows an EM image of actin branched network. The endocytic patch is typically 200 nm wide. The average filament length in this typical patch is $\approx 50\ nm$.

Generation of pushing forces by actin polymerization has been observed in many

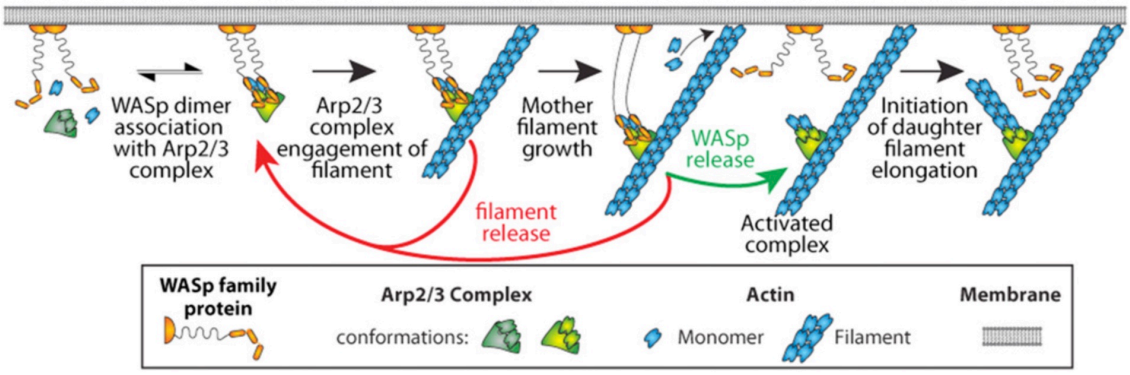

Figure 1.3: Arp2/3 complex in yeast once activated by Las17 (yeast WASp) form new actin filaments (daughter filaments) at a 70° orientation from the existing filament (mother filament). Figure is taken from Ref. [1].

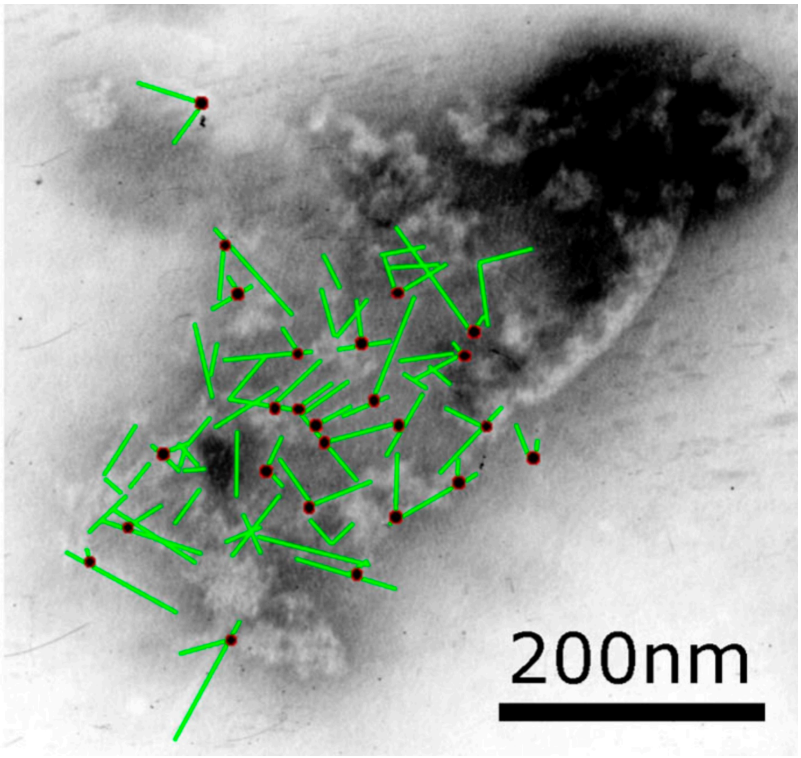

Figure 1.4: Electron microscopy images show that actin filaments in yeast at the endocytic patch form a cross-linked branched network. Green bars highlight actin filaments, forming branches from the location of black dots, the Arp2/3 complex. Figure is taken from Ref. [11].

experiments, and various models exist in the literature that explain the key mechanisms behind pushing force generation. The models are essentially based on the Brownian ratchet model, first described by Peskin et. al in 1993, Ref. [12]. Generation of pulling forces by actin polymerization on the other hand, is not very well-understood. However, recent advancements in microscopy techniques have enabled us to assess different hypotheses to how actin polymerization leads to generation of pulling forces.

1.2 Pushing forces from actin polymerization

In the micrometer scales of the cytoplasmic environment, explaining how object A pushes object B is not as straightforward as explaining real life physical phenomena involving forces. It is possible to find very large forces exerted on cell membrane or vesicles inside the cytoplasm by an ensemble of growing biopolymers with complex interconnectivity and stochastically changing growth rates. Polymerization and depolymerization of actin filaments can generate significant forces in many cellular phenomena in the absence of any associated molecular motors [13, 14].

1.2.1 Actin based pushing forces in experiments

Measurements with real-time fluorescence microscopy of the elongation of actin filaments bound between immobilized formin and myosin molecules [15] shows that polymerization of single actin filament can produce forces of about 1 pN. In these experiments, glass microscope slides are coated with myosin II and budding yeast (Bni1) or fission yeast (Cdc12) molecules. The barbed ends of actin filaments are captured by a single formin that is fixed on the surface of the microscope slide (Figure 1.5). The two ends of the actin filaments are referred to as the "barbed" and "pointed" ends, based on their appearance under transmission electron microscopy, with most actin filaments being arranged with the barbed end toward the cellular membrane and the pointed end toward the cellular interior. Growth is more rapid at the barbed end. Myosin bound to the microscope slide anchored filaments at one

or a few points along their length, leaving both ends free to elongate. The fraction of filaments originating from or captured by an immobilized formin depended on the concentration of formin, but growing filaments rarely dissociated from either budding or fission yeast formin molecules, suggesting that the active immobilized formins are indistinguishable from soluble formins in supporting persistent barbed end elongation.

Barbed ends grow at 10 subunits per second *in vitro* and 100 subunits per second *in vivo* [16]. The authors have also noted that the barbed end elongation rate in the presence of formins is 30-fold higher than the ATP-hydrolysis rate, measured without formin [17]. Therefore the filament tips are ATP-actin. They have also found that capping proteins did not limit the elongation of barbed ends that are captured by immobilized formins, although they did limit the growth of branches formed by Arp2/3 complex. This confirms that formins protect barbed ends from capping protein.

New subunits are inserted at the formin-attached barbed end and the elongation of the buckled actin filament in between formin and myosin molecules allowed for the force determination. The force required to buckle a rod is proportional to its stiffness and inversely proportional to its length squared ($F = \pi^2 \frac{l_p}{k_B T L^2}$, where l_p is the persistence length of the filament, and L is the length of the buckled filament [18]). Therefore, the length of the shortest buckled filament reveals the maximum force produced by actin polymerization. In the experiments done by Kovar and Pollard, in the presence of phalloidin molecules which double the stiffness of the actin filaments, the lengths of the shortest buckled filaments were $\approx 0.75\ \mu m$, corresponding to a polymerization force of $1.3\ pN$, close to the theoretical stall force of $\approx 2\ pN$ under the experimental conditions. The limiting factors for detection of forces greater than $1.3\ pN$ are the flexibility of actin filaments and the temporal and spatial resolutions ($\approx$ 100 subunits) of the microscope. Because this method relies on filament anchoring by the formin protein, it cannot be used to examine force generation by polymerization of actin filaments with free barbed ends, filaments in bundles, or in the presence of other actin-binding molecules that interfere with formin function. It is worth mentioning that microtubules are much stiffer, and measurements of their elongation revealed

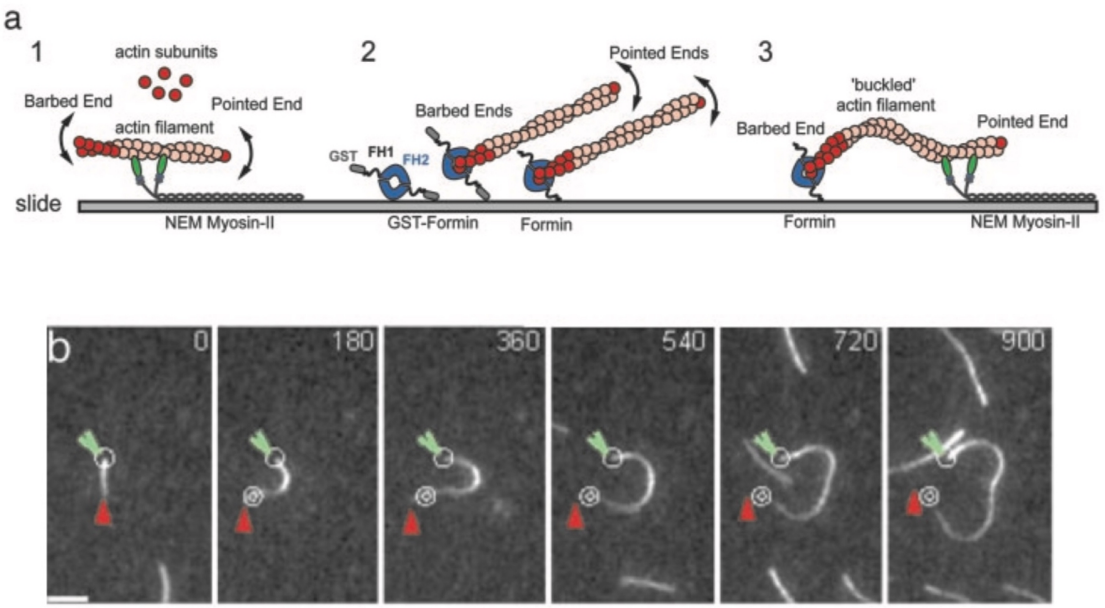

Figure 1.5: a) Diagram of the single-filament force experiments. Glass slides are preincubated with myosin II, binding a single actin filament at one or a few points along its length, and yeast formins binding the barbed end of the actin filament. The length of the buckled filament determines the force produced by actin polymerization. b) Real-time fluorescent microscopy images of the actin filament that is bound between a formin and a myosin molecule. Green wedges indicate barbed ends; white double rings indicate the position of myosin on the surface of the microscope slide; red triangles indicate the pointed ends. Time in seconds indicated at the top. Scale bar is 5 μm. Figure is adapted from Ref. [15].

polymerization forces up to 10 pN [19, 20].

Generation of pushing forces by polymerization of ensemble of actin filaments is also well observed in a variety of *in vivo* and *in vitro* experiments. One of the most evident examples of propulsion in cellular scales driven by actin polymerization is the motion of the bacterium Listeria inside the cytoplasm. Listeria is an example of an intracellular parasite that is transmitted from cell to cell without ever leaving the host's cytoplasm. Its motion is driven by the growth of a long actin "comet" tail, which can exceed 5 μm in length and 1 μm in width [21]. The fact that actin polymerization is able to generate very large propulsive forces allows the bacterium to penetrate through the membrane of the donor host's into the new host's cell. Figure 1.6 (left) shows a schematic of the motion of the bacterium at different stages of entry and propulsion by an actin comet tail, and on the right an electron microscopy snapshot of the branched network of actin filaments forming a comet tail and polymerizing at the rear end of Listeria to push it through the cytoplasm. The actin filaments initially surround the Listeria, to separate it from the formed elements of the cytoplasm of the host, then become organized into an array that extends from only one end of the Listeria instead of surrounding it. From higher resolution images, the authors concluded that the tightly packed actin mesh is composed mostly of short and relatively rigid filaments that are in random orientations. In this paper published in 1989, the authors did not report the magnitude of the pushing forces produced by actin polymerization, generally because of the difficulty of counting the number of filaments in an image with limited resolution.

Using optical traps for direct measurements of elongation of a bundle of growing filaments has also allowed quantitative force measurements. They showed that approximately eight parallel-growing filaments can exert forces on the order of $1pN$ before stalling [22]. The estimated effective actin elongation rate constant in these experiments for various actin concentrations (1, 2, and 4 μM) is 2.6 monomers $\mu M^{-1} sec^{-1}$. The measured pushing forces of about $1pN$ correspond to those expected for single filaments, but in the experiments shown in Figure 1.7 that mimic the geometry of filopodial protrusion, for a higher concentration of actin, eight parallel-growing

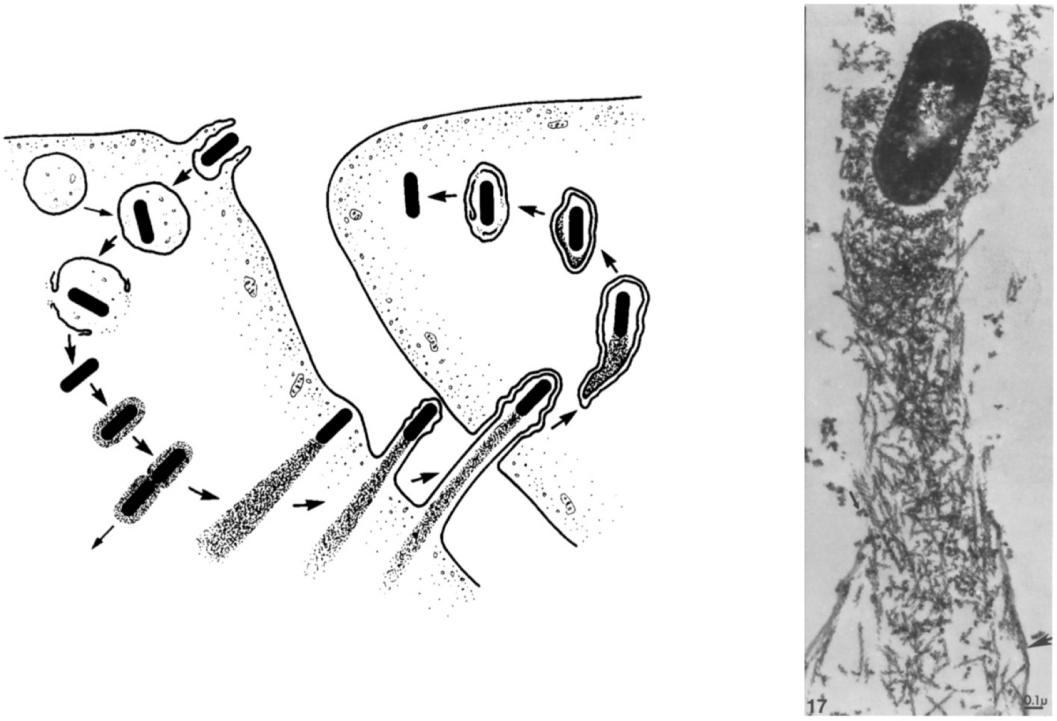

Figure 1.6: On left, a schematic of different stages in the motion of Listeria inside cytoplasm propelled by actin polymerization. On right, electron microscopy image of the actin comet tail forming a branched network of filaments growing at the rear end of the bacterium. Figure is adapted from Ref. [21].

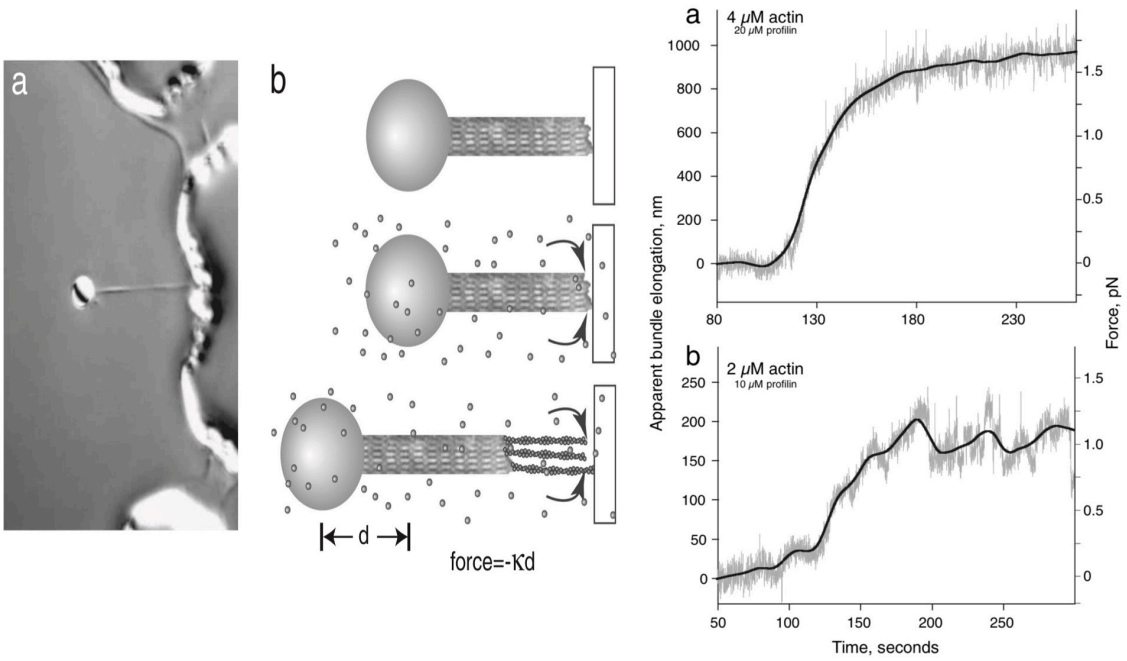

Figure 1.7: Force measurements using optical traps to observe elongation of small number of parallel-growing actin filaments in a bundle. The elongation of the bundle of filaments determines the magnitude of the exerted force on the bead. Figures on the right side show that over a range of actin concentrations, forces on the order of 1 pN are generated by six to eight parallel-growing filaments. The higher the actin concentration, the longer the elongation of the bundle, and thus the measured forces in the stall phase. Figure is adapted from Ref. [22].

filaments are brought into apposition with a rigid wall, polymerizing at the end in vicinity of the wall and pushing the bead at the other end. Large length fluctuations during the stall phase, that can be seen in Figure 1.7 on the right side, suggest that only the longest actin filaments at any given time are in contact with the barrier. The small magnitude of the force is consistent with these findings, suggesting that generation of larger pushing forces by actin polymerization in living cells requires "load-sharing" between growing filaments, to protect growing filaments from depolymerizing [23, 22, 24].

In other experiments, observing growing actin networks *in vitro* using atomic force microscopy (Figure 1.8) has revealed the presence of a load-independent growth phase, where the actin network grew at a velocity of $\approx 72\ nm/min$ over a 50-160-nN range,

followed by a stalling phase, where the rate of network elongation slowed until a complete stall at a force of $\approx 294\ nN$, corresponding to an actin pressure of $\approx 10^{-3}$ pN/nm^2. The authors with a mechanical stall test affirmed that the stall was induced by force and was not due to depletion of actin or other proteins contributing to the network growth. The load-independent growth phase before stalling can be explained by an increase in the actin filament density to sustain a constant force per filament during this phase. This explanation stems from the hypothesis of an auto-catalytic mechanism for filament formation, where filament density is governed by the load and adjusts to prevent changes in velocity as force increases or decreases [25]. Several molecular mechanisms might be responsible for regulating filament density, such as force-dependent branching or capping rates. The observed load-independent growth phase also suggests that an optimum-force range exists in which crawling cells may operate for robust, stable movement.

The authors have also concluded that the force-velocity (FV) relation of a branched actin network in vitro depends on the loading history, unlike the FV relation for individual filaments. To further examine this hypothesis, they performed force-clamp-reduction experiments (Figure 1.9). The results revealed that multiple steady-state growth velocities are possible at a given load, proving that a single FV relation can not fully describe the behavior of a branched actin network *in vitro*. In moving cells, remodeling of the actin network as a result of load may enable immediate cytoskeletal responses to physical obstacles, independent of chemical signaling. The authors mentioned that further experiments will be required to elucidate the specific molecular mechanisms involved in remodeling and hysteresis.

Among other evidences for actin pushing forces in cell motility are the progression of cross-linked lamellipodia networks and fingerlike filopodium protrusions of unbranched parallel filaments at the edge of the plasma membrane in the cell migration processes (see Fig. 1.10). The lamellipodium of the moving cell is a quasi-two-dimensional actin network formed via the assembly of filaments beneath the leading edge membrane. In lamellipodia, actin polymerization is found to be crucial for generating forces in the order of nN, to deform the plasma membrane [27]. The

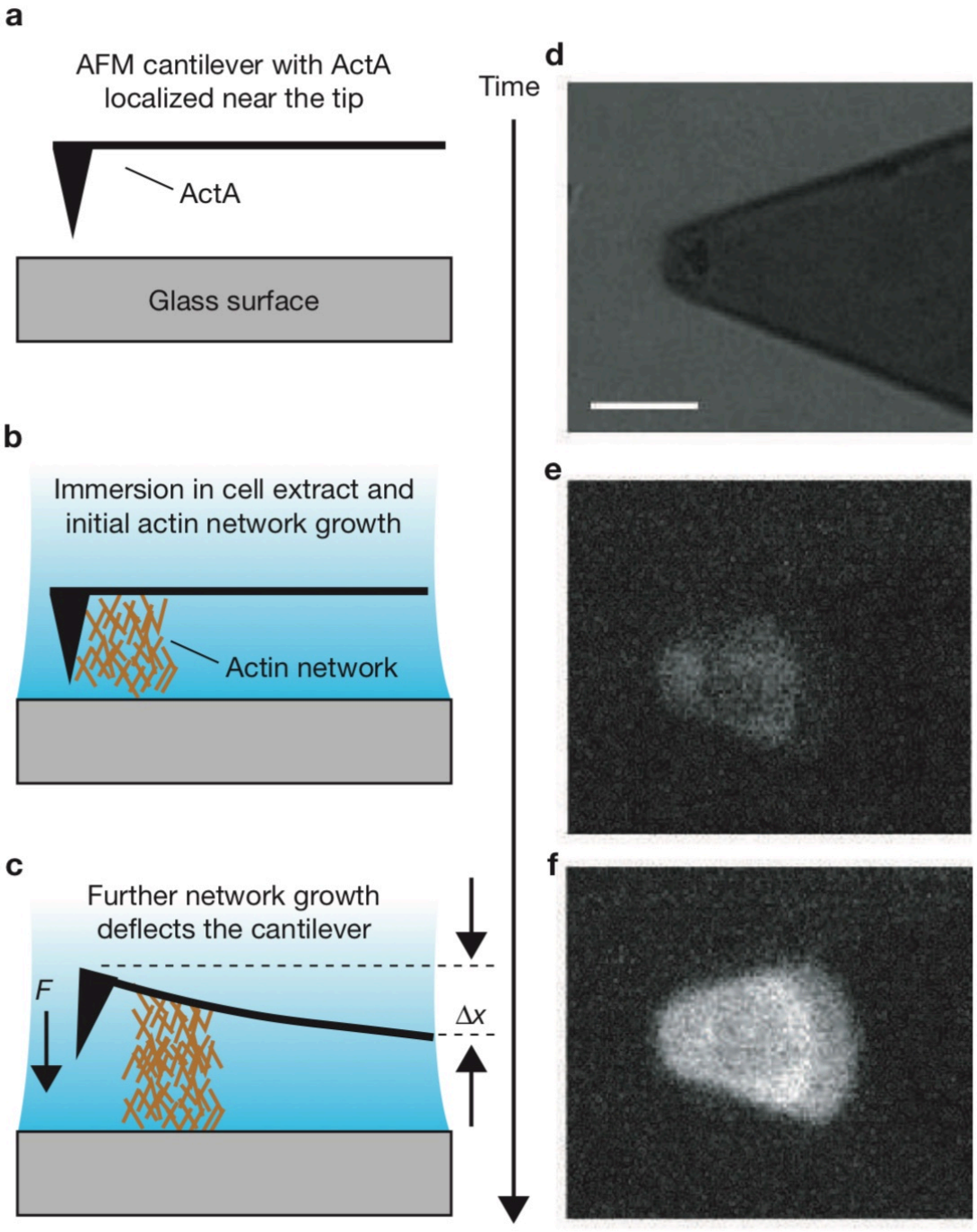

Figure 1.8: Measurements of force generation from growing branched actin network *in vitro*. The tip of the cantilever is preincubated with actin assembly-inducing proteins, ActA. Nanometer deflections of the cantilever tip position caused by network growth can be detected in this AFM set-up. On the right side, fluorescence micrographs show the growth of the actin network. Scale bar is 10 μm. Figure is taken from Ref. [26].

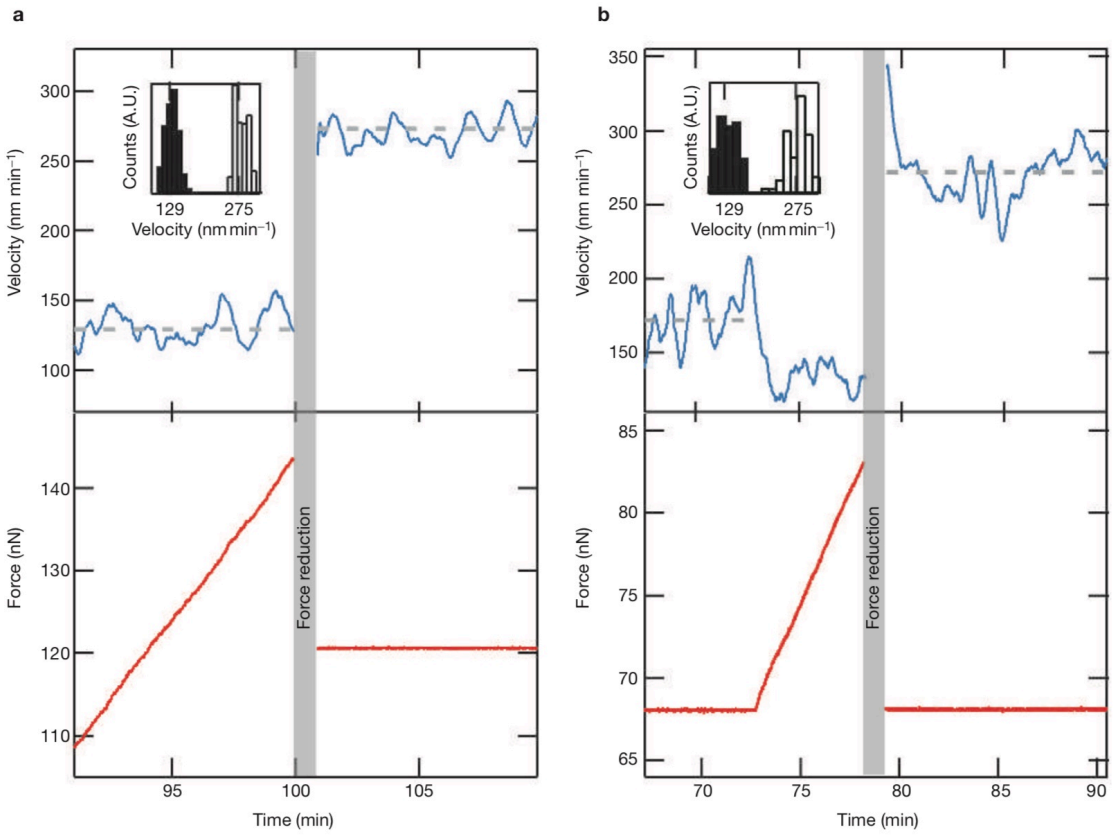

Figure 1.9: Force-clamp-reduction experiments demonstrate multiple stable growth velocities for a single load on the network. In a), the system is at the load-independent phase and is growing with an average velocity of 129 nm/min for 100 min with the force being increased gradually. Force is then immediately reduced to a previously exerted value, and the system is observed to enter a similar load-independent phase with a different growth velocity of 275 nm/min. In b), the force-reduction step is performed at the stall phase of the network development, in which increasing the force decreases the growth velocity, but similarly two steady-state growth velocities are measured at a single force of $\approx$ 68 nN, before and after force-reduction step. Figure is adapted from Ref. [26].

maximal force necessary to stall the whole body of a moving cell is on the order of 35 nN. The stall pressure necessary to stop lamellipodium extension is on the order of 3×10^{-3} pN/nm^2, on the same order of magnitude as the force density generated by actin polymerization resulting from Arp2/3 complex activation on micro-metric beads [28, 29, 30].

Capping protein (CP) is a protein which binds to the fast-growing end of actin filaments, thereby blocking the polymerization and depolymerization of actin subunits at these ends. In the absence of capping proteins, actin filaments grow longer and can align into a parallel bundle organization. These parallel filaments form stable finger-like filopodial protrusions with a role in cell migration and sensing the cell environment, as well as transmitting cell to cell signals. In these structures, the growing barbed ends of the filaments face the leading edge of the membrane, making it possible to exert pushing forces with their polymerization. This orientation is due to the presence of formins at the tip of the filopodia complex which nucleate actin filaments. Short stiff bundles of filaments tend to stay straight as they apply a force against a load, whereas long actin bundles have a tendency to buckle and deform instead of maintaining an increasing force against a load [31, 32]. Direct measurements of the force generated by filopodia using beads coated by attachment proteins, coupled with an optical tweezer set-up, revealed that the force exerted by a retracting filopodia is on the order of 10 pN and works over a distance of 10 μm [33, 34]. Myosin motors and microtubules are not required for filopodia retraction, and in some cases, their mechanics appear to rely on actin assembly and actin dynamics solely [35], but there are other cases as well where filopodial retrograde flow is influenced by the activity of myosin-type motors [36, 37, 38].

1.2.2 Ratchet models that describe the pushing forces

When actin filaments elongate in close proximity to a biological load, they are believed to generate pushing forces through a ratcheting mechanism where thermal fluctuations allow for periodic insertion of new actin subunits in the filament, despite the presence of a counteracting load force [12, 39]. Thermodynamical calculations of force

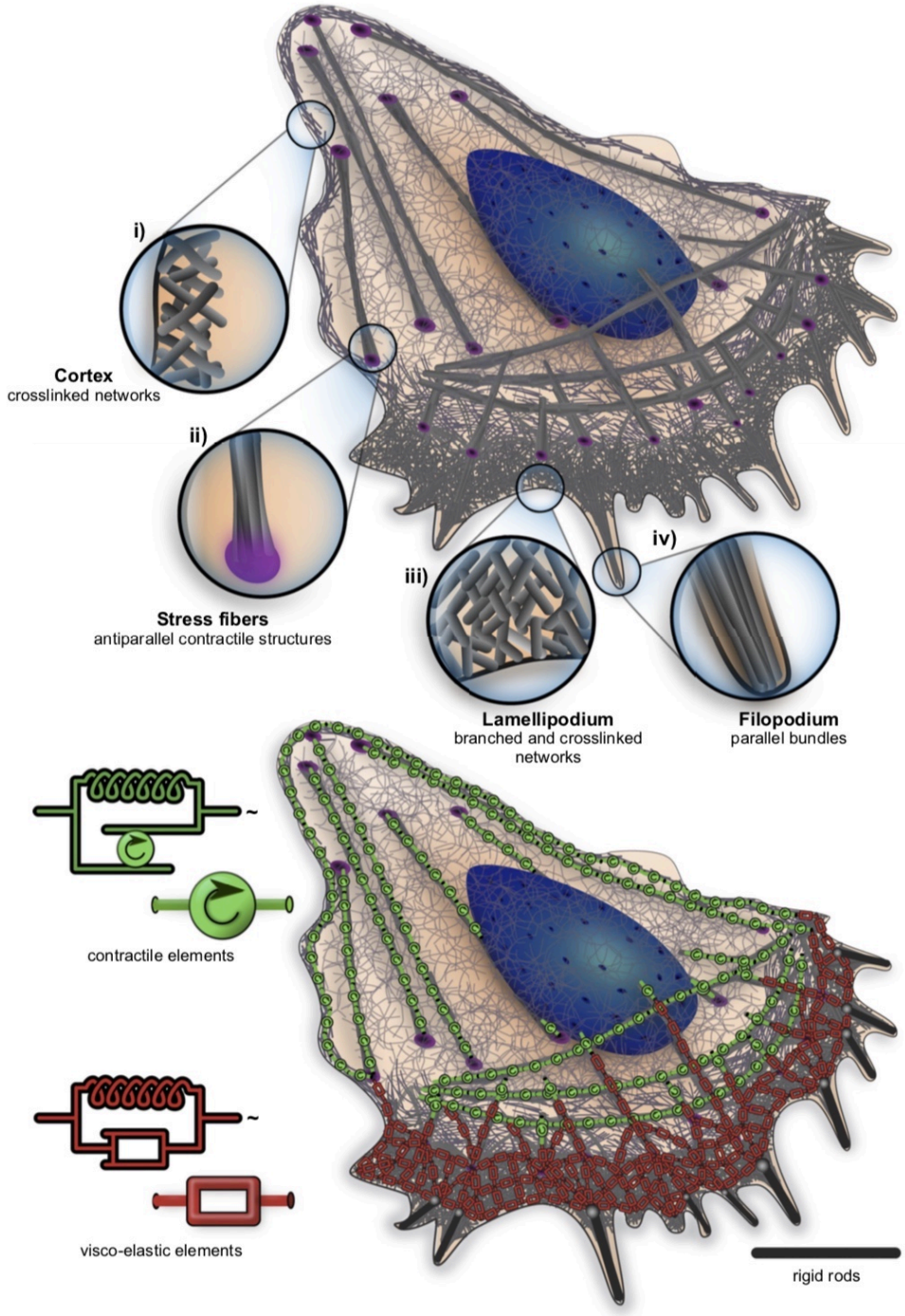

Figure 1.10: Cross-linked actin network in the lamellipodia and protrusion of parallel-growing filaments in the filopodia are among other evidences of pushing forces generated by actin polymerization in living cells. The zoomed regions indicate architectural properties of different regions of the cell, with an overlay of their mechanical profile. The 2D network of branched actin filaments in lamellipodia form a viscoelastic medium, while the filopodia protrusions are more accurately described as rigid rod extensions. Figure is adapted from Ref. [27].

generation by actin filament polymerization via this mechanism [40, 12] predict that filament growth should slow and eventually stall as the applied force on the growing end of the filament approaches the value determined by:

$$F_{stall} = \frac{k_B T}{\delta} ln(\frac{A \cdot k_{on}^0}{k_{off}^0}), \tag{1.1}$$

where k_B is Boltzmann's constant, T is the absolute temperature, δ is the step size for addition of a single actin subunit ($2.7\ nm$), A is the concentration of actin monomers in the solution, and k_{on}^0 and k_{off}^0 are the rate constants for polymerization and depolymerization of a free actin filament, respectively.

The classic Brownian ratchet (BR) model [12] gives an explanation of how the free energy of polymerization is transduced into directed mechanical force. As the obstacle position fluctuates over time, occasionally a gap large enough to insert a new subunit appears. This model estimates the growth velocity of a polymerizing biopolymer:

$$v_{growth} = \delta[A \cdot k_{on}^0 \exp(-F_{ext}\delta/k_B T) - k_{off}^0], \tag{1.2}$$

where F_{ext} is the load on the obstacle. Figure 1.11 shows the force-velocity curve for such polymerization ratchet process [12]. The actin filament polymerizes against a rigid wall having a diffusion constant D, with an external force F_{ext} (showed by f in Fig. 1.11) exerted on the wall. The solid line represents the FV curve when depolymerization is negligible. The dashed line is valid when polymerization is much slower than obstacle diffusion, which is the case in most living cell processes.

In all of the experiments that we discussed above, if the distance between the edge of the actin network and the surface of the object opposing the network is large enough for a non-zero chance of further network growth, given enough time the object will be pushed as a result of actin polymerization. This general mechanism is at the core of further ratchet models explaining the actin pushing forces. There have been a number of follow up models, improving upon some simple assumptions in BR model. For example, in the Elastic BR model [41], the assumption of rigidity of actin filaments is removed; therefore thermal motions of filament tip are also explicitly treated. The

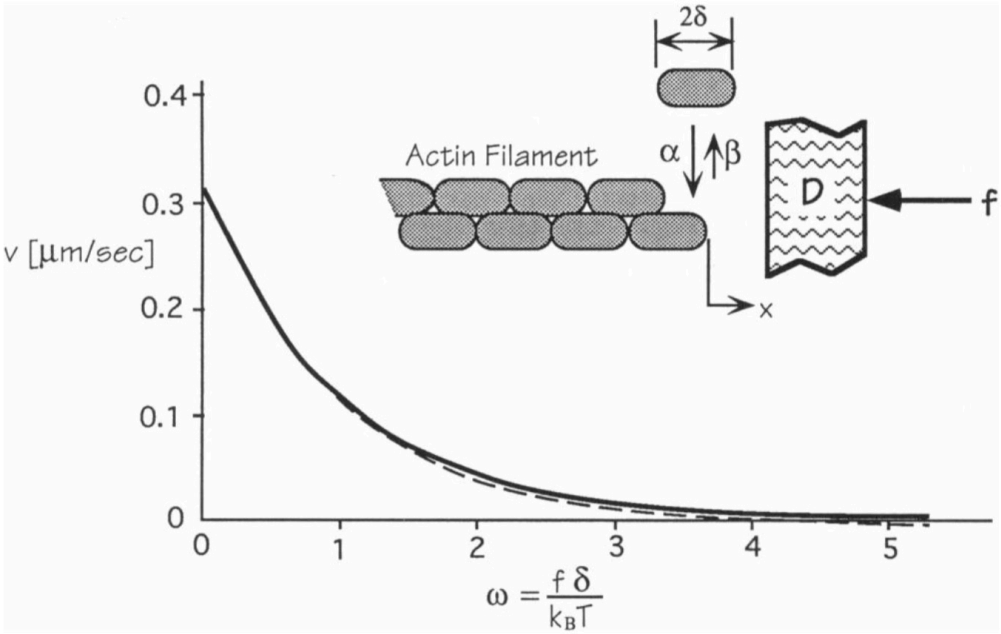

Figure 1.11: Force-velocity curve for a ratchet polymerization mechanism. Solid line (analytical theory) represents the case where depolymerization is zero, and dashed line (numerical calculations) is for the case of rapid obstacle diffusion, compared with polymerization rate. Parameter values for Eq. 1.2 used to generate this curve are Figure is taken from [12] and are as follows: $A = 10\mu M$, $k_{on}^0 = 11.3sec^{-1}\mu M^{-1}$, $k_{off}^0 = 1.6sec^{-1}$, and $\delta = 2.7nm$. The authors chose $D = 10^5 nm^2/sec$ in their numerical calculations. The stall force for a single actin filament with this choice of parameters is $\approx 7.8\ pN$. Figure is taken from Ref. [12].

effect of tethering filament tips to obstacle on the growth rate is also included in this model. That for example, results in force-velocity curves that match the experimental data for Listeria more accurately. In another study, a model for the growth of multiple filaments which expands on BR model is developed [42]. The model stochastically treats the polymerizing ensemble of rigid parallel filaments growing against a hard diffusing obstacle. In this model, the effects of ATP hydrolysis (hydrolysis of ATP-actin to ADP-actin) on force generation by actin polymerization are studied. The results show that by lowering the concentration of free actin monomers, the pushing force from the obstacle forces the filaments to enter a depolymerizing state, suggesting that at any given time, only a small number of filaments contact the obstacle [42].

In the next section, we move onto discussing the experiments and models that explain the mechanisms behind the generation of pulling forces via the growth of actin networks in cellular processes.

1.3 Intracellular actin based pulling forces

Pulling the cell membrane inward relies on actin polymerization in several types of cellular processes, including endocytosis, phagocytosis, and uptake of large viruses. As the opposing force against the membrane invagination becomes higher, the role of actin polymerization becomes more crucial. An example of such a phenomenon is endocytosis in yeast, where the turgor pressure is higher, relative to mammalian cells. In this section, to discuss the mechanisms behind the generation of actin pulling forces, we first review the experiments with quantitative analysis of actin pulling force distributions around biological structures, such as lipid vesicles and podosomes. Next, we review the experimental evidences for actin pulling forces in endocytosis, provided by recent microscopy advancements that made clear the temporal and spatial molecular composition at the endocytic sites. We end this section by reviewing the existing hypotheses on how actin polymerization is capable of generating large pulling forces to drive the membrane invagination in endocytosis.

Pathogenic bacteria, viruses, and endocytic vesicles that use actin polymerization-

based mechanisms for motility are associated with a characteristic actin "comet tail' structure, which consists of a large number of actin filaments crosslinked in a dendritic meshwork [21, 43]. In experiments that simulate the motion of Listeria *in vitro* [44] (see Figure 1.12), the authors examined the magnitude and distributions of actin polymerization forces that propel large artificial lipid vesicles (beads coated with lipid monolayers) preincubated with ActA (actin nucleating proteins found on the surface of Listeria). ActA on the surface of these fluid vesicles at saturated amounts ($\approx 10^7$ molecules per bead) directly activates Arp2/3 complex [44], whereas endocytic vesicles have more indirect Arp2/3 activation mechanisms that require the presence of other actin nucleation promoting factors [45]. ActA in these experiments is shown to mostly accumulate at the rear end of the vesicles. Since ActA binds indirectly to actin filaments via VASP and the Arp2/3 complex [46], this asymmetry in ActA spatial distribution on the vesicle surface suggest that actin-dependent ActA polarization contributes to inducing a persistent asymmetry of actin filament density on the vesicle surface and thus reinforcing persistent unidirectional motion over time. The ActA binding to F-actin also allows filaments to exert pulling forces on the vesicle. By localizing any of several different Arp2/3-activating factors to generate the formation of actin comet tails, the authors confirmed that regardless of the specific identity of the surface nucleation factors, it is the force exerted by the organized network of actin filaments that propels the vesicles. These lipid vesicles, when propelled by actin polymerization in a cytoplasmic extract, deform and elongate from the rear end, where actin tail is growing (Figure 1.12), suggesting the existence of inward compressional forces on the sides, along with the pulling forces opposite to the direction of motion at the rear end. The total net compressional force is >10 times larger in magnitude than the total net pulling force. The total volume of most vesicles decreased slowly over time, presumably as water was squeezed out through the semipermeable lipid bilayer, further solidifying the suggested actin force distribution picture.

Since the mechanical properties of the artificial phospholipid vesicles were well characterized, the authors were able to use the information on vesicle deformations to directly calculate the distribution of the forces acting on the vesicle surfaces. Be-

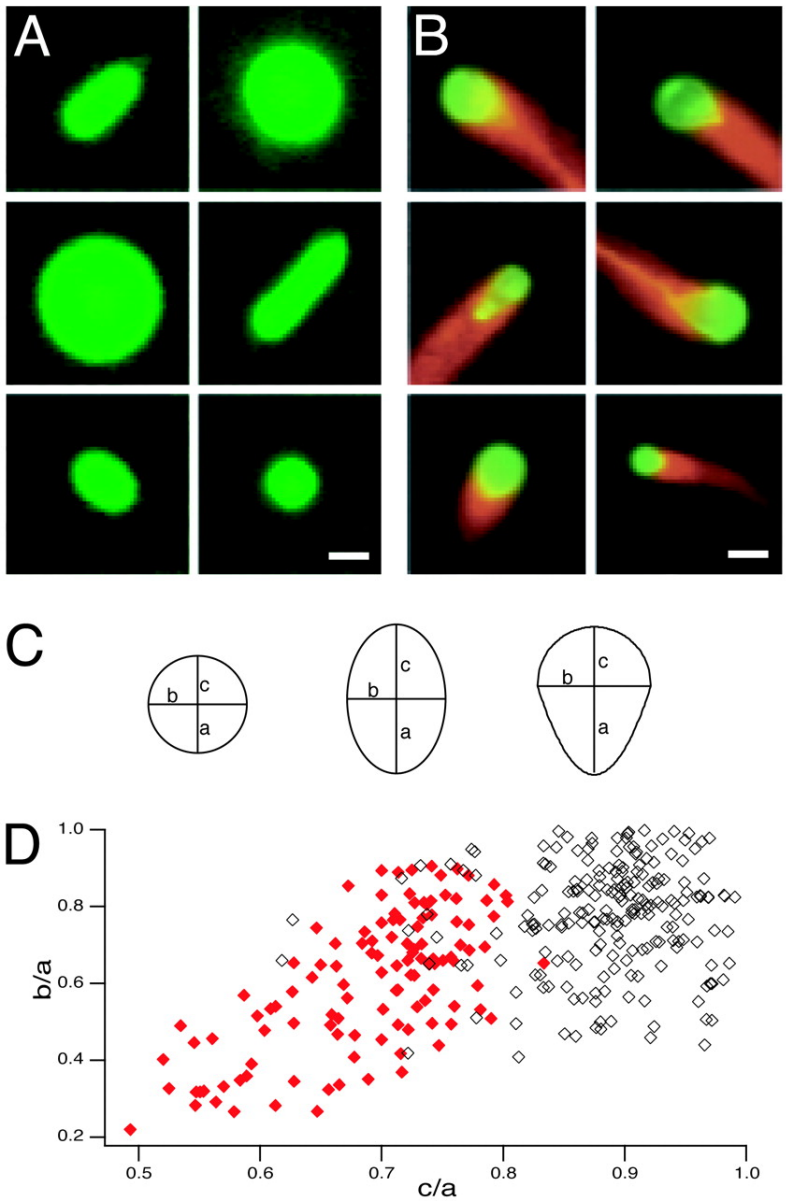

Figure 1.12: Experiments on fluid vesicles coated with ActA, propelled in cytoplasmic extracts by actin polymerization. **A** Control vesicles not coated with ActA, showing no deformation as a result of actin polymerization forces, **B** Vesicles coated with ActA. The compressional forces on the side along with the retarding forces at the rear of the vesicles cause significant deformations in their shape along the direction of motion. The vesicles range in size from a few hundred nanometers to tens of micrometers. Similarly prepared control vesicles not coated with ActA (and therefore not associated with actin) mostly maintained a symmetrical spherical shape in cytoplasmic extract. **C** and **D** Quantitative analysis of the shape distortion (plot on the bottom of the figure) show a clear separation in classification of the actin-associated vesicles (red diamonds) and the control ones (black diamonds). Figure is taken from Ref. [44].

cause the vesicle shapes and actin distributions changed slowly over time, the authors assumed that the systems are thermodynamically quasi-static, indicating that external force densities balanced the internal pressure and other force components at every point on the surface at any given time. In a quasi-static system, given the fact that the hydrodynamic drag for these large beads is negligible, the internal turgor pressure (which is constant everywhere on the surface) balances out the external pressure due to membrane tension and actin compressional and retarding forces at every position (the forces induced by membrane curvature were ignored). The factors contributing to balancing the turgor pressure vary with position along the membrane, so by calculating the spatial distribution of pressure due to membrane tension that varies inversely with surface curvature, one can readily find the actin pressure distribution. Figures 1.13C and 1.13D show the calculated actin pressure distribution and magnitude, in terms of multiples of membrane tension (γ), which is assumed to be constant around the vesicle. The prediction of this quasi-static model for the actin force distribution is consistent with the tear-drop distorted vesicle shapes; net inward pushing forces on the sides along with net retarding pulling forces at the rear. This analysis also suggests that the actin pressure normal to the vesicle surface (see Fig. 1.13C) is not uniquely determined by the actin filament density, despite the prediction of most simple biophysical models [40, 12, 39]. This might be due to the spatial variations in actin filament length and density in the comet tail, as well as their random orientation. The ratio between numbers of attached and unattached filaments is also believed to affect the magnitude of the net actin force [41].

The magnitude of the actin pressure can be obtained from an estimate of the membrane tension; knowing the material properties of the artificial phospholipid vesicles, $\gamma = 0.01 - 0.1 mN/m$ is the estimated range for the membrane tension. Given that estimate, the authors concluded that maintaining the distorted shape of these fluid vesicles requires a minimum total compressive force from actin in the range of $\approx 0.4 - 4\ nN$. Calculations considering all net normal actin pressure also show that more than 90% of the force is used to compress the vesicle, and the remaining force is supplied along the direction of motion. Fig. 1.13D shows that the maximum actin

pulling pressure (in units of $nN/\mu m^2$) at the rear is ≈ 3.5 times the membrane tension divided by the mean radius of the vesicle on the y-axis ($\approx 1.5\mu m$). Given the maximum membrane tension $\gamma = 0.1\, mN/m$, the maximum actin pressure is $\approx 2.5 \times 10^{-4}$ pN/nm^2. These estimates of actin forces are compromised in accuracy, due to the assumption of constant membrane tension over time, as the vesicles are increasingly distorted. Nonetheless, the prediction of nN range of actin forces is consistent with other theoretical and experimental analysis.

Another example of experiments that display simultaneous existence of pushing and pulling forces by actin polymerization involve measurements of force around podosomes. Podosomes are mechanosensitive adhesion cell structures that exert protrusive forces onto the extracellular environment. Experiments using atomic force microscopy [47] show that protrusive forces from actin polymerization at the core of a single podosome and pulling forces from lateral acto-myosin contractility in the adhesion ring that surrounds the core lead to the substrate deformation at the podosome site. Figure 1.14 shows the AFM images of podosome induced deformations onto the surface of a polymer substrate (known as Formvar membranes). Profiles of vertical deflections and heights are imaged by AFM in contact mode. With a model used for numerical simulations of substrate deformation due to a core of actin point pushing force surrounded by a ring of actin pulling force (Fig. 1.14d), the authors calculated the protrusive forces as a function of podosome geometrical parameters (see captions of Fig. 1.14). These calculations yielded a mean force value of 10.4 nN for actin protrusive forces, using experimental topography data from 59 macrophage cells plated on a 30 nm-thick substrate. Since the quantification of deformation height used in force calculations relies on the measurements of the ring radius value, this quantity had to be measured each time the experimental conditions were changed notably.

The nature of pushing and pulling forces during endocytosis is becoming clearer. In order to reach a better mechanistic understanding of the process, data from live-cell imaging of fluorescently tagged endocytic proteins were linked with information on the membrane shape from electron tomography at each stage in the process [48] (Figure 1.15). In these experiments, in addition to identification of temporal sequence during

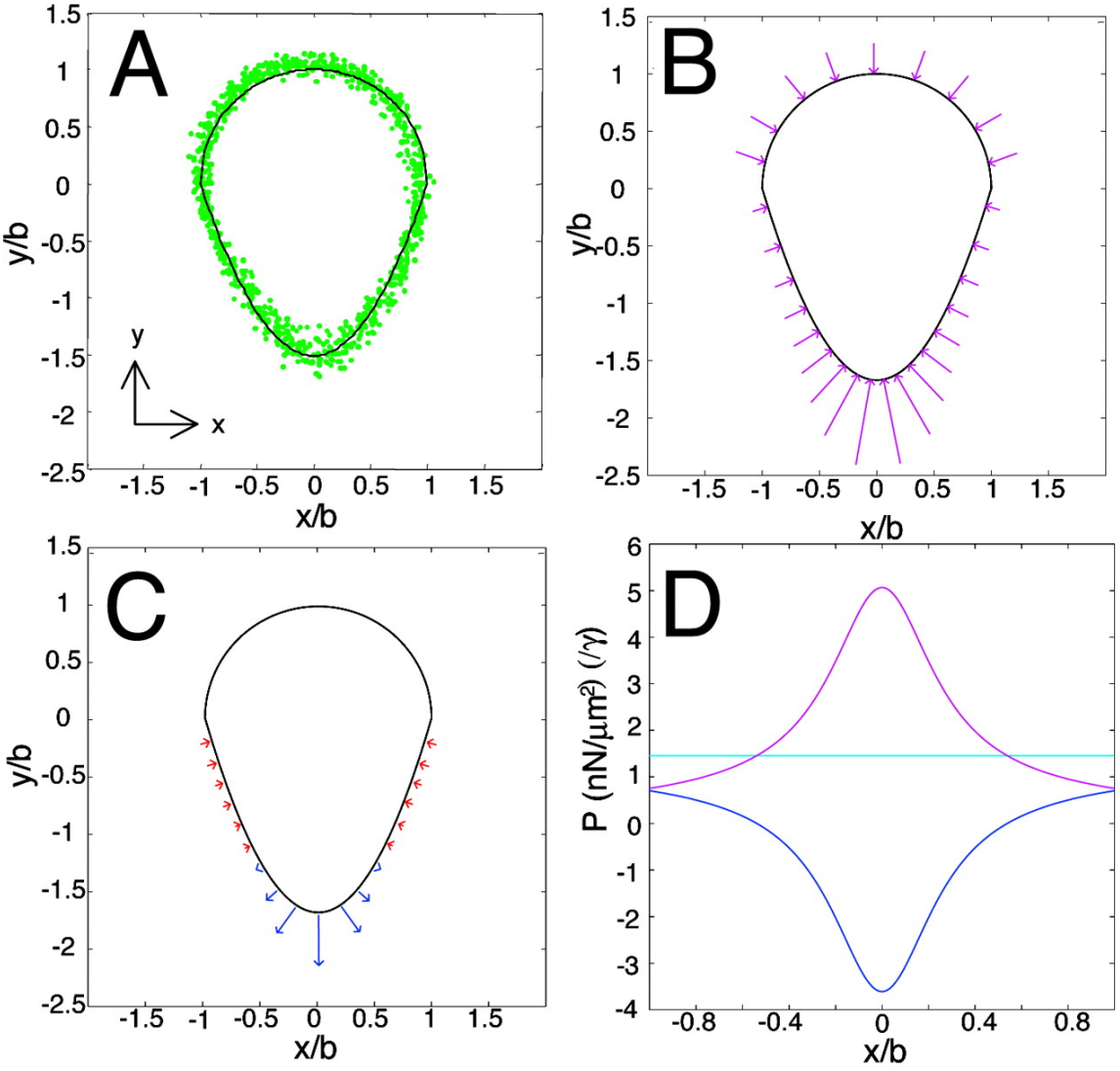

Figure 1.13: Predictions of a quasi-static model for the actin force distribution and magnitude around the surface of the distorted vesicles. Green circles in **A** show the distribution of fluorescently labeled actin on the fluid surface. Panel **B** shows the pressure due to membrane tension, and **C** the net actin pressure (pushing minus pulling). Net actin pushing forces on the side, along with net retarding pulling forces at the rear, are indicated with positive and negative actin pressure in **C**. In **D**, pressure distribution around the lipid vesicles with their magnitude as multiples of membrane tension (γ) for membrane tension pressure (magenta), turgor pressure (cyan), and actin pressure (blue) is depicted. γ has units of mN/m. Figure is taken from Ref. [44].

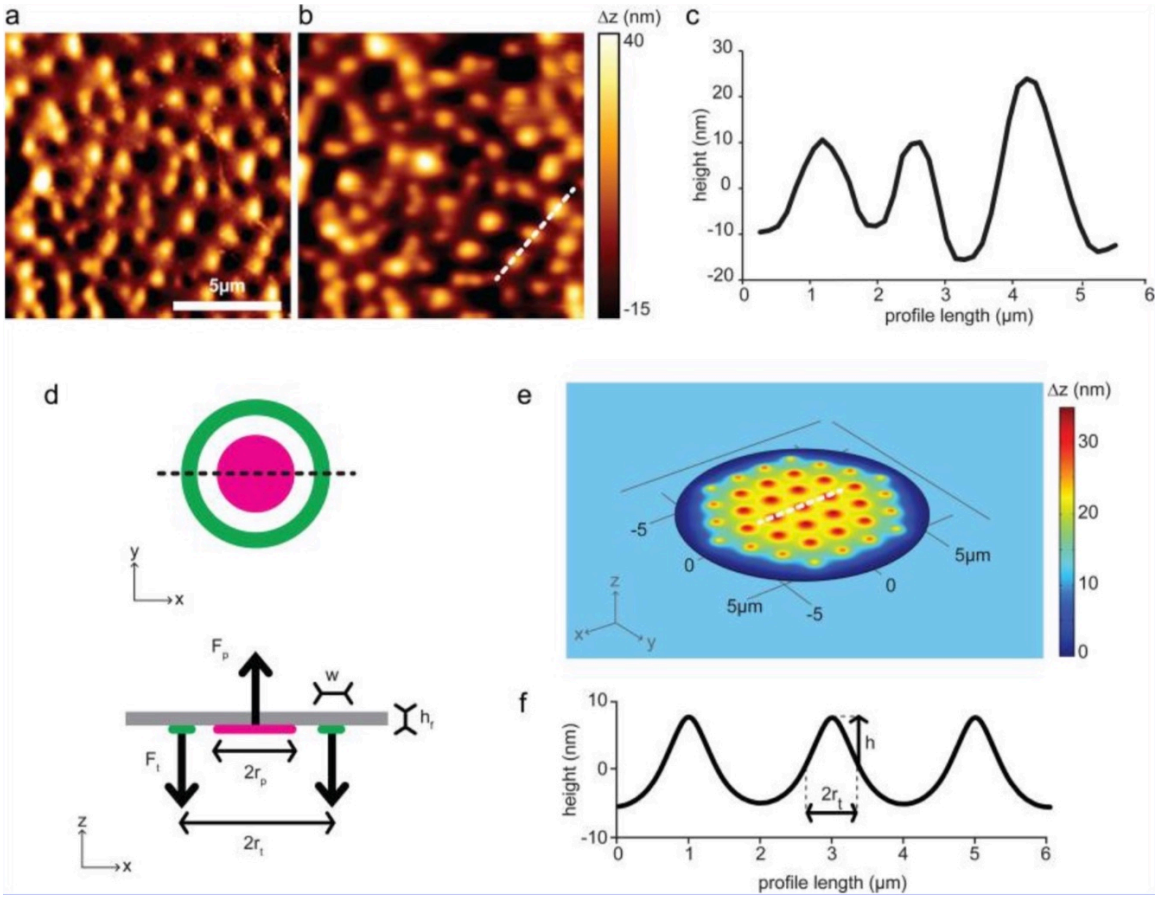

Figure 1.14: Deformations on the surface of the substrate induced by podosome protrusive forces, imaged by atomic force microscopy. Frame **a** is the vertical deflection, **b** the height, and **c** the height profile of the dotted line in **b**. These profiles are then used in numerical simulations to calculate force from geometrical parameters shown in panel **d**. To obtain force values from experimental deformation height measurements, the authors also measured the actual mean values of the relevant geometrical parameters: ring radius = 350 nm, core radius = 140 nm, and membrane thickness = 30 nm. Figure is taken from Ref. [47].

the average endocytic event in yeast, changes in membrane curvature were observed to be correlated with the presence or absence of particular proteins. Figure 1.16 shows the results of fluorescent microscopy measurements for the temporal order and length of the time windows of different tagged proteins, as well as the percentage of the observations via electron microscopy for various membrane deformation stages. Abp1, a component of the actin module, was chosen as a proxy for polymerized-actin and was tagged with mCherry. The lengths of the time windows vary between endocytic sites, but their temporal order is consistent. Upon the initiation of actin polymerization that is identified by the arrival of Abp1 (time window 3), more than 99% of the endocytic sites showed either an invagination or a vesicle. Additionally, membrane curvature is not initiated before the arrival of actin, at the point when only curvature generating coat proteins are present. This confirms the hypothesis that although clathrin arrives at the endocytic patch before actin to bend the membrane initially, the forces exerted on the membrane by the clathrin structure only are not enough to generate invagination against the turgor pressure. The authors have also reported that by using Latrunculin A, an actin polymerization inhibitor, patches of early coat proteins such as Sla1 remained immobile, and distinct Abp1 patches were absent, indicating that actin patches were not formed and coat internalization could not occur. This discovery is of crucial importance for modeling mechanisms of actin pulling force generations in endocytosis; since actin polymerization is confirmed to be the major contributor in generating force to overcome internal turgor.

Time-resolved electron microscopy also revealed that a ribosome-free zone, of diameter $\approx$ 200 nm, surrounds the endocytic invagination [48] (Figure 1.2). This ribosome-free zone indicates the presence of polymerized actin, and thus it is where the elastic actin network (actin gel) is growing. The retrograde motion of the growing actin network, when accompanied by the filament-membrane attachments provided by coat proteins such as Sla2, is believed to pull the membrane inward to form the invagination tubules.

In recent experiments, super-resolution microscopy images made it possible to reconstruct the nanoscale structural organization of 23 endocytic proteins from over

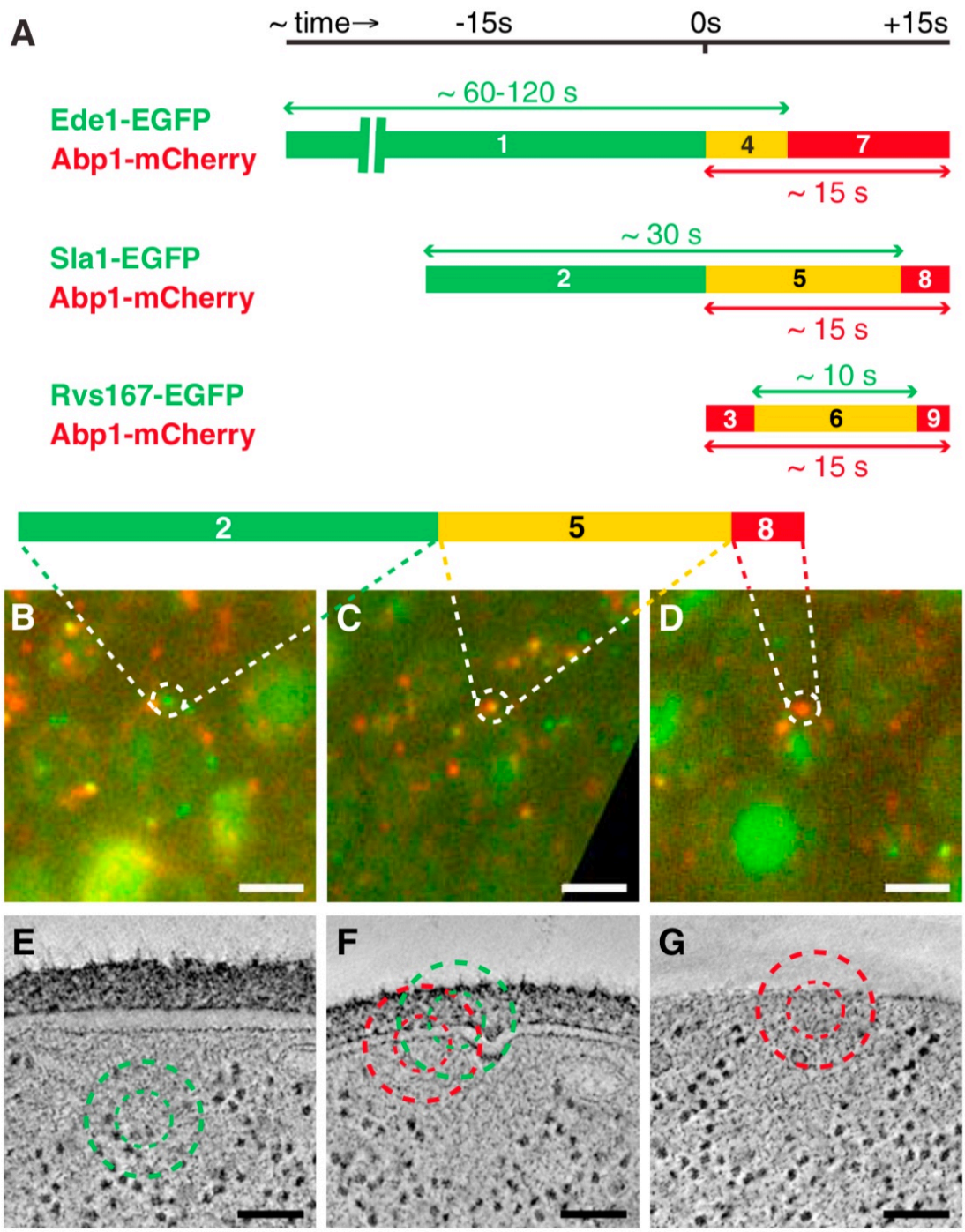

Figure 1.15: Examples of time-resolved fluorescence and electron tomography images, showing the overlays of GFP and RFP (green and red fluorescent proteins) signals from 300 nm sections of the yeast cells, that are expressed to indicate the presence of early coat proteins (Ede1 and Sla1), curvature sensor bar protein (Rvs167), and actin (Abp1). Time = 0 is assigned to when Abp1-mCherry appears, indicating the arrival of actin. Scale bars are 2 μm in fluorescent images, and 100 nm in EM images. Figure is taken from Ref. [48].

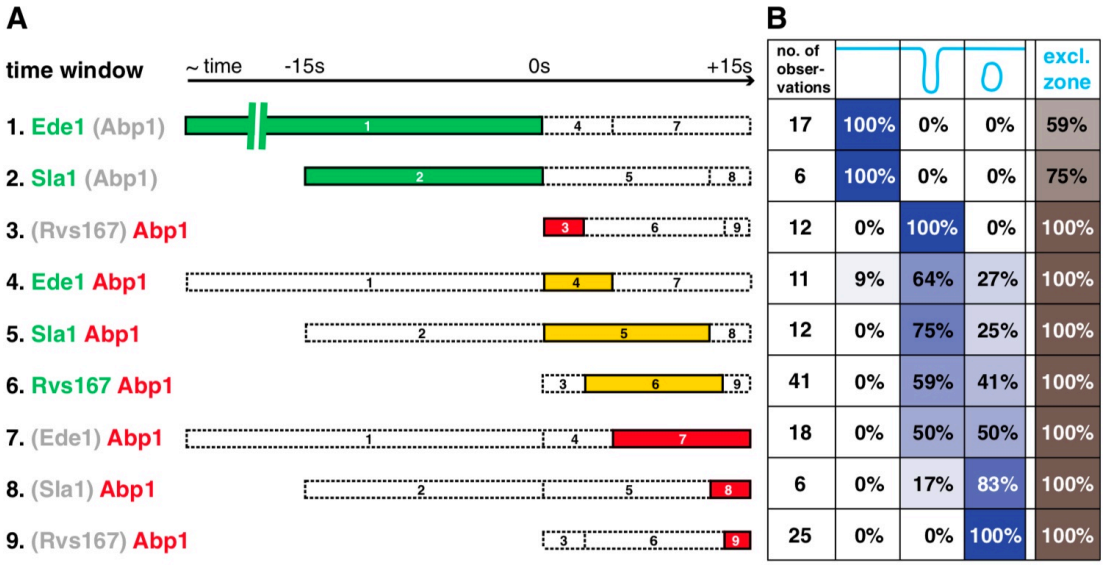

Figure 1.16: Time windows of the appearance of various fluorescent probes used to identify the presence of different endocytic proteins, along with the EM data for the frequency of observations of various membrane deformation stages (right side, with the first column for the number of observations). The coat assembly is formed with the early module proteins, including clathrin, scaffold protein Ede1, and at later times the adaptor protein Sla1. On average, 15 to 20 sec after assembly of these proteins, a short burst of actin polymerization occurs. Scission module proteins are recruited $\approx$ 3 sec after actin polymerization is initiated. But prior to the arrival of actin, none of the EM observations showed a deformed plasma membrane, indicating that membrane invagination occurs only after actin is recruited. Figure is adapted from Ref. [48].

100,000 endocytic sites in yeast [49]; see Figure 1.17. These experiments revealed a circular nano-template of actin polymerization at the membrane base. Images in Figure 1.18 show the distribution of actin nucleators Las17 (WASP homolog in yeast), on a ring with an average radius of $\approx 75\ nm$, which surrounds a central dot concentration of the actin-filament-membrane binding protein, Sla2. This nanoscale pre-patterning of actin nucleation defines the basis of mathematical modeling of how actin polymerization at the membrane base of the endocytic sites exert forces to bend the membrane.

Actin force distributions extracted from electron microscopy images of the membrane curvature during endocytosis have quantified pulling forces in the process [50]. Figure 1.19 (left) shows the result of the depth and curvature fitting analysis, and on the right the calculated actin force distributions based on the extracted deformation profiles. For these calculations, the authors treated the entire actin network as an elastic medium that is bounded to a rigid membrane. The extracted force profiles revealed a relatively flat pulling-force distribution at the center, with an estimated pulling pressure of about $0.5\ MPa$, surrounded by a ring-region of pushing forces that are not quite as flat (see Figure 1.19). This hump in the pushing-force distribution suggests varying filament growth rates in the pushing region. The total pulling force exerted by the actin network estimated from these force profiles is $\approx 2800\ pN$.

Although a lot of details are known about the composition of the endocytic machinery, it is not well known how the motions and interactions of the endocytic proteins, and in particular to our interest in this thesis, actin polymerization, lead to generation of large pulling forces.

At the most general level, a non-uniform actin polymerization distribution leads to a varying force density acting on the membrane. Figure 1.20 illustrates how different regions of local polymerization generate different force density patterns. A central polymerization region generates a focus of pushing forces that is balanced by the surrounding pulling forces; an outer ring of actin polymerization generates a central focus of pulling forces surrounded by pushing forces. In endocytosis, it is believed that actin polymerization at the Las17 ring surrounds a central region of little to no active

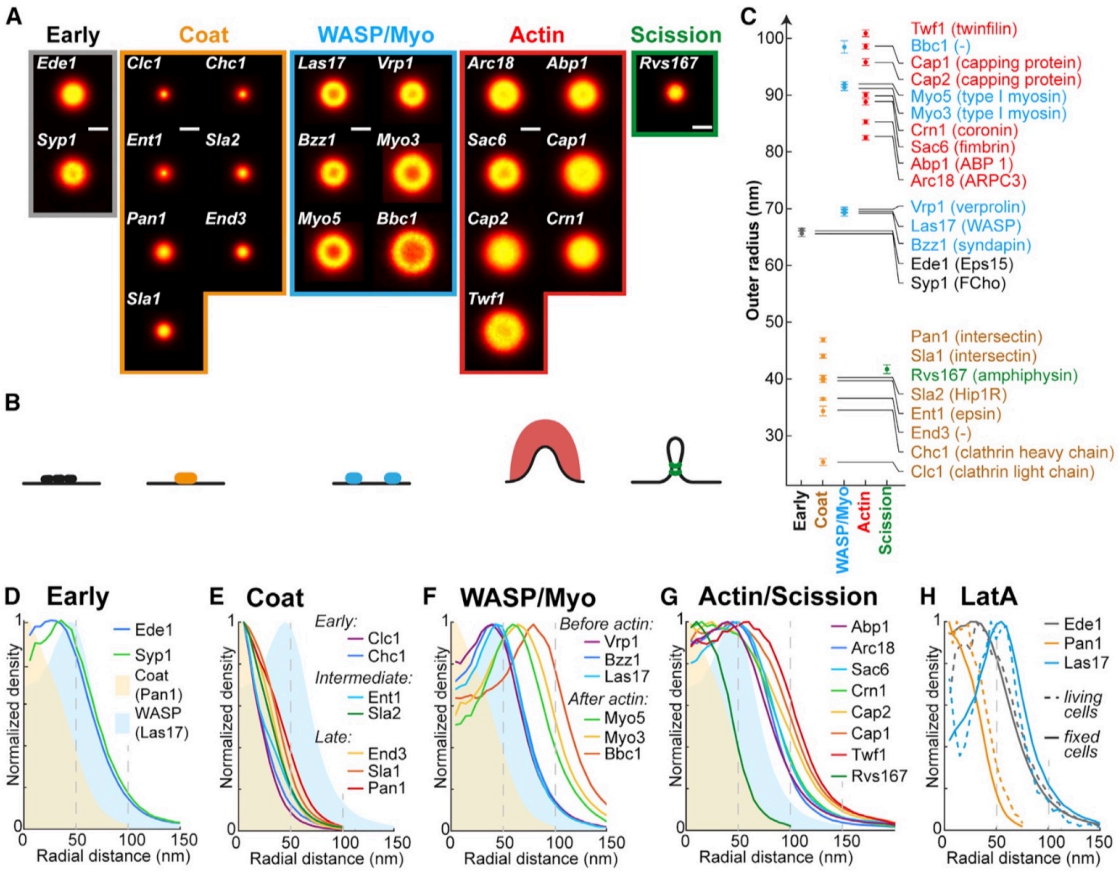

Figure 1.17: Images from super-resolution microscopy of sites of clathrin-mediated endocytosis in budding yeast revealed the nanometer spatial pattering of 23 fluorescently tagged endocytic proteins. Endocytic invaginations are oriented perpendicularly to the microscope focal plane, to obtain 2D projections of endocytic structure. The individual images provide snapshots of different endocytic time points, with the lateral distributions of endocytic proteins appearing as patches, rings, or irregular shapes. The average radial distributions derived by spatially aligning thousands of images from endocytic sites, followed by translations of their specific temporal organization, further illustrate the role of each protein in the endocytic machinery. Figure is taken from Ref. [49].

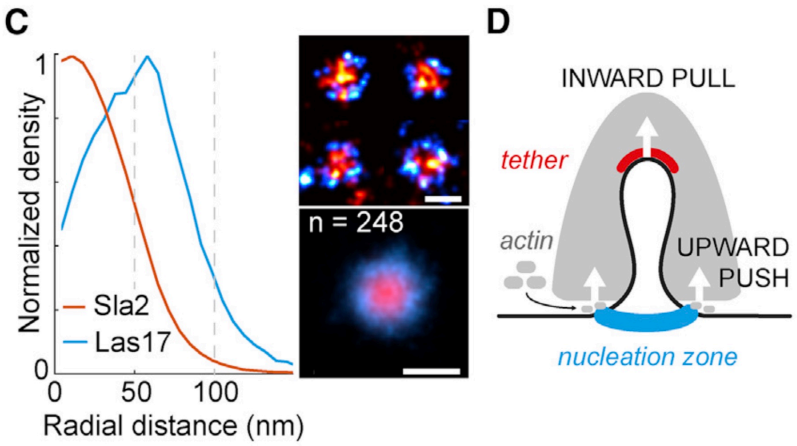

Figure 1.18: A ring of actin nucleators in yeast, Las17, surrounds a central concentration of filament-membrane binding proteins, Sla2. Observations are performed by super-resolution fluorescent microscopy. The average radial distributions are made from 248 observations. Actin polymerization on the periphery of the central region, where the filaments are attached to the membrane, exerts pushing forces on the membrane that in turn push the entire actin network inward. These forces, in balance with the pulling forces at the center, deform the membrane. Scale bar is 100 nm. Figure is adapted from Ref. [49].

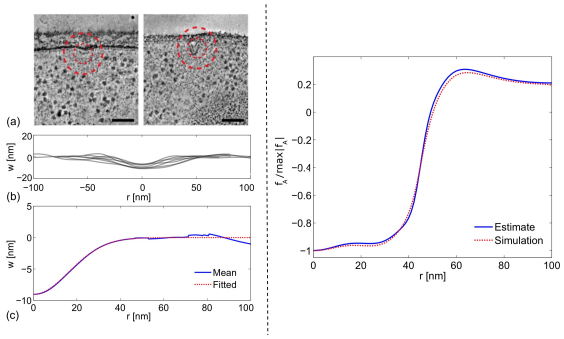

Figure 1.19: Fitting analysis for the depth and curvature of membrane deformations captured by EM (left), to use in quantitative analysis for relationship between polymerization and force, that yields the radial distribution of actin force (right). A region of pulling-forces at the center of the endocytic site, with a radius of ≈ 35 nm, is surrounded by a ring-shaped region of pushing-forces. This finding is consistent with the picture provided by super-resolution microscopy results. Figure is adapted from Ref. [50].

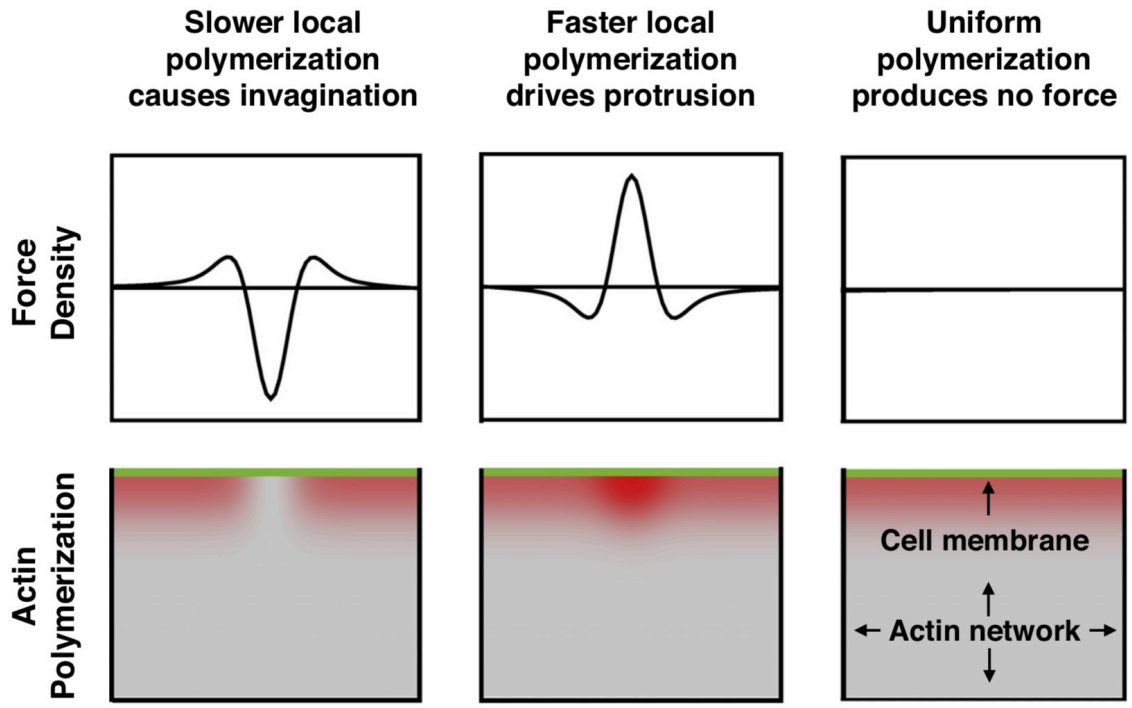

Figure 1.20: Inhomogeneous actin polymerization rates lead to non-uniform force densities. Red areas indicate where actin is polymerizing. Slower local polymerization in the center leads to a focus of pulling force surrounded by a ring of pushing force. If polymerization is faster at the center, the opposite force distribution occurs; central pushing force balanced by a ring of pulling force. Uniform actin polymerization produces no force. Figure is taken from Ref. [2].

actin polymerization. This surrounding pushing force drives the retrograde flow of the entire actin network. Since filaments in the central region bind to the membrane via the protein Sla2, the retrograde motion allows the pulling forces in the central region to pull the membrane inward. Pulling forces by actin polymerization must overcome opposing forces from turgor pressure, membrane tension, and membrane bending stiffness. The turgor pressure in yeast has a generally accepted value of 0.5 MPa [2] or more, and is significantly larger than other forces opposing invagination.

As discussed above, actin pushing and pulling forces are generated by differences in actin polymerization from point to point across the membrane. In a recent study [51], working with a continuum-mechanics model of the endocytic region, the authors made the assumption of a continuously varying actin polymerization rate, increasing from the center of the endocytic patch outwards. The results based on this specific

rate distribution showed that large pulling forces at the center are generated even by a small magnitude of force density over a large surrounding ring of actin polymerization. Figure 1.21 shows the profiles of actin growth after 1 simulation time unit (**a**) and the stress distribution after 1 time unit of growth (**b**) and 3 time units of growth (**c**). The actin polymerization stress is tensile and is enhanced over the central region, where the growth rate is smaller. This result suggests that even with small amount of actin polymerization at the center of the endocytic patch, large pulling forces can be exerted on the membrane from this region, given the right polymerization distribution and a large enough difference between actin polymerization rates in the different pushing and pulling regions.

Another model of membrane deformation (Figure 1.22) during endocytosis in yeast found an estimate of $\approx 3000\ pN$ for the minimum actin pulling-force that is required to sustain the invagination [52]. The parameters included in the fitting analysis are membrane curvature, membrane tension, and the invagination depth. However, their assumption of a point pulling force for actin at the tip of invagination is not quite accurate.

The total pulling force exerted by actin filaments on the membrane is generally assumed to be equal to the sum of the thermodynamic stall forces from the growing pushing filaments. This general assumption is used in stochastic simulations of the growth of a rigid 3D actin network [53], based on the Brownian ratchet model mechanism for actin subunit dynamics. The actin network is not treated as an elastic medium in this model, but rather as being infinitely rigid. The number of filament branches changes stochastically with a rate determined by the amount of actin in a "branching" region. Actin filament growth velocities are determined by the polymerization rate of the filaments in contact with membrane and the load per filament. Capping and severing of actin filaments are also treated stochastically. This model shows that a uniform distribution of Las17 proteins in a ring, with a constant detachment probability, leads to a pulling force in the central region. Membrane deformation is treated by an increasing detachment rate for Las17, which leads to a pulse-like actin behavior.

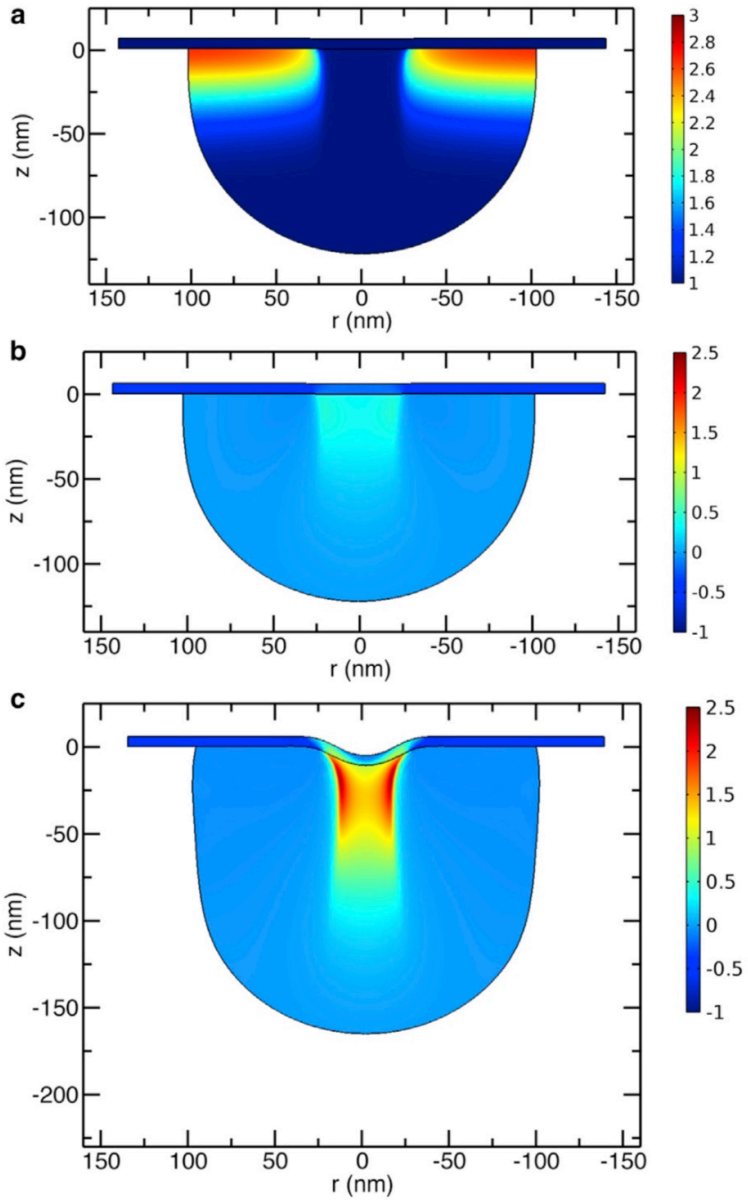

Figure 1.21: Actin growth and stress distribution, from continuum-model simulations of an elastic actin gel with the assumption of continuously increasing polymerization rate from the center of the endocytic region in vicinity of membrane outwards. Frame **a** shows the dimensionless growth parameter after 1 time unit of growth, while in frames **b** and **c** the color bars denote the stress in units of $10^5 Pa$ from actin gel after 1 and 3 time units of growth respectively. Turgor pressure is assumed to have a value of $2 \times 10^5 Pa$, 10 times larger than the actin gel shear modulus. Radius of invagination is 25 nm, and radius of actin gel is 100 nm. The distribution of actin pressure is consistent with the expectation from the assumed polymerization distributions; the stress is larger at the central region where the growth rate is smaller. Figure is adapted from Ref. [51].

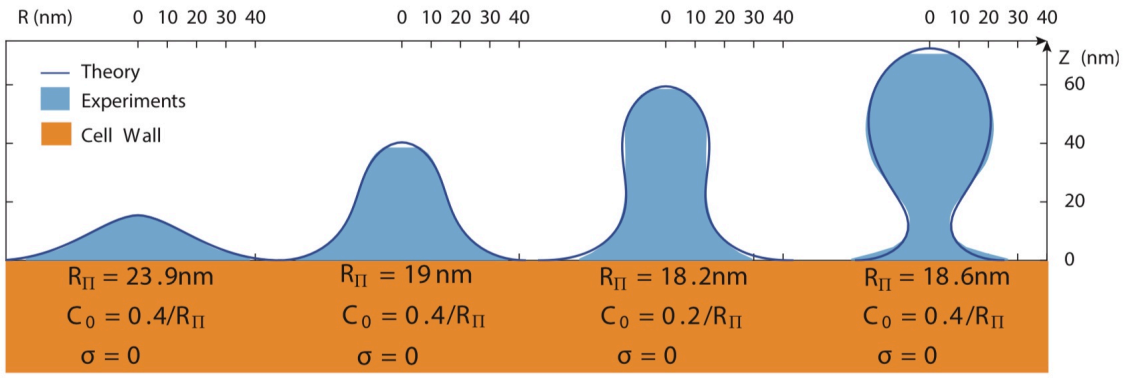

Figure 1.22: Theoretical analysis with fitting model parameter values to the experimental membrane deformation shapes gives an estimate of $\approx 3000\ pN$ of force that is required to be generated by actin polymerization, to reach the experimentally measured invagination depths. Figure is taken from Ref. [52].

In another modeling analysis of actin network dynamics in endocytosis [49], the authors used their experimental data derived from super-resolution microscopy for dimensions of the endocytic patch and spatial distributions of the proteins involved. This model (Figure 1.23) showed that a pre-patterned Las17 ring decoration on the membrane optimizes force generation for membrane invagination and substantially increases the efficiency of endocytosis. Actin subunit dynamics in this model is again based on the BR model, but individual filaments as well as the entire actin network are treated as elastic objects; filaments are considered to be elastic beams with persistence length $\approx 20\ \mu m$, and actin filament crosslinkers are treated stochastically and represented by springs with resting length 12 nm, and stiffness of 5 pN/nm. Filament-membrane connections in the central Sla2 dot region are represented by permanently attached springs with stiffness 200 pN/nm, and the zero resting length at the membrane surface. There is no explicit treatment of membrane deformation in this model. Actin filament branching is treated stochastically, with a gradual build up of the active Arp2/3 complex number. Forces exceeding 1000 pN were found to be generated by this 3D branched actin network. This force is large enough to overcome the opposing turgor pressure and successfully internalize the plasma membrane; given the assumed size of the pulling region (25 nm) and their estimate of turgor pressure (0.5 MPa), actin pulling forces exceeding $\approx 980\ pN$ can overcome the turgor pressure.

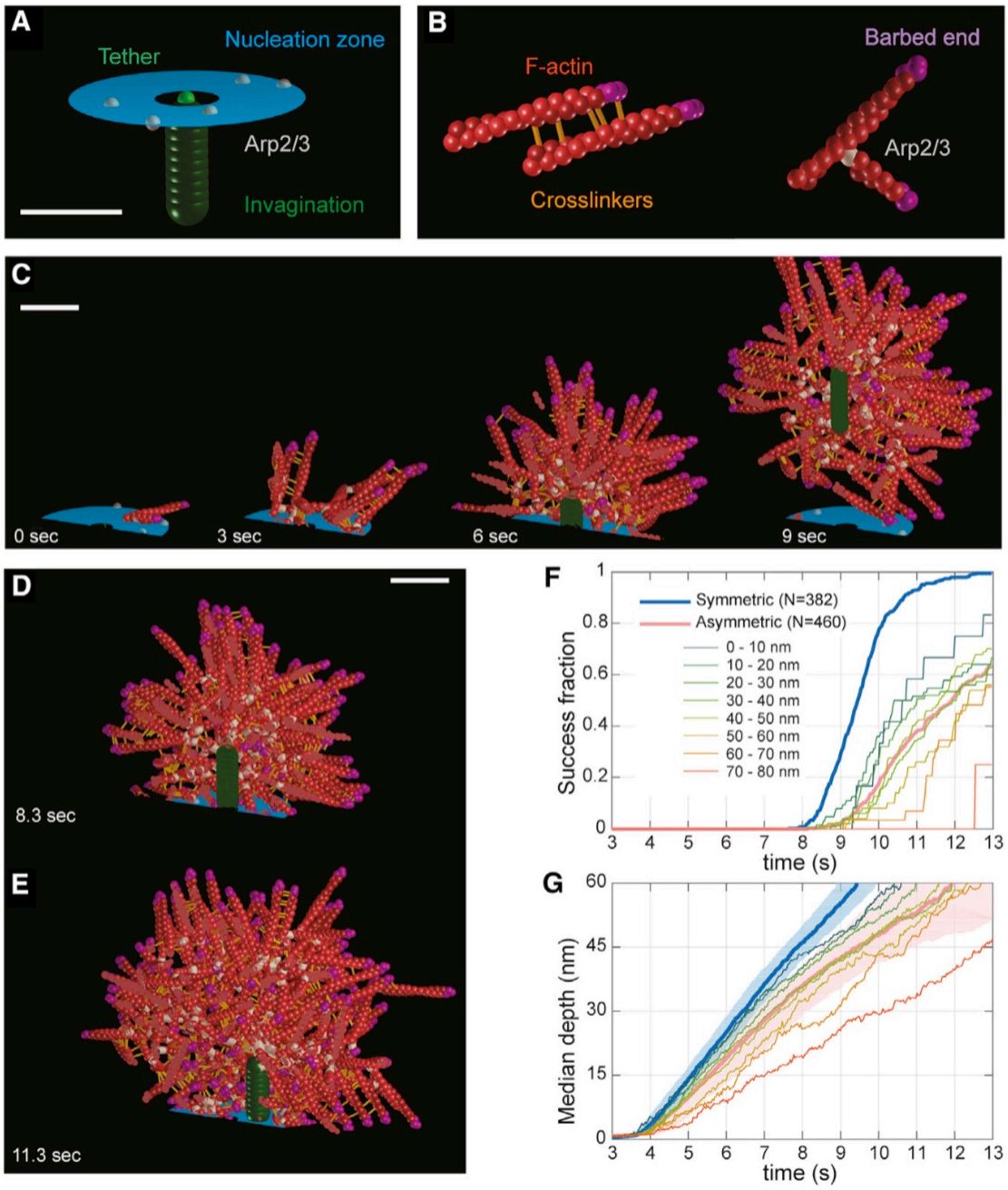

Figure 1.23: Mathematical modeling of the endocytic machinery shows that a nucleation zone that surrounds a central attached zone of actin filaments leads to central pulling forces due to the retrograde flow of the growing actin network. Filaments in the attached region are tethered to the membrane surface with stiff spring connectors (200 pN/nm). Their stiffness is constant over time. Successful endocytosis events are defined by a threshold on the invagination depth. The symmetrical distribution of the nucleation zone around the central Sla2 dot is crucial for the occurrence of successful invaginations. Scale bars represent 50 nm. Figure is taken from Ref. [49].

1.4 Summary of this thesis

In this thesis, we attempt to further clarify the mechanisms behind the generation of pulling forces by actin polymerization, using thermodynamic arguments and stochastic simulations of discrete arrays of crosslinked actin filaments. We discuss questions such as: What is the relation between force and polymerization rates of actin filaments? What are the magnitude and distributions of actin forces across the plasma membrane? How large is the total pulling force that can be generated? How long does it take for the system of actin gel and membrane to reach steady-state, and how does this time relate to the stiffness of the actin gel? Can pulling filaments sustain the large forces required, without detaching from the membrane?

The main focus of this thesis is force generation by filament ensembles. However, at the beginning of these calculations, we found that the methodology even for single filaments was inadequately developed. For this reason, Chapter 2 develops the methodology for simulating force generation by single filaments. We use it to study the effect of different force fields on the growth of a single biopolymer. In most previous stochastic simulations, actin polymerization and depolymerization rates are averaged over time and depend only on the load per filament. We derive and implement potential-dependent on- and off- rates, using thermodynamically valid arguments. Force-velocity relations are studied for various filament-obstacle interaction potentials. A well in the filament-obstacle interaction potential could represent, for example, Sla2 attachments. The growth of filaments with purely repulsive potentials is essentially that predicted by the BR model. Filaments with well potentials grow slower, and wells deeper than $25k_BT$ stop the polymerization essentially completely. The paper for this chapter is currently under review at Physical Review E

Chapter 3 expands this study for a single filament to an array of multiple filaments. We use thermodynamically consistent rate constants derived in Chapter 2, to study the force generation mechanisms of a 12×12 square array of actin filaments, containing a central 6×6 array of slowly growing filaments. We find that the total pulling force is limited by the sum of the stall forces of the pushing filaments, as expected. The total

pulling force reaches more than 95% of theoretical stall force in less than 10 seconds for potential wells as deep as $100k_BT$. We find that strong attachments of filament-membrane in the pulling region are required for the generation of substantial forces, and that stronger attachments lead to slower polymerization of pullers but larger generated pulling forces. We find that the amount of actin polymerization is larger for softer gels, but the chance for the breakage of membrane-filament links is also higher. Soft gels with weaker puller binding are more likely to experience rupture before steady-state is reached. The paper for this chapter will be submitted for publication within two weeks.

The stochastic simulations are done in C++, and OpenGL is used for writing the visualization programs. Some sample codes are explained in Chapter 4. Finally, in Chapter 5, I present the conclusions of the thesis and the steps that can be taken to further improve the model.

Chapter 2

The effect of the filament-obstacle interaction on the force-velocity relation of a growing biopolymer

2.1 Introduction

Polymerization of biopolymers such as actin filaments provides force to drive both protrusion and invagination of the cell membrane. This process is modulated by the interaction between the filament tip and the membrane, which varies considerably between different cellular phenomena. In lamellipodia, filaments are likely weakly bound to the membrane by their interaction with, for example, WASP-family actin-nucleating proteins [54]. On the other hand, in filopodia actin filaments are nucleated by formins, which can bind actin filaments strongly [55]. Furthermore, in processes that require strong pulling forces to bend the membrane, such as endocytosis in yeast, some actin filaments must be strongly bound to the endocytic site. In this process, the binding is believed to result from the protein Sla2, which has both actin-binding domain and a domain that links it to the membrane. [56]. Recent super-resolution experiments have shown that WASP (Las17 in yeast) forms a ring around a Sla2 dot [49], and pulling forces are probably concentrated in the dot [50, 53]. Similarly, microtubule interactions with the cell membrane are mediated by a range of proteins,

which may lead to a variety of effective interaction potentials [57, 58]. In all of these cases, it is important to understand how the interaction between a growing filament and the membrane plus associated proteins affects the polymerization rate. The filament-membrane interaction may be optimized for different criteria, such as polymerization velocity where migration speed is crucial, or stability where strong pulling forces are required.

Most previous calculations of force generation by polymerization have used hard wall repulsive potentials acting between the filament tip and the obstacle. The classic Brownian ratchet (BR) model [12] used such a potential to treat polymerization in the presence of a diffusing obstacle, assuming that the monomer on-rate increases suddenly from zero to its free-filament value at a certain distance from the membrane. Analysis of this model showed that in the limit of fast obstacle diffusion, the hard-wall potential gives rise to a growth velocity that decays exponentially with opposing force:

$$v_{growth} = \delta[k_{on}^0 \exp\left(-F\delta/k_BT\right) - k_{off}^0], \tag{2.1}$$

where δ is the step size per added subunit, and $k_{on,off}^0$ are the free-filament on- and off-rates.

Calculations based on this analysis can qualitatively explain the mechanism behind the generation of pushing forces by actin polymerization in several types of cellular protrusions, such as filopodial and lamellipodial protrusions [59, 60, 61, 62, 63, 64, 65, 66, 67, 68]. The basic features of intracellular motion of pathogens such as Listeria, which is driven by actin polymerization, can also be explained by BR-type models.

However, the true interaction is continuously varying and the force may have both attractive and repulsive components. It is not known how these variations affect the force-velocity relation. For example, a potential with a deep well might trap the growing end of the filament near the obstacle, and thus slow polymerization. On the other hand, a smoother potential might speed polymerization. A small number of calculations have treated such smoothly varying potentials. Calculations in 2D using an explicitly moving obstacle with explicitly diffusing monomers to treat the growth

rate of a single actin filament, interacting with an obstacle via a steeply increasing force field, found that the velocity decays more rapidly than the BR prediction [69]. This effect was attributed to a diffusion barrier in which monomers had to traverse a tunnel-like region to reach their binding site at the end of the filament. Such effects are expected to be smaller in 3D. Calculations using a range of force fields to treat 3D polymerization [70, 71], including filament bending, found large acceleration of growth by a soft obstacle when the obstacle diffusion coefficient was small. Refs. [41] and [72] considered actin filaments strongly bound to the obstacle, but assumed they did not grow. Studies of filament growth while clamped to a motile obstacle via a deep potential energy well suggested that the filament-obstacle attachment is the controlling factor for the elongation rate [73, 74]. A later model considered filaments attached to an obstacle with a double-well potential [75], explicitly treating diffusive motion of the obstacle. It was found that a filament can push the obstacle and grow with a speed of about half of the free filament speed and thus progressively polymerize, if the potential is sufficiently deep.

Among these preceding studies, there is no systematic exploration of a broad range of possible force fields, to establish how the force field influences the force-velocity relation. In fact, the methodology for performing calculations with smoothly varying filament-obstacle interactions is not well established. One must choose spatial dependences for both the interaction energy between the obstacle and the filament tip, and the polymerization rate parameters. In previous work these dependences have often been chosen independently.

Here we establish a thermodynamic relationship between the spatial dependence of the polymerization-rate parameters and that of the interaction energy, simplifying the construction of appropriate force-generation models. This relationship applies to a filament growing against a diffusing obstacle whose motion is treated explicitly, with a smoothly varying filament-obstacle interaction. Performing calculations without this relationship can lead to an incorrect stall force. In our implementation, either the on-rate or off-rate is reduced, depending on the form of the interaction potential; neither is increased. We then perform a systematic set of simulations for

a broad range of possible filament-obstacle interaction potentials, treating polymerization and depolymerization as well as obstacle motion stochastically. We find that monotonically decaying repulsive potentials lead to force-velocity relations very similar to the BR prediction, as expected from general thermodynamic principles. Weak attractive potentials both reduce the zero-force velocity, and lead to a decay that is more rapid than the Brownian-ratchet prediction. Deep and narrow potentials lead to slow polymerization at all force values. We find that attached filaments stop growing if the potential well is deep enough to sustain pulling forces greater than about 1pN, unless the potential well has a shelf comparable to the monomer size. Potentials with such a shelf have fairly rapid polymerization at zero force and have a force-velocity relation that decays almost linearly.

Although the model is highly simplified, multiscale calculations such as those of Ref. [59, 61, 76, 68, 77, 78, 51, 79] have demonstrated the utility of simple, but approximate results for the force-velocity relation in calculating the properties of cells and processes inside cells. The general understanding gained from the present studies will enhance the physical relevance of such multiscale calculations.

2.2 Model

2.2.1 Filament-obstacle interaction

The model (Figure 2.1) treats the stochastic polymerization of a biopolymer, exerting force on an explicitly moving, flat, penetrable obstacle. We envisage the base of the filament as being rigidly anchored. Actin filaments, for example, could be anchored in a crosslinked actin meshwork. For conceptual simplicity the results presented here are for a filament growing perpendicular to the obstacle without bending fluctuations; results for a filament growing at an oblique angle, including membrane fluctuations, are described in the Appendices. We treat a range of filament-obstacle interactions given by smooth potential functions having the form

$$U(r) = Ae^{-\kappa_1 r} - Be^{-\kappa_2 r} \tag{2.2}$$

or

$$U(r) = Ae^{-\kappa_1 r} - Ce^{-[\kappa_3(r-r_1)]^2} - De^{-[\kappa_4(r-r_2)]^2} \tag{2.3}$$

Here, A, B, C, D, κ_1, κ_2, κ_3, κ_4, r_1, and r_2 are constants, and r is the variable gap between the tip of the filament and the obstacle. Filament-obstacle binding can be naturally included in the force field via the B term in Eq. 3.4; we denote such a potential a "simple well". A non-zero C in Eq. 3.5 also adds a Gaussian "spike" to the potential at $r = r_1$ which can be either attractive or repulsive. Choosing both C and D to be positive in Eq. 3.5 generates a double-well potential, as shown in Figure 2.2(b). The depth of the wells in the potentials represents the energy of binding filaments to membrane-bound proteins. The corresponding forces that the filament exerts on the obstacle are

$$F(r) = -\frac{dU}{dr} = A\kappa_1 e^{-\kappa_1 r} - B\kappa_2 e^{-\kappa_2 r} \tag{2.4}$$

and

$$F(r) = A\kappa_1 e^{-\kappa_1 r} - 2C{\kappa_3}^2(r-r_1)e^{-[\kappa_3(r-r_1)]^2} - 2D{\kappa_4}^2(r-r_2)e^{-[\kappa_4(r-r_2)]^2}, \tag{2.5}$$

respectively. We will denote a filament having only repulsive potential terms a "pusher". A filament with an interaction potential containing a well or a spike is denoted a "puller" (although it can also exert a pushing force).

2.2.2 Obstacle dynamics

The obstacle position is stepped forward in time according to biased Brownian motion driven by $F(r)$ and thermal fluctuations. We use a "filament-centric" approach in our simulations, in which the filament base is assumed to be stationary and the obstacle moves. Cases where the filament base is moving can be handled by a simple coordinate transformation, in which obstacle motion is the inverse of the base motion and the diffusion coefficient of the obstacle is replaced by that of the entity to which

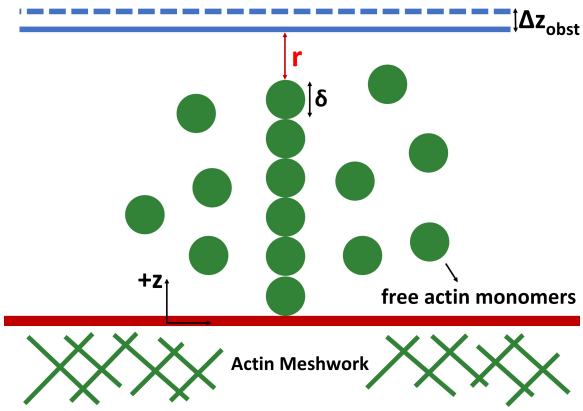

Figure 2.1: Schematic of model applied to an actin filament: r is the distance between the filament tip and the obstacle, δ is the actin monomer size = 2.7nm, and Δz_{obst} is the obstacle position fluctuation in the +z direction during a given time step. We treat the filament's base as being solidly anchored.

the filament is anchored. At each time step, the diffusive motion of the obstacle is calculated by the discrete form of the Langevin equation (Ref. [80], Chap. 3):

$$\Delta z_{obst} = \alpha\sqrt{24\Delta t}\sqrt{D_{obst}} + \frac{D_{obst}}{k_B T}\Delta t[F(r) + F_{load}] \tag{2.6}$$

where D_{obst} is the obstacle diffusion constant, F_{load} is the external force applied on the obstacle, Δt is the time step, and α is a random number uniformly distributed between $-\frac{1}{2}$ and $\frac{1}{2}$, so that $< \alpha^2 >= \frac{1}{12}$. Consecutive time steps are uncorrelated.

2.3 Results

2.3.1 Thermodynamic relation between $k_{on}(r)$ and $k_{off}(r)$

It is physically clear that at least k_{on} must be modified as a filament tip approaches an obstacle, because there is less room available for new subunits to add. Some previous models [81, 82, 83, 84] treated hard-wall potentials and considered $\bar{k}_{on}$, the addition rate averaged over a time long in comparison with the time scale of filament-tip fluctuations. They argued that when the distance between the filament tip and the closest obstacle position to the filament tip in a multi-filament simulation is less then

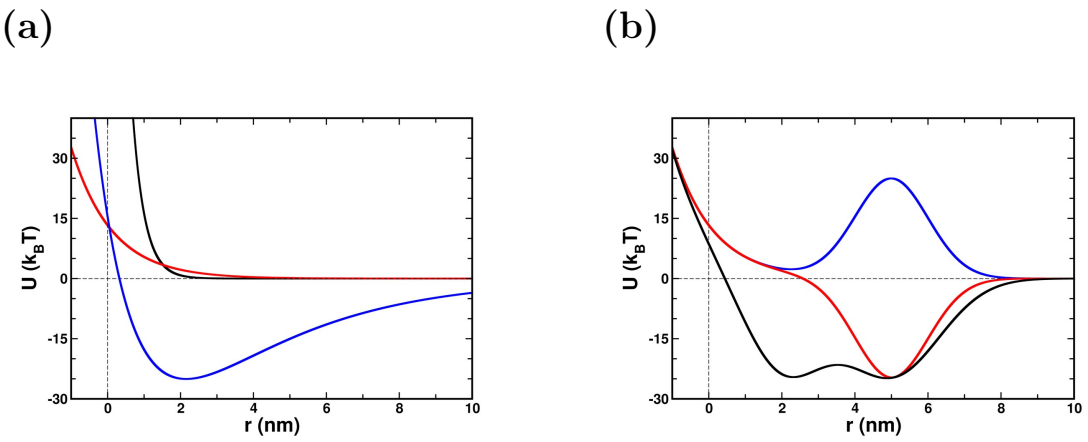

Figure 2.2: Filament-obstacle interaction potentials. **(a)** Potentials from Eq. 3.4. Black curve represents a hard obstacle, with A=1339 $pN{\cdot}nm$, B=0, and κ_1=3 nm^{-1}. Red curve corresponds to a soft obstacle with A=54.7 $pN{\cdot}nm$, B=0, and κ_1=0.9 nm^{-1}. Blue curve shows a simple-well potential with a depth of $25k_BT$, with parameter values A=358 $pN{\cdot}nm$, B=295 $pN{\cdot}nm$, κ_1=0.9 nm^{-1}, and κ_2=0.3 nm^{-1}. **(b)** Potentials from Eq. 3.5, containing one or more Gaussian spikes. Blue curve has a positive Gaussian spike described by parameters A=54.7 $pN{\cdot}nm$, D=0, $\kappa_3 = 0.707\,nm^{-1}$, $r_1 = 5$ nm, and C = -104 $pN{\cdot}nm$; red curve differs from this one by having C = 104 $pN{\cdot}nm$. Black curve is a double-well potential with A=54.7 $pN{\cdot}nm$, C=100 $pN{\cdot}nm$, D=100 $pN{\cdot}nm$, $\kappa_3 = 0.643\,nm^{-1}$, $\kappa_4 = 0.544\,nm^{-1}$, $r_1 = 2$ nm, and $r_2 = 5$ nm.

the monomer length increment δ, $\bar{k}_{on}$ is reduced by a factor of $\exp\left[-F(\delta - r)/k_BT\right]$ relative to the free-filament value, where F is the time-averaged force exerted on the filament tip, and r is the distance between filament tip and the obstacle. This relationship holds when the force required to bend a filament tip is fairly constant over the size of a subunit. Here we show that a more complex relationship holds when the filament-obstacle interaction varies strongly over distances on the order of the subunit size. In such cases, it is necessary to include obstacle motion explicitly in the calculations. Then one uses rates $k_{on}(r)$ and $k_{off}(r)$ that refer to polymerization and depolymerization events occurring at a given filament-tip and obstacle position, rather than time-averaged rates.

We consider polymerization of filaments in the absence of nonequilibrium effects such as hydrolysis of ATP to ADP in actin. In this case, the stall force must be independent of the form of the interaction potential $U(r)$ between the filament tip and the obstacle. This follows from the thermodynamic arguments of Ref. [85]: At

the stall force, changes in chemical free energy resulting from polymerization precisely balance changes in mechanical energy, relating the stall force to the polymerization free energy per subunit. Then the combined system of obstacle and filament can be described by a free energy function, containing a mechanical term $F_{ext}z$ where F_{ext} is the external force (measured in the direction opposite to filament growth) acting on an obstacle with coordinate z, a chemical term $N\Delta G$ where N is the number of subunits in the filament and ΔG is the chemical free-energy increment per added subunit, and $U(r)$. Defining r to be the obstacle-tip distance, $z = r + N\delta$. Then the total free energy as a function of N and r is

$$G_{tot} = N\Delta G + NF_{ext}\delta + F_{ext}r + U(r). \tag{2.7}$$

Here the free energy is defined on a time scale shorter than the time scale of monomer addition and obstacle motion but still long enough that the free energy of an actin monomer interacting with water molecules is well defined.

The stall force F_{stall} is defined by G_{tot} being independent of N at a fixed value of r, so that

$$F_{stall} = -\Delta G/\delta, \tag{2.8}$$

as is well known [12, 85]. This result implies [85] that

$$F_{stall} = (k_B T/\delta) \ln (k^0_{on}/k^0_{off}), \tag{2.9}$$

where k^0_{on} and k^0_{off} are rates for a free filament not interacting with an obstacle. Note that k^0_{on} is the on-*rate* (having units of s^{-1}), which is the product of the on-rate constant with the free-actin monomer concentration.

Now consider the dynamics of the filament-obstacle system at the stall force. The system is in equilibrium and thus obeys detailed balance (recall that ATP hydrolysis

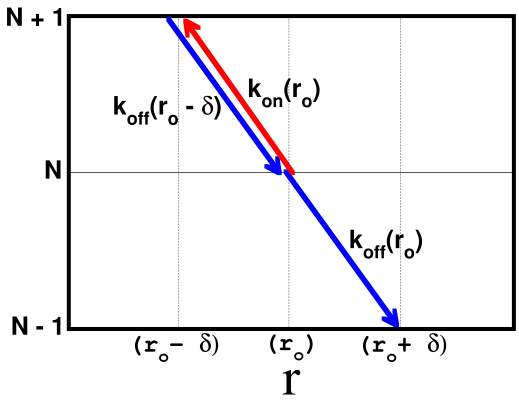

Figure 2.3: Dynamics of obstacle motion and actin filament polymerization and depolymerization. Red arrow corresponds to the polymerization rate at the point where the filament-obstacle gap is r_o, and the blue arrows correspond to the depolymerization rates at r_o and $r_o - \delta$.

is neglected). Since the system is at the stall force, the free energy

$$G_{tot} = F_{stall} \cdot r + U(r), \tag{2.10}$$

is independent of N. The dynamic processes in the system are i) Brownian motion of the obstacle, ii) polymerization, and iii) depolymerization. In Figure 2.3, Brownian motion leads to infinitesimal steps in r, while polymerization leads to jumps $r \to r-\delta$ and depolymerization leads to jumps $r \to r+\delta$. Because the system is in equilibrium, the probability distribution $P(r;N)$ satisfies the Boltzmann relation. In particular, referring to Figure 2.3 and ignoring normalization of P,

$$\begin{aligned} P(r;N) &= \exp\{-[U(r) + F_{stall} \cdot r]/k_B T\} \\ P(r-\delta;N+1) &= \exp\{-[U(r-\delta) + F_{stall} \cdot (r-\delta)]/k_B T\} \end{aligned} \tag{2.11}$$

Detailed balance between the states $(r;N)$ and $(r-\delta;N+1)$, which holds for this equilibrium system, implies that

$$k_{on}(r)P(r;N) = k_{off}(r-\delta)P(r-\delta;N+1) \tag{2.12}$$

Therefore, using Eq. 2.9,

$$\begin{aligned}\frac{k_{on}(r)}{k_{off}(r-\delta)} &= \exp\{-[U(r-\delta)-U(r)]/k_BT\}\cdot\exp\left(F_{stall}\cdot\delta/k_BT\right)\\ &= \exp\{-[U(r-\delta)-U(r)]/k_BT\}\cdot\frac{k^0_{on}}{k^0_{off}}\end{aligned} \tag{2.13}$$

This relationship guarantees that the correct stall force is obtained. It generalizes the well-known result [85] for the average rates that

$$\bar{k}_{on}/\bar{k}_{off} = \exp\left(-F\delta/k_BT\right)k^0_{on}/k^0_{off}. \tag{2.14}$$

Eq. 2.14 follows from Eq. 2.13 in the limit $D_{obst}\to\infty$. To see this, note that from Eq. 2.13 the rate constants have the form

$$\begin{aligned}k_{off}(r) &= k^0_{off}f(r)\\ k_{on}(r) &= k^0_{on}\exp\{-[U(r-\delta)-U(r)]/k_BT\}f(r-\delta)\end{aligned} \tag{2.15}$$

where f is a function of r. When $D_{obst}\to\infty$, the obstacle position distribution $P(r)$ has its thermal equilibrium form $P(r)=\exp\{-[U(r)+Fr]/k_BT\}/Z$, where $Z=\int_{-\infty}^{\infty}\exp\{-[U(r)+Fr]/k_BT\}dr$. Then

$$\begin{aligned}\bar{k}_{on} &= (k^0_{on}/Z)\int_{-\infty}^{\infty}\exp\{-[U(r-\delta)-U(r)]/k_BT\}\exp\{-[U(r)+Fr]/k_BT\}f(r-\delta)dr\\ &= (k^0_{on}/Z)\int_{-\infty}^{\infty}\exp\{-[U(r-\delta)]/k_BT\}\exp\left[-Fr/k_BT\right]f(r-\delta)dr\\ &= (k^0_{on}/Z)\exp\left(-F\delta/k_BT\right)\int_{-\infty}^{\infty}\exp\left[-U(r)/k_BT\right]\exp\left[-Fr/k_BT\right]f(r)dr\end{aligned} \tag{2.16}$$

while

$$\bar{k}_{off} = (k^0_{off}/Z)\int_{-\infty}^{\infty}\exp\left[-U(r)/k_BT\right]\exp\left[-Fr/k_BT\right]f(r)dr \tag{2.17}$$

$$= \bar{k}_{on}[\exp\left(F\delta/k_BT\right)k^0_{off}/k^0_{on}], \tag{2.18}$$

implying that Eq. 2.14 holds. When obstacle diffusion is not rapid, Eq. 2.14 will not

necessarily hold because energy is dissipated by the obstacle drag, which is inversely proportional to D_{obst} according to the Einstein relation. This is not accounted for in the thermodynamic analysis. The stall force, however, is unaffected by obstacle drag because the obstacle is stationary on average.

Eq. 2.13 correctly implies that the force-velocity relation is independent of the choice of zero for evaluating r. For example, adding a constant shift Δr to r would cause the typical positions sampled by the filament tip to move out a distance Δr from the obstacle, i. e. remaining close to the minimum of $U(r)$ if the potential has a deep well. Then the values sampled by the factor $\exp\{-[U(r-\delta)-U(r)]/k_BT\}$ will also remain the same, corresponding to the energy difference between a point at the minimum and one shifted in by Δr from the minimum. This also implies that for the repulsive potential, the force-velocity relation is independent of the prefactor A; changes in the prefactor can be accounted for by changing the zero of the r-coordinate, which does not affect the force-velocity relation. This is confirmed by our numerical simulations below.

The derivation above applies to a single-stranded filament growing perpendicular to the obstacle. However, Eq. 2.13 holds for a broader range of models. If the filament grows at an angle of θ relative to the obstacle, then the schematic of Figure 2.3 holds provided that δ is replaced by $\delta\cos(\theta)$, the step size per added subunit. Similarly, for multistranded filament growth Figure 2.3 applies provided that a new subunit can add only at a unique specified site (typically next to the preceding one); then δ is again the step size per added subunit. Thus Eq. 2.13 holds for both these cases. It also holds when filament bending degrees of freedom are included, and for systems of many filaments. If, for example, one describes the bending of a single filament by angle θ, then Figure 2.3 applies to transitions occurring at a given value of θ. Because detailed balance must hold for all transitions in a system at equilibrium, Eq. 2.13 will still hold. In systems of many filaments, Figure 2.3 would apply to a single filament, and again transitions involving just that filament must satisfy detailed balance at the stall force.

Eq. 2.13 does not uniquely determine $k_{on}(r)$ and $k_{off}(r)$. In our simulations, we

make a minimal assumption, that has frequently been used for the rates $\bar{k}_{on}$ and $\bar{k}_{off}$, by preventing both rates from exceeding the free filament on and off rates:

$$\begin{aligned} k_{on}(r) &= k_{on}^0 \exp\{-[U(r-\delta)-U(r)]/k_BT\} \qquad \text{if} \quad U(r-\delta) > U(r) \\ k_{on}(r) &= k_{on}^0 \qquad\qquad\qquad\qquad\qquad\qquad\qquad\qquad\quad \text{if} \quad U(r-\delta) < U(r) \end{aligned} \tag{2.19}$$

$$\begin{aligned} k_{off}(r) &= k_{off}^0 \exp\{-[U(r+\delta)-U(r)]/k_BT\} \qquad \text{if} \quad U(r+\delta) > U(r) \\ k_{off}(r) &= k_{off}^0 \qquad\qquad\qquad\qquad\qquad\qquad\qquad\qquad\quad \text{if} \quad U(r+\delta) < U(r) \end{aligned} \tag{2.20}$$

Thus if $U(r)$ is monotonically repulsive, there is no correction to k_{off} in Eq. 3.10. This assumption has been made in most previous calculations in the literature. We do not have strong arguments justifying the assumption, but have decided to make it here in order to avoid investigating an unwieldy set of possibilities.

In the limit of a hard obstacle, where $U(r-\delta)$ jumps suddenly from 0 to ∞ when r becomes less than δ, $k_{on}(r)$ in Eq. 3.9 will vanish when $r < \delta$ and equal k_{on}^0 otherwise, as in the BR analysis. For a slowly varying repulsive $U(r)$, force balance on the obstacle implies that typical values of r will satisfy $dU/dr \simeq -F_{ext}$. Then $U(r-\delta) - U(r) \simeq F_{ext}\delta$, so that k_{on} is reduced by the familiar $\exp(-F_{ext}\delta/k_BT)$ factor. However, in the case of an interaction potential with a deep narrow well, the results can be quite different. For vanishing external force on the obstacle, basing the slowing on the average obstacle force will give no correction. However, Eqs. 3.9 and 3.10 will give corrections to both k_{on} and k_{off}. The filament tip will generally be near the bottom of the well. Therefore both $U(r-\delta) - U(r)$ and $U(r+\delta) - U(r)$ are positive, so that k_{on} and k_{off} are reduced.

2.3.2 Numerical results for different potentials and finite D_{obst}

We calculated the force-velocity relations for a range of filament-obstacle interaction potentials described above, including "pusher" and "single-well" potentials (Figure 2.2a), and potentials having positive or negative Gaussian spikes as well as a

double-well potential (Figure 2.2b). The key parameter values are given in Table 3.1. The free-filament polymerization rate k_{on}^0 is taken for a concentration of $1\mu M$ actin with an on-rate constant of $11.6\mu M^{-1}s^{-1}$ [86]. Because the fractional error of the off-rate k_{off}^0 measured in Ref. [86] is much larger than that of the on-rate constant, we have assigned it a rough estimate of 1 s^{-1} corresponding to the general range of values in the literature. The obstacle diffusion coefficient D_{obst} is taken as that of a sphere of radius $R = 5\mu m$, using the Stokes relation $D_{obst} = k_B T/6\pi\mu R$, where the viscosity μ is taken as that of cytoplasm, assumed to have a value $8.9 \times 10^{-3} Pa \cdot s$ ten times larger than that of water. This corresponds to relatively rapid diffusion

Table 2.1: Symbol definitions and parameter values.

Symbol	Definition	Value
δ	Actin step size	2.7 nm
D_{obst}	Obstacle diffusion coefficient	5000 nm^2/s
D_{tip}	Filament tip diffusion coefficient	5×10^4 nm^2/s
Δt	Simulation timestep	10^{-8}s
k_{on}^0	Free filament polymerization rate	11.6 s^{-1}
k_{off}^0	Free filament depolymerization rate	1 s^{-1}
F_{stall}	Filament stall force	3.74 pN
$U(r)$	Potential of interaction between filament tip and obstacle	varies
$F(r)$	Force exerted on obstacle by filament	varies
F_{load}	External force on obstacle	varies
v_{growth}	Filament growth velocity	varies
r	Gap between filament tip and obstacle	varies
z_{obst}	Obstacle z coordinate (height)	varies

according to the measure $D_{obst}/k_{on}^0\delta^2 \simeq 50$ [12]. Because this ratio is the key factor controlling the polymerization behavior, our results could also be taken to describe, for example, a system with faster polymerization and faster diffusion. The effects of using lower values of D_{obst} are described in Appendix B. The value of filament tip diffusion coefficent D_{tip} (used in the calculations in Appendix A) is unknown. Because the moving part of the filament is much smaller than the sphere that we treat as an obstacle, we choose D_{tip} to be 10 times larger than D_{obst}, fast enough to ensure that filament-tip fluctuations are much faster than obstacle fluctuations. We show results for a rigid filament growing at perpendicular incidence. Results for a

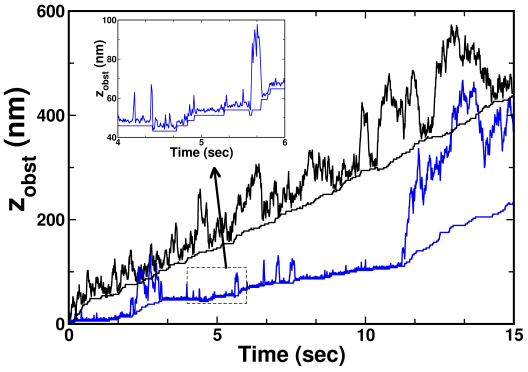

Figure 2.4: Time course of filament length and obstacle motion for zero external force. Upper black curve is obstacle motion time course for a repulsive filament-obstacle interaction potential (corresponding parameter values from Eq. 3.4 are: A=54.7 $pN{\cdot}nm$, B=0, and κ_1=0.9 nm^{-1}) and the lower black curve is the filament height vs. time. Upper blue curve is the time course of the obstacle motion for an potential with an attractive well of depth 5 k_BT (parameter values from Eq. 3.4 are: A=71.6 $pN{\cdot}nm$, B=35.8 $pN{\cdot}nm$, κ_1=0.9 nm^{-1}, and κ_2=0.3 nm^{-1}) with lower blue curve showing the filament height. Inset shows discrete polymerization and depolymerization steps, as well as the obstacle fluctuations against the filament tip.

fluctuating filament tip, growing at oblique incidence, are given in Appendix A.

Figure 2.4 shows sample time courses of filament length and obstacle position at zero load for two different force fields. The black curves correspond to a "soft" repulsive potential (see Figure 2.2a). The filament grows at roughly the free-filament rate and the obstacle has excursions of 100 nm or more away from the filament tip. The blue curves correspond to a force field with an attractive well (Figure 2.2a) of depth 5 k_BT. Here the growth is slower by about 50%. The obstacle excursions are smaller on average. Although there are several "mini-excursions" of tens of nm, the obstacle returns to the filament. We consider this case to correspond to transient attachment of the filament to the obstacle. However, later in the time course (at around 11 sec), the obstacle has an excursion similar to that seen for repulsive potential. Eventually, the filament will catch up to the obstacle and the excursions will diminish.

Figure 2.5 shows the calculated force-velocity relations for the range of potentials considered. For all the potentials, the growth velocity lies at or below the BR prediction. This is expected from the assumption (Eqs. 3.9 and 3.10) that $k_{off} \leq k^0_{off}$: Eq.

2.14 implies that $\bar{k}_{on} - \bar{k}_{off} = k_{on}^0 \exp(-F\delta/k_BT) f(F) - k_{off}^0 f(F)$, where $f(F) \leq 1$. Then $\bar{k}_{on} - \bar{k}_{off} = f(F)[k_{on}^0 \exp(-F\delta/k_BT) - k_{off}^0]$, below the BR prediction. For all purely repulsive potentials, the force-velocity relation is essentially indistinguishable from the BR prediction. This again follows from Eq. 2.14, 3.9, and 3.10. For repulsive potentials Eqs. 3.9 and 3.10 imply that $k_{off}(r) = \bar{k}_{off} = k_{off}(0)$, so that $\bar{k}_{on} = k_{on}^0 \exp(-F\delta/k_BT)$ and the BR relation holds.

Simple-well potentials, as well as potentials having negative spikes and double wells (Figure 2.2b), lead to slowing of growth relative to the BR model in the positive (pushing) force regime. For a well depth of 5 k_BT, the zero-force velocity is about half of the free-filament velocity, larger than might have been expected from the $\exp\{-[U(r-\delta) - U(r)]/k_BT\}$ factor in Eq. 3.9, which is approximately $\exp(-5)$ in the case of the Gaussian spike when the obstacle is near the bottom of the potential well. The reason for the faster growth is that in the absence of external force, the obstacle is outside the well a substantial fraction of the time.

To see this, we assume fast obstacle diffusion and exploit the fact that the growth of the filament tip at velocity v toward the obstacle has the same effect on the distance distribution $P(r)$ as a weak external effective force $F_{eff} = k_BTv/D_{obst}$ [12]. This holds because the equation of motion for $P(r)$ in the presence of filament growth (taken to have a constant velocity, and using the Einstein relation) is $\partial P/\partial t = D_{obst}\partial^2 P/\partial r^2 + [F(r)D_{obst}/k_BT + v]\partial P/\partial r$, while the equation of motion in the presence of a constant force F_{eff} is $\partial P/\partial t = D_{obst}\partial^2 P/\partial r^2 + \{[F(r) + F_{eff}]D_{obst}/k_BT\}\partial P/\partial r$.

We assume the obstacle to be in either the region of the potential well, where we ignore polymerization, or in the region outside the well, where it polymerizes at the free-filament velocity v_0. This picture is most applicable to narrow wells, such as the "Negative Spike" treated in Figure 2.5c. The polymerization rate is then $v/v_0 = Z_{free}/(Z_{well} + Z_{free})$, where Z_{well} is the contribution to the obstacle's partition function from the well region and Z_{free} is the contribution from outside the well. We take

$$Z_{free} = \int_0^\infty exp(-F_{eff} \cdot r/k_BT) dr = \frac{k_BT}{F_{eff}} = \frac{D_{obst}}{v} \tag{2.21}$$

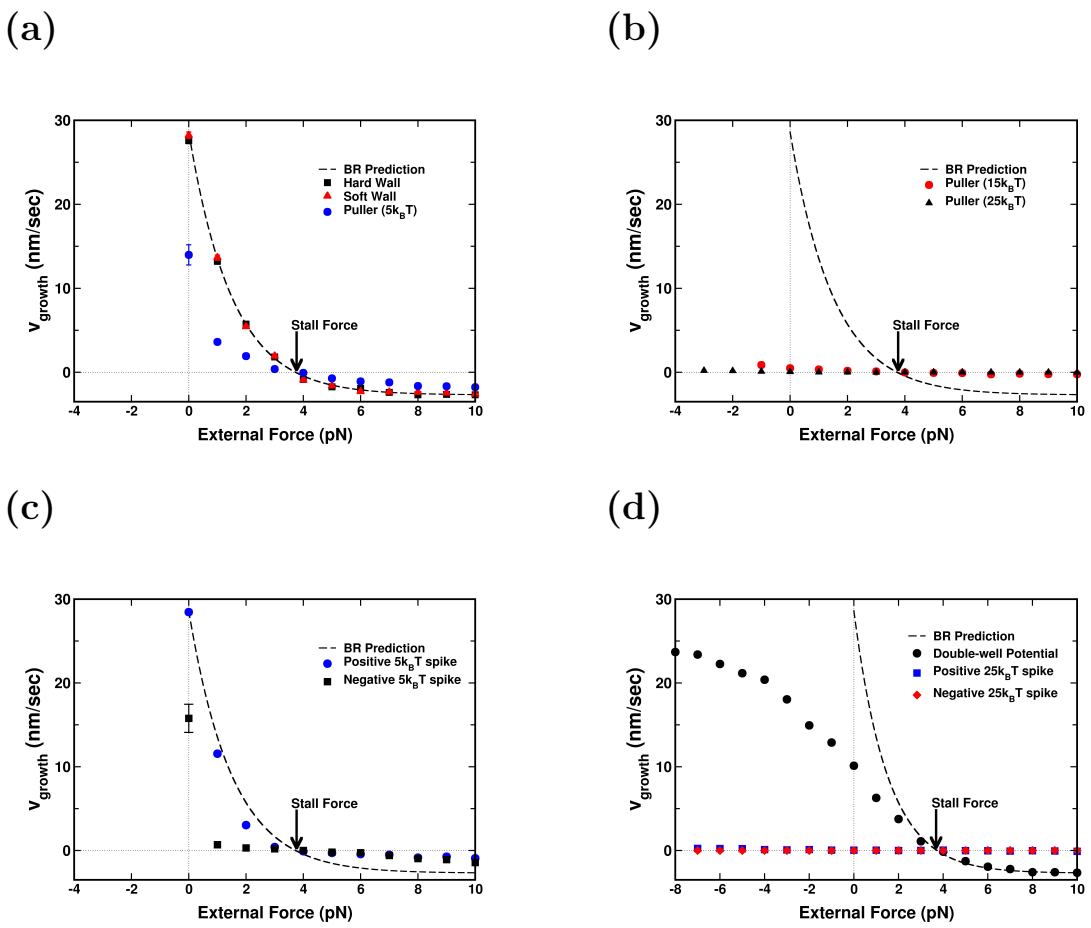

Figure 2.5: Simulated force-velocity relation for several different forms of filament-obstacle interaction potential. Error bars are smaller than the symbols, except indicated; and they are calculated by finding the standard deviation of the mean for growth velocity, from 20 different simulations of 20 seconds. The dashed line is the prediction of the BR model at large diffusion constant values for obstacle. Data points for pullers are shown out to forces where they detach from the obstacle. Frames (a) and (b) are for potentials in Figure 2.2a, while (c) and (d) are for potentials in Figure 2.2b.

where we have taken the integral to extend from 0 to ∞ for mathematical simplicity, which is valid as long as F_{eff} is weak. This gives

$$\frac{v}{v_0} = \frac{1}{1 + Z_{well}/Z_{free}} = \frac{1}{1 + Z_{well}v/D_{obst}} \tag{2.22}$$

The solution to this equation is

$$\frac{v}{v_0} = \frac{2}{1 + \sqrt{1 + 4\eta}}, \tag{2.23}$$

where $\eta = v_0 Z_{well}/D_{obst}$. Treating the "Negative $5k_BT$ Spike" as a square well of depth $5k_BT$ and width 2 nm, we obtain $Z_{well} = 2\ nm \cdot e^5$ and $v/v_0 = 0.52$, roughly consistent with the numerical results in Figure 2.5c. The growth velocity given by Eq. 2.23 is appreciable only if $\eta \lesssim 1$, so that $D_{obst} \gtrsim v_0 Z_{well}$. Therefore, even though $D_{obst}/k^0_{on}\delta^2 >> 1$, the growth velocity depends strongly on the diffusion coefficient.

For the potentials with $5k_BT$ wells, the velocity also decays more rapidly with opposing force than the BR relation predicts. For example, the "5 k_BT" curve in Figure 2.5a drops by nearly 75% already at 1 pN force, while the BR model and repulsive force fields drop by only about 50%. For the "Negative 5 k_BT" spike in Figure 2.5c, the drop is practically down to zero. This rapid drop occurs because the external force reduces the statistical weight of the free region, which becomes $Z_{free} = k_BT/(F_{eff} + F_{ext})$. Substituting this into Eq. 2.22 gives

$$\frac{v}{v_0} = \frac{2}{1 + \tilde{f} + \sqrt{(1 + \tilde{f})^2 + 4\eta}}, \tag{2.24}$$

where $\tilde{f} = Z_{well}F_{ext}/k_BT$. Even small values of F_{ext} can affect the velocity strongly, because of the Z_{well} factor in $\tilde{f}$. Solving Eq. 2.24, again using a square well of depth $5k_BT$ and width 2 nm, we find $v/v_0 = 0.014$ at $F_{ext} = 1$ pN, consistent with the very rapid drop seen in Figure 2.5c. When diffusion is very rapid, $\eta \to 0$, and

$$v/v_0 \simeq 1/(1 + \tilde{f}). \tag{2.25}$$

Taking $(1/v)(-dv/dF_{ext}) \geq 2\delta/k_BT$ at zero force (twice the BR value) as a definition of rapid decay with force, we find that rapid decay will occur when $Z_{well} \gtrsim 6$ nm.

For the double-well potential (Figure 2.5d), the velocity decays less rapidly relative to its $F = 0$ value than the BR prediction (although the magnitude of v_{growth} is always smaller than the BR result); in fact the drop is almost linear.

Another feature of the systems with potential wells is that they can polymerize processively under pulling (negative) force, over a limited time [75]. As expected physically, there is a tradeoff between maximum sustainable force and polymerization rate. High pulling force enhances polymerization, but at the same time accelerates detachment of the obstacle from the filament. For a $5k_BT$ potential depth, almost no pulling force can be sustained over 20 seconds (Figure 2.5a). But for a $15k_BT$ depth (Figure 2.5b), a force of about 1 pN can be sustained over 20 seconds. The growth velocity in this case is about 80% greater than the zero-force value, but much lower than for the 5 k_BT case. For the $25k_BT$ potential still larger pulling forces can be sustained, at an even smaller growth rate. Figs. 2.5(c) and Figure 2.5d show that the same trade-off occurs for potentials with spikes. The trade-off is explicitly illustrated in Figure 2.6. Frame a) shows how the maximum pulling force that allows a 20-second attachment period, depends on the depth of the potential well. Frame b) shows how the growth velocity depends on the well depth. These two plots show that large sustainable pulling forces on the obstacle (greater than about 1 pN) come at the expense of greatly reduced growth velocity. Pullers with a well depth of about $5k_BT$ grows only half as fast as a free filament, but can sustain essentially no pulling force. If the depth is larger than about $15k_BT$, which is needed to sustain pN forces, growth almost completely stops. The only form of potential used here that achieves a reasonable growth rate at a substantial pulling force is the double-well potential (Figure 2.2b). As shown in Figure 2.5d, this potential eliminates the trade-off between sustainable force and polymerization rate that is seen with other potentials. This is because the well is wide enough that polymerization can occur inside even a very deep well. If the obstacle is pulled toward the large-r end of the well, $U(r - \delta)$ and $U(r)$ do not differ greatly, so there is no significant slowing in Eq. 3.9.

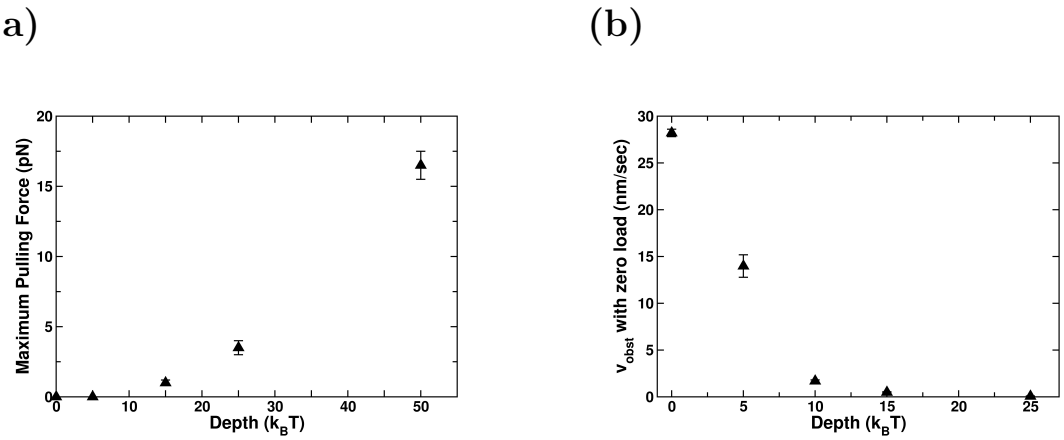

Figure 2.6: Effect of binding strength of single-well potential on a) the maximum pulling force allowing attachment up to 20 seconds, and b) the growth velocity at zero external load.

2.4 Discussion

Our main findings are the following:

- The ratio of the on- and off-rates depends on the details of the interaction potential with the obstacle on a nanometer scale (see Eq. 2.13). This implies that even at zero force, a deep well in the interaction potential can dramatically slow both polymerization and depolymerization. Polymerization is slowed because of the high-energy configuration assumed by the filament tip after addition of a new subunit, while depolymerization is slowed because removal of an existing subunit also leaves the filament in a high-energy configuration. Eq. 2.13 is automatically satisfied by calculations implementing the BR approximation that $k_{on}(r) = 0$ when the filament tip is within a distance δ of a hard obstacle with no attractive well, but $k_{on}(r) = k_{on}^0$ beyond that distance.

  Not all single-filament calculations in the literature treating obstacle motion explicitly have satisfied the constraint of Eq. 2.13. We note that Eq. 2.13 does not apply to calculations such as as those of Refs. [69], which ignored depolymerization. Ref. [71] assumed a variation of the on-rate resulting from the interaction potential with the obstacle, but it did not appear to satisfy Eq.

2.13. On the other hand, Ref. [75] used a relationship very similar to Eq. 2.13, in which the exponential factor corresponded to the energy difference between binding in two different positions in a double-well potential.

Some works treating force generation by actin networks stochastically have also treated smoothly varying tip-obstacle interactions [87, 88, 89, 90, 91, 92, 49]. In all of these works, actin polymerization was slowed by the obstacle. But none of the treatments satisfies Eq. 2.13 exactly. Ref. [87] used an approximate version in which the $U(r)$ term in the exponential of Eq. 2.13 is ignored. In Refs. [88] and [89], the mechanical energy, including the membrane deformation/position and states of actin filament bending, was minimized after each polymerization event. To evaluate the on-rate, the energy was reminimized with a hypothetical next subunit in place. The resulting energy difference ΔU was used in a Boltzmann factor slowing the polymerization. This approach is similar in spirit to Eq. 2.13, but differs in that the energy is minimized in calculating ΔU. In the context of the systems treated here, this would correspond to placing the obstacle, before and after the addition of the new subunit, at the minimum of the potential $U(r) + F \cdot r$. Then $\Delta U = F\delta$, giving a slowing of the growth velocity of a single filament by a factor of $\exp(-F\delta/k_BT)$. As found above, this is correct provided there is no attractive well in the potential.

Refs. [90, 91, 92, 49] used criteria based on force rather than energy difference. In such approaches, even plausible assumptions regarding the slowing of actin polymerization can lead to substantial errors in the stall force. For example, one can assume [49] that a filament tip experiences a linear force $F(r) = -k_c r\theta(-r)$ when in contact with the obstacle, and that this force slows polymerization according to

$$k_{on}(r) = k_{on}^0 \exp\left[-F(r)\delta/k_BT\right], \tag{2.26}$$

while $k_{off}(r) = k_{off}^0$ is not affected. This corresponds to applying the thermodynamic result Eq. 2.14, for the averaged rate $\bar{k}_{on}$, to the instantaneous rate $k_{on}(r)$. The force-velocity relation can be obtained exactly for this model in

the limit $D_{obst} \to \infty$. Using the same analysis as used to derive Eq. 2.16, but incorporating Eq. 2.26, we obtain

$$\begin{aligned}\bar{k}_{on} &= (k^0_{on}/Z)\int_{-\infty}^{\infty} \exp\left[-F(r)\delta/k_BT\right]\exp\left\{-[U(r)+F_{ext}\cdot r]/k_BT\right\}dr \\ &= (k^0_{on}/Z)\left[\sqrt{\frac{\pi k_BT}{2k_c}}e^{\{[F_{ext}-k_c\delta]^2/2k_ck_BT\}}\{1+\mathrm{erf}[\frac{F_{ext}-k_c\delta}{\sqrt{(2k_ck_BT)}}]\}+k_BT/F_{ext}\right]\end{aligned}$$

where $U(r) = k_c\theta(-r)r^2/2$ and

$$Z = \sqrt{\frac{\pi k_BT}{2k_c}}\exp\left(F^2_{ext}/2k_ck_BT\right)\{1+\mathrm{erf}(F_{ext}/\sqrt{(2k_ck_BT)})\}+k_BT/F_{ext}. \quad (2.27)$$

The stall force for this model can be obtained by numerically locating the zero of $\bar{k}_{on} - \bar{k}_{off}$.

In the limit of large stall force ($F_{ext} - k_c\delta >> \sqrt{2k_ck_BT}$), Eq. 2.27 simplifies. The error functions in Eqs. 2.27 and 2.27 approach unity, and the $1/F_{ext}$ terms can be ignored. Thus $\bar{k}_{on} \simeq k^0_{on}\exp\left(-F_{ext}\delta/k_BT\right)\exp\left(k_c\delta^2/2k_BT\right)$. Solving for $\bar{k}_{on} = \bar{k}_{off}$ we obtain

$$F_{stall} = (k_BT/\delta)\ln\left(k^0_{on}/k^0_{off}\right) + k_c\delta/2, \quad (2.28)$$

which exceeds the thermodynamic stall force by the amount $k_c\delta/2$. Numerically, both from Eq. 2.27 and from our stochastic simulations with a large but finite D_{obst}, we find comparable overestimates of the stall force in other parameter ranges. The overestimates are equally large in parameter ranges where filament-tip fluctuations dominate. For the spring constant assumed in Ref. [49] we obtain a stall force of 50 pN, about five times too high given the assumed actin concentration. We emphasize that these results hold only when thermal motion of the obstacle or filament tip is explicitly treated rather than being averaged out.

Why does Eq. 2.27, which appears to correctly implement the force dependence of actin polymerization by equating the instantaneous rates to the known results

(Eq. 2.14) for the average rates, fail to obtain the correct stall force? The reason is that although the force $F(t)$ acting on the tip of a filament polymerizing under an average force F_{ext} satisfies $\bar{F} = F_{ext}$, the fluctuating motion of the obstacle or the filament tip causes the tip to experience a range of forces described by a distribution $p(F)$, so that

$$\bar{k}_{on} = k^0_{on} \int_{-\infty}^{\infty} p(F) \exp(-F\delta/k_BT) dF \tag{2.29}$$

Since the exponential is convex upwards (the second derivative of $\exp(-F\delta/k_BT)$ is positive), $\bar{k}_{on}$ will exceed $k_{on}(\bar{F})$, leading to an overestimate of the stall force. If one assumes that $p(F) \propto \exp[(F-\bar{F})^2/2\Delta F^2]$ where ΔF^2 is the variance of F, Eq. 2.29 shows that $\bar{k}_{on} = k^0_{on} \exp[-\bar{F}\delta/k_BT] \exp[\delta^2\Delta F^2/2(k_BT)^2]$. Setting this equal to k^0_{off}, one finds

$$F_{stall} = (k_BT/\delta) \ln(k^0_{on}/k^0_{off}) + \Delta F^2\delta/2k_BT. \tag{2.30}$$

For force fluctuations induced by thermal motion in a harmonic potential, $\Delta F^2 = \Delta r^2 k_c^2 = k_c k_B T$, and Eq. 2.30 is identical to Eq. 2.28. On the other hand, if thermal motions of the filament tip or obstacle come from non-thermal sources, as in Refs. [90, 91, 92], force fluctuations could instead result from the geometrical constraints imposed on the individual filaments by the network structure. Then one might expect the bending-induced fluctuation of a given filament tip position to be $\lesssim \delta$; larger deformations would likely be evened out by the differences in growth velocity. As described in Appendix A, one can estimate the spring constant of a filament in the direction of motion as $k_{bend} \simeq 0.5\ \frac{pN}{nm}$. Then $\Delta F \sim k_{bend}\delta \lesssim 1.35$ pN, and the overestimate in Eq. 2.30 is $\lesssim 0.6$ pN, much smaller than for thermal force fluctuations.

- Provided that $k_{off}(r) \leq k^0_{off}$ and D_{obst} is large, no type of filament-obstacle interaction potential leads to polymerization faster than a hard wall; for monotonically decaying force fields the force-velocity relation is very near that for a

hard wall, which is described well by the BR prediction. These results follow from Eq. 2.14 and are confirmed by the simulations. For intermediate values of $D_{obst} \sim k_{on}^0 \delta^2$, we find that softer potentials accelerate growth slightly (see Figure A.3).

But when D_{obst} is very small, a soft potential can accelerate polymerization substantially. This was found in the simulations of [71], where a soft obstacle accelerated polymerization by about 100% using $D_{obst} = 0.0016 k_{on}^0 \delta^2$. To understand this physically, consider the case of zero external force. In the limit of a slowly varying potential, it is legitimate to ignore the randomness in polymerization and treat filament growth as occurring at a constant velocity. As described in Section 3.2, obstacle drag can then be included via an effective force $F_{eff} = k_B T v_{obst}/D_{obst}$ [12]. After a sufficiently long time, the probability distribution $P(r)$ will settle into a steady-state form $P(r) = \exp\{-[U(r) + F_{eff} \cdot r]/k_B T\}/Z$, where Z is the corresponding partition function. Then following the derivation of Eq. 2.16, and taking $f(r) = 1$ in Eq. 2.15 so that $\bar{k}_{off} = k_{off}^0$,

$$\begin{aligned} \bar{k}_{on} &= (k_{on}^0/Z) \exp(-F_{eff}\delta/k_B T) \int_{-\infty}^{\infty} \exp[-U(r)/k_B T] \exp[-F_{eff} \cdot r/k_B T] dr \\ &= \exp(-F_{eff}\delta/k_B T) k_{on}^0 \end{aligned} \tag{2.31}$$

Since $v_{obst} = (\bar{k}_{on} - k_{off}^0)\delta$, it follows that $v_{obst} = (D_{obst} x/\delta - k_{off}^0 \delta)$, where x satisfies the transcendental equation $x/\tilde{k}_{on} = \exp(-x) \exp(\tilde{k}_{off})$ and we define $\tilde{k}_{on,off} = (k_{on,off}^0 \delta^2/D_{obst})$. Therefore

$$\begin{aligned} v_{obst} = &\ (D_{obst}/\delta)\{W[\tilde{k}_{on} \exp(\tilde{k}_{off})] - \tilde{k}_{off}\} && (2.32) \\ \simeq &\ (D_{obst}/\delta) \ln(\tilde{k}_{on}/\tilde{k}_{off}) && (\tilde{k}_{on} >> 1,\ \tilde{k}_{off} >> \ln(\tilde{k}_{on})) \\ \simeq &\ (D_{obst}/\delta)[\ln(\tilde{k}_{on}) - \ln(\ln \tilde{k}_{on})] && (\tilde{k}_{on} >> 1,\ \tilde{k}_{off} \to 0) \end{aligned}$$

where the Lambert function W is the inverse of the function $x \exp(x)$. We have used the asymptotic expansion $W(x) \simeq \ln(x) - \ln[\ln(x)]$, valid when x is large

(very slow diffusion).

In cases of very slow obstacle diffusion, the simplified form Eq. 2.33 will hold if the ratio between the on- and off-rates is moderate. The physical content of this result is clarified by considering the work done in moving the obstacle. The work done per added subunit is $(v_{obst}k_BT/D_{obst})\delta$ where the first term is the force according to the Einstein relation. From Eq. 2.33 this equals $k_BT\ln(k^0_{on}/k^0_{off})$, which is the free energy released per added subunit [85]. Thus the process is 100% efficient in that all of the free energy of polymerization is used to push the obstacle against the drag force. If (k^0_{on}/k^0_{off}) is large, the velocity in Eq. 2.33 could exceed the hard-wall limit $2D_{obst}/\delta$ [12] substantially. For example, for a free-actin concentration of $10\mu M$, our parameters would predict that $(k^0_{on}/k^0_{off}) \simeq 100$, and the logarithm is greater than 4. Then the hard-wall limit would be exceeded by more than a factor of 2.

The simulations of Ref. [71] treated the case $\tilde{k}_{on} = 6.67 \times 10^2$ and $\tilde{k}_{off} = 0$. In this case, Eq. 2.32 gives $v_{obst} = 4.9D_{obst}/\delta$, while Eq. 2.33 gives $v_{obst} = 4.6D_{obst}/\delta$, both about a factor of two above the hard-wall limit and comparable with the value of $4.4D_{obst}/\delta$ found in Ref. [71]. This suggests that the analytic theory captures the key effects in these simulations.

- For relatively shallow attractive potentials the velocity can be a substantial fraction of the free-filament velocity at zero force, but decay rapidly with opposing force. This finding may help explain the results of experiments [22] studying small number of actin filaments growing against a hard wall, if the filament tips are weakly bound to the wall. The filaments propelled acrosomes attached to beads held in an optical trap (backwards). The filaments/acrosome/bead are moving rather than the obstacle, so as discussed above it is their motion that is considered. The growth velocity was found to drop off much more rapidly than expected from the BR model at forces of a few tenths of a pN per filament, especially at a $2\mu M$ actin concentration. We cannot treat their many-filament system within our model, so we consider a single filament grow-

ing against an obstacle with a force of a few tenths of a pN. Because the bead is trapped in potential well of spring constant $k_c \simeq 0.008 pN/nm$, the "free" contribution Z_{free} is different from that calculated in Sec. 3.2. The energy of the bead in the potential well, displaced a distance r from the minimum, is $k_c r^2/2$. Thus $Z_{free} = \int_0^\infty \exp(-F_{ext} \cdot r) \exp(-k_c r^2/2) dr$. Provided that $F_{ext} \geq \sqrt{k_c k_B T} = 0.2pN$, the reduction in Z_{free} from F_{ext} will exceed that from k_c, and it is reasonable to take $Z_{free} = k_B T/F_{ext}$ as in Sec. 3.2. Then Eq. 2.25 applies, and a force of few tenths of a pN per filament could reduce the velocity by a large factor if $Z_{well} \geq 15nm$. The validity of Eq. 2.25 requires that $\eta = v_0 Z_{well}/D_{obst} << 1$. In Ref. [22], v_0 was less than $20nm/s$, so a diffusion coefficient $\geq 600nm^2/s$ would be adequate.

Experiments on whole cells [30, 68] have shown that the growth velocity of lamellipodia drops very rapidly with opposing force. The velocity decay found here may contribute to this effect, but only if the filaments are sufficiently long to allow thermal fluctuations greater than $Z_{free} = k_B T/F_{ext}$ away from the obstacle. In this system, mechanical factors may be the dominant effect [68].

- Sustaining strong pulling forces at a significant rate of polymerization requires a deep, broad well in the filament-obstacle interaction. Actin filaments polymerizing under pulling force may have several functions. They could act as parts of force sensors, or as mechanical absorbers for rapidly generated forces from myosin motors [55]. It is also believed that actin filaments in the central region of endocytic sites in budding yeast exert pulling forces on the membrane [53, 49], and it is important to know if filaments can polymerize sufficiently quickly to generate a gel in the pulling region that can sustain the large stresses generated by the process. The behavior of actin filaments under pulling forces has been addressed by thermodynamic arguments [93] as well as kinetic models [55, 94] and simulations [95, 75]. Most of the calculations have predicted acceleration of polymerization by pulling force, but Ref. [95] found a competition between different conformational factors that could either slow or speed polymerization.

Experimental studies [96, 94, 55, 97] have shown that polymerization under pulling forces of several pN is possible if actin filaments are linked to the obstacle via formins. They suggest, on the whole, that pulling force accelerates polymerization if rotational constraints are absent. These models have included effects not explicitly included here, such as conformational changes of formins at the actin filament tip. Our finding that for narrow wells polymerization is incompatible with the ability to sustain large forces implies that in the systems where this phenomenon occurs, the interaction between the actin filament and the obstacle must have a broad minimum. Our models are too simple to quantitatively describe the three-dimensional geometry of a formin-tipped actin filament, but the broad minimum in our "double-well" potential may approximately mimic the conformational flexibility that appears to be at the heart of the phenomenon.

The calculations described here make several major approximations, including the treatment of just a single filament, and the modeling of the filament-obstacle interaction via simple potential energy functions. To make direct contact with experiments will require more complex calculations for many-filament systems. The present results can help make progress toward this goal by informing multiscale calculations such as those of Ref. [59, 61, 62, 63, 76, 64, 65, 98, 77, 68, 78, 66, 51, 79, 67, 99], which treat force generation by multifilament systems using a variety of approximations to include the single-filament force-velocity relation. The present results will provide useful guidance, especially in cases where different types of filament-obstacle interactions are present in the same system.

Chapter 3

Pulling force generation by ensembles of polymerizing actin filaments

3.1 Introduction

In many cellular processes that require large forces to generate membrane curvature, such as cell migration and endocytosis, actin polymerization is an essential factor [2]. Bending the membrane requires pushing and pulling forces in balance. Generation of pushing forces by actin polymerization has been studied extensively. Experiments have shown that polymerization of a single actin filament tethered between an immobilized formin and a myosin molecule can produce forces > 1.3 pN, close to the theoretical stall force under the experimental conditions [15]. Direct measurements of force generation by small growing bundles of about eight parallel filaments also revealed force generation, but the total stall force of 1 pN was surprisingly small [22]. Force measurements on growing branched actin networks *in vitro* using cantilevers [26] found the force-velocity relation of the network to have a load-independent growth phase over a range of 50-160 nN (corresponding to pressures of $\approx 0.18 - 0.5 \times 10^{-3}$ pN/nm^2) at a velocity of ≈ 72 nm/min, followed by a stalling phase at a force of $\approx 290nN$ corresponding to a pressure of about 10^{-3} pN/nm^2. Further experimental

evidence for actin pushing forces is given by bacteria such as Listeria, which form a long "comet tail" extensions that push them through the cytoplasm [100]. Studying a Listeria analog consisting of a protein-coated bead, Ref. [29] found fources corresponding to a stress on the bead surface of at least 2.5×10^{-4} pN/nm^2. Because the bead was attached to its actin tail, it was possible to study the force-velocity relation under both applied pushing and pulling forces. A linear increase of the velocity was found under applied pulling forces, and a slower drop for applied pushing forces. Due to the buckling of actin comet tail under large forces (greater than 4.3 nN), stall forces could not be reached in these experiments.

On the other hand, the processes by which actin polymerization generates pulling forces have received less quantitative study. Experiments on motile fluid vesicles propelled by actin comet tail [44, 101] found a force distribution dominated by inward pushing forces on the sides of the vesicle, and directional pulling forces at the rear of the vesicle. The maximum pulling pressure in Ref. [44] was about $\approx 3.5 \times 10^{-4}$ pN/nm^2. It was also found that a total net actin force (pulling + pushing) in the range of $\approx 0.4 - 4$ nN is essential to maintain the distorted shape of the lipid vesicle. Most of this was from inwards forces; the component along the direction of motion was very small. Measurements of force around podosomes, mechanosensitive adhesion cell structures that exert protrusive forces onto extracellular environment, show that protrusive forces from actin polymerization at the core and pulling forces from lateral acto-myosin contractility in the surrounding adhesion ring are required simultaneously for a single podosome to deform the substrate [47]. Endocytosis in yeast also requires large pulling forces from actin to overcome the high turgor pressure. Actin patches consisting of an Arp2/3-branched network [11] form during this process. The large pulling forces required to initiate invagination are generated only after the arrival of actin [48], suggesting that the network generates them. Actin force distributions extracted from electron-microscopy images of the membrane curvature during endocytosis reveal a relatively flat pulling-force distribution at the center of the endocytic patch with an estimated pulling pressure of about 0.5 pN/nm^2 and a required total pulling force of nearly $3000pN$ from the actin network [50]. The

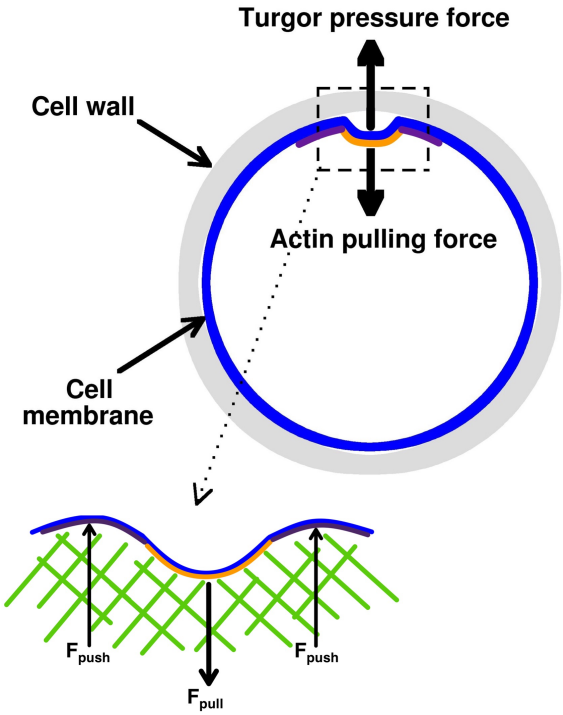

Figure 3.1: Schematic of the force balance on the cell membrane. Force from internal turgor pressure is the major opposer against curvature generation regulated by actin polymerization.

pulling-force region was surrounded by a ring of pushing forces. Furthermore, recent superresolution microscopy of the geometry of the process revealed the accumulation of the membrane-filament binding protein Sla2, within a central dot, surrounded by a ring the actin nucleator Las17 [49] (WASP homolog), suggesting a generic mode of pulling-force generation with enhanced actin polymerization in a ring-shaped region creating pulling forces at the center. Deleting the yeast fimbrin Sac6, which should reduce the stiffness of the actin gel [27] stops invagination [102], showing that a stiff gel generated by cross-linking between actin filaments is also critical for generating pulling forces. Reducing the turgor pressure by providing osmotic support across the plasma membrane reduces the requirement for actin filament cross linkers [103], presumably because the force requirement is lowered. This suggests that a stiff actin gel is required for pulling-force generation. Mutating Sla2 by deleting its actin-binding domain also stops the invagination process [102], suggesting that strong actin-membrane attachments are also crucial.

Although numerous theoretical models have described how actin polymerization generates pushing force [104, 105], generation of pulling forces has been studied only in a few models. These have been based on the assumption of enhanced actin polymerization in a ring-shaped region. It has generally been assumed that the total pulling force from actin filaments acting on the membrane is limited by the stall force of all the uncapped pushing filaments. In addition, most studies have assumed that the total force exerted by the actin network on the membrane vanishes, corresponding to overall force balance on the actin network. This assumption is justified by the smallness of the viscous and inertial forces acting on the actin network [51]. Force balance implies that there are two types of filaments, some of which pull and some of which push. Simple calculations based on the surface area of the invagination and the turgor pressure indicated that forces of over 1000 pN were required to drive invagination [106]. Subsequent analyses performed by fitting to observed membrane shapes, including force terms from membrane tension, membrane curvature, and curvature-generating proteins, gave estimates of ~ 3000 pN for the minimum actin pulling force required to sustain the invagination [52, 50].

Assuming an actin polymerization rate increasing outwards from the center of the endocytic patch, Ref. [51] used a continuum-mechanics model to show that even modest actin polymerization forces spread over a large ring can generate a large pulling-force density at the center by a force-amplification process. These calculations were extended in Ref. [50] to evaluate the actin growth profile to generate the required pulling forces. The validity of a continuous treatment of the discrete system of filaments and membrane, however, is not clear. Stochastic simulations of the growth of a rigid 3D actin network [53] assumed a uniform distribution of the actin nucleator Las17 in a ring-shaped region on the membrane. They also assumed that the filament growth velocity is determined by the average opposing force per filament. However, the distribution of the forces exerted on the membrane was not obtained in any of these calculations. Simulations based on realistic dimensions and molecular compositions obtained from super-resolution experiments found that a 3D branched network of actin filaments can produce forces exceeding 1000pN, enough to

overcome turgor pressure [49]. However, in this model, the actin filament stall forces may have been overestimated [107], which could lead to an overestimate of the pulling force. Although these models have confirmed the ability of an actin-nucleator ring to generate pulling forces, there has been no robust study of the mechanisms determining the magnitude of the pulling force. By force balance, the pulling force must be limited by the stall force of the pushing filaments. However, it is neither clear what fraction of this limit can be achieved practically, nor how rapidly the pulling force reaches its maximum value. In addition, there have been no detailed studies of the spatial distribution of the pulling force explicitly treating stochastic polymerization of individual filaments. Finally, the possibility of pulling filaments detaching from the membrane has not been treated to date. This process is plausible because of the large magnitude of the pulling force per pulling filament.

The key features that affect pushing-force generation, such as the free-monomer concentration A and the on/off rate constants k_{on}^0 and k_{off}^0, are important for pulling-force generation as well. The stall force obtained by thermodynamic arguments is given by

$$F_{stall} = (k_B T/\delta) \ln (k_{on}^0 \cdot A/k_{off}^0), \tag{3.1}$$

where k_{on}^0 and k_{off}^0 are rates for a free filament not interacting with an obstacle, A is the actin monomer concentration, and δ is the actin step size per added subunit. Thermodynamic analyis shows that the stall force is proportional to the number of filaments and is independent of the geometrical details of the growth process, a result confirmed by simulations [82]. Other studies confirmed that stall force is independent of the geometry of the polymerizing ensemble and different energy distributions. However, it has also been suggested that including ATP hydrolysis effect can reduce the actin stall force [42]. Lateral interactions [84, 83] can also affect the stall force. However, in branched actin networks such those at endocytic actin patches, the filament spacings of $\sim$10nm are large enough that lateral interactions are probably not important. Elasticity of individual actin filaments, and the actin network on whole, are also likely important for pulling forces. Fluctuations of the tips or bases of actin filaments are crucial for obtaining rapid network growth under moderate forces [23].

Here we calculate the pulling forces that a discrete array of cross-linked actin filaments with varying polymerization properties generates on a rigid obstacle. We evaluate the total magnitude of the pulling force, its spatial distribution, the dynamics of the force buildup, and the conditions that lead to detachment of the pulling actin filaments from the membrane. The scale and parameters of the model are chosen to correspond to endocytosis in yeast. We assume that there is a group of filaments at the center of the array whose zero-force growth velocity is low because their growing ends are strongly bound to the obstacle. When the remaining "pushing" filaments grow, the slower-growing filaments inhibit this growth via their linkage to the pushing filaments, and thus exert a pulling force on the obstacle. We vary several parameters, including the pulling filaments' binding strength and the actin gel stiffness, and evaluate the resulting effects on force generation and actin network deformation. We interpret our numerical results from this complete system of filaments, including "pushers" and "pullers", via a mean-force model that treats the pushers and pullers separately. In this model, the growth velocity is determined by the equality of the pusher and puller forces at a common velocity. We study the effect of transient attachments of the pushing filaments to the membrane on the magnitude of the pulling force. We evaluate the dependence of the time scale of force generation rate on the gel stiffness. Finally, we calculate the detachment rate of pullers as a function of their binding strength to the membrane. This model treats only the actin contribution to pulling forces. Additional contributions are probably generated by curvature-generating proteins such as clathrin. However, these are not sufficient to drive the process, as shown by the correlated electron-microscopy and light-microscopy studies of Ref. [48]. This work showed that no measurable membrane bending occurs without polymerized actin, suggesting that actin polymerization is the dominant factor generating pulling forces.

We find that strengthening the filament-obstacle binding by choosing deeper potential wells for the central filaments decreases the growth rate of the actin network in this region. This increases the total pulling force up to a maximum that is close to the sum of the stall forces of the surrounding pushing filaments. The pulling force

is maximal when the central filaments do not polymerize at all. We also find that the mean-force model accurately predicts the results of full system simulations for the total pulling force. Stiffening the actin gel reduces the total gel deformation, as expected intuitively, while stronger membrane attachments increase the deformation. Transient attachments of the pushing filaments reduce the total pulling force, so maximum force is produced when their potential is purely repulsive. We find that the time required for the maximum pulling force to build up is roughly inversely proportional to the gel stiffness. Finally, softening the gel, or weakening the binding of the central filaments, can lead to membrane rupture despite the total binding energy of several hundred k_BT or more of the puller filaments to the membrane.

3.2 Model

We model the growing actin network as a 12×12 square array of filaments with a 10-nm spacing, interacting with a flat moving obstacle (see Fig. 3.2). The geometry is motivated by the measured architecture [49] of the endocytic actin patch, but the dimensions are taken somewhat smaller to reduce the computational load. We treat a fixed number of uncapped filaments rather than treating the dynamics in which filaments are nucleated by Arp2/3 complex and subsequently capped. Thus we model the force-generation properties of the filaments that are uncapped at a given time. The obstacle, corresponding to the combination of the cell wall and membrane, contains a central patch of the filament-membrane binding protein Sla2 (yellow circles), surrounded by a square band of nucleation promoting factors (NPFs), such as the yeast WASP homolog Las17 (purple circles). As the filaments grow, pulling and pushing forces act on the gel in the directions indicated by black arrows, deforming the gel. In order to elucidate the physical mechanisms as clearly as possible, we focus on the steady-state force and the buildup to steady state, rather than treating the feedback loops [53] that cause the polymerized-actin count to drop to zero after reaching a peak. We also leave out possible effects of hydrolysis of actin subnits at filaments tips. The possible consequences of this effect are analyzed under **Discussion**.

Each filament tip interacts with the obstacle via a smooth potential, which can be either purely repulsive or have an attractive well. A 6×6 square subset of filaments at the center of the array is assumed to have a deep well in the filament-obstacle interaction, corresponding of binding to membrane-bound Sla2. The outer filaments have a purely repulsive potential or one with a shallow well. We adopt a picture similar to that of Ref. [108] where the filament "free length" L protrudes beyond a gel region, which we treat as linear and elastic. We define the filament bases (black squares) as being a distance L in from the tip. At this point the filaments are crosslinked, either by Arp2/3 complex or another crosslinker, and the gel begins (see Fig. 3.2). For simplicity, we ignore variations in L from filament to filament. The initial filament lengths are staggered randomly within a subunit length interval, so that every filament starts to grow with a length of one subunit plus a random number smaller than a subunit. The filaments polymerizate and depolymerize stochastically at rates that depend on the distance between the filament tip and the obstacle. The rates are assumed to be bounded by the free-filament values. The filament tips also diffuse rapidly in the direction perpendicular to the obstacle, describing bending fluctuations of the filaments. The corresponding lateral motion is not treated explicitly because it does not affect the interaction potential with the obstacle. The filament orientation fluctuates from perpendicular to the obstacle to parallel to the obstacle, placing corresponding limits on the motion of the filament tip in the direction perpendicular to the obstacle surface. Similarly, diffusion of bases describes elastic deformation of the actin gel induced by the differing polymerization rates of the filaments. In treating this effect, crosslinks between bases of adjacent filaments are modeled as springs that constrain the relative motion of filaments in the direction perpendicular to the obstacle. Both the tip and base motions are described using biased Brownian dynamics driven by the filament-obstacle interaction and a linear restoring force. This force is determined by the filament rigidity for tip fluctuations and the actin gel stiffness for the motions of the bases. The obstacle moves stochastically in response to forces from the filaments, via biased Brownian motion.

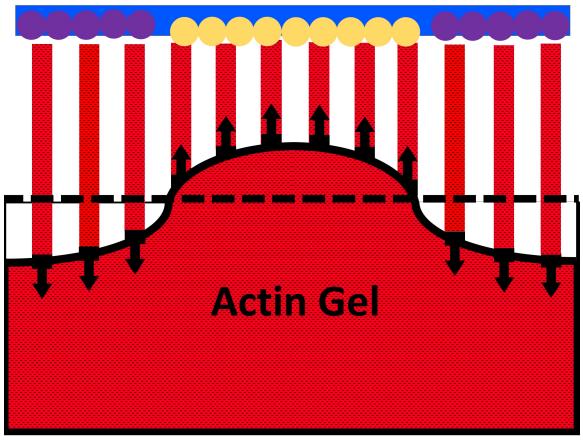

Figure 3.2: Schematic cross section of 12×12 filament array. A 6×6 square of central pullers are bound to the membrane via protein Sla2 (yellow circles) and the surrounding 108 filaments in the ring of actin nucleators Las17 (purple circles) are uncapped growing filaments exerting pushing forces on the membrane, with corresponding reaction forces on the actin gel. Solid black line denotes surface of deformed actin gel, while dashed line denotes undeformed surface.

3.2.1 Filament-obstacle interaction

Fig. 3.3 shows the interaction between a single actin filament and the obstacle. The default filament direction makes an angle $\theta = 35°$ with the normal to the obstacle, consistent with the 70° Arp2/3 branching angle [10]. The azimuthal angle is unspecified because it does not affect the calculation results. To simplify the calculations, we project the directional growth of the actin filament on the z direction (the direction of the obstacle motion), with $\delta \cos(\theta)$ being the projected actin step size, and only treat the z-direction growth explicitly. Thus we ignore lateral motion of the filament tips along the membrane resulting from polymerization. The distribution of pulling and pushing forces on the obstacle is determined by the differences in polymerization and bending/deformation between different filaments. To keep track of these differences, we define for each filament a "filament height" given at any given time step by

$$h = n\delta \cos(\theta) + \Delta z_{tip} + \Delta z_{base} + h_o \tag{3.2}$$

where n is the number of subunits added to the filament up to that time step, Δz_{tip} is the filament tip fluctuation, and Δz_{base} is the filament base fluctuation; h_o is the initial

height of the filament, which equals the length of one subunit plus a random number between zero and one subunit length, to treat staggering. Results of simulations without staggering are given in the Supplementary Material.

The height h corresponds to the distance that a given filament tip has moved during the simulation. Thus the values of h do not correspond to actual filament lengths, since they will exceed the size of the gel after a sufficiently long simulation time. The time dependent gap r between the obstacle at position z_{obst} and a given filament tip is then

$$r = z_{obst} - h \tag{3.3}$$

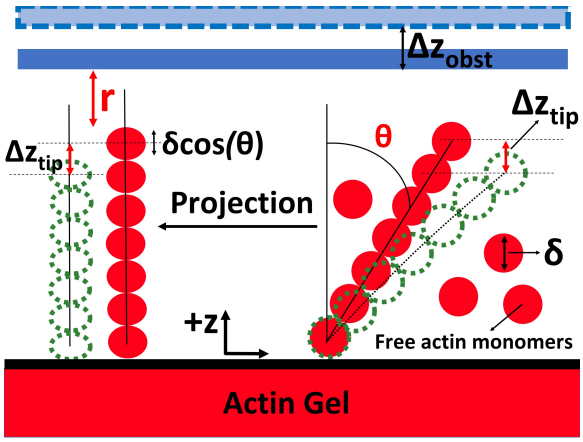

Figure 3.3: Schematic of the filament-obstacle interaction. r is distance between filament tip and obstacle, δ is actin monomer size = 2.7nm, Δz_{obst} is obstacle position fluctuation, and Δz_{tip} is the filament tip position fluctuation in the $\pm z$ direction during a given time step. The base of the filament is located on the surface of the actin gel and also fluctuates in the $\pm z$ direction by an amount Δz_{base} during a time step.

We treat the interaction between the obstacle and the filament tip with smooth potential functions, as shown in Fig. 3.4, having the form

$$U(r) = Ae^{-\kappa_1 r} - Be^{-\kappa_2 r} \tag{3.4}$$

or

$$U(r) = Ae^{-\kappa_1 r} - Ce^{-[\kappa_3(r-r_1)]^2} - De^{-[\kappa_4(r-r_2)]^2} \tag{3.5}$$

Here, A, B, C, D, κ_1, κ_2, κ_3, κ_4, r_1, and r_2 are constants, while r is the variable

distance between filament tip and obstacle. Having a non-zero B in Eq. 3.4 adds an attractive component to the potential that represents filament-obstacle binding. We refer to this type of potential as a "simple well". A "double-well" potential is obtained by choosing positive C and D in Eq. 3.5. In the double-well potential the broad minimum might represent conformational flexibility of a protein binding the actin filament to the membrane, or the presence of two different binding sites [75]. The corresponding forces exerted on the obstacle by the filaments are

$$F(r) = -\frac{dU}{dr} = A\kappa_1 e^{-\kappa_1 r} - B\kappa_2 e^{-\kappa_2 r} \tag{3.6}$$

and

$$F(r) = A\kappa_1 e^{-\kappa_1 r} - 2C{\kappa_3}^2(r - r_1)e^{-[\kappa_3(r-r_1)]^2} - 2D{\kappa_4}^2(r - r_2)e^{-[\kappa_4(r-r_2)]^2}. \tag{3.7}$$

The pusher filaments in the outer ring of the array have either only repulsive potential terms or a repulsive potential plus one with a shallow well. The puller filaments in the central region have a deep well in their interaction potential.

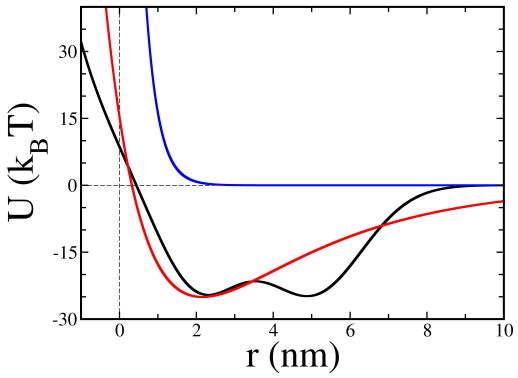

Figure 3.4: Filament-obstacle interaction potentials, given by Eq. 3.4 and Eq. 3.5. Blue curve: "pusher potential" (Eq. 3.4), with A=54.66 $pN{\cdot}nm$, B=0, and κ_1=0.9 nm^{-1}. Red curve: "puller potential" with a well depth of $25k_BT$, with parameter values (Eq. 3.4) A=358.01 $pN{\cdot}nm$, B=294.72 $pN{\cdot}nm$, κ_1=0.9 nm^{-1}, κ_2=0.3 nm^{-1}. Black curve: "double-well potential" (Eq. 3.5) with A=54.66 $pN{\cdot}nm$, C=100 $pN{\cdot}nm$, D=100 $pN{\cdot}nm$, $\kappa_3 = 0.643\,nm^{-1}$, $\kappa_4 = 0.544\,nm^{-1}$, $r_1 = 2$ nm, and $r_2 = 5$ nm.

3.2.2 Stochastic treatment of actin polymerization

The actin on-rate, k_{on}, has been defined in most previous models as an average over a time long compared to the time scale of filament-tip and obstacle fluctuations. Here, such an average is not appropriate because of the large force fluctuations that occur from the combination of Brownian motion and the rapid variation of the force between the filaments and the obstacle. Therefore we treat instantaneous rates that apply to a particular position of the filament tip relative to the obstacle. Thermodynamic analysis [107] shows that the position-dependent rates must satisfy the relationship

$$\frac{k_{on}(r)}{k_{off}(r-\delta)} = \exp\{-[U(r-\delta)-U(r)]/k_BT\} \cdot \frac{k_{on}^0}{k_{off}^0} \tag{3.8}$$

where k_{on}^0 and k_{off}^0 are free-filament on and off rates respectively. In order to concretely determine k_{on} and k_{off}, we assume that their magnitudes never exceed the free filament on and off rate values, so that

$$\begin{aligned} k_{on}(r) &= k_{on}^0 \cdot \exp\{-[U(r-\delta)-U(r)]/k_BT\} \quad \text{if} \quad U(r-\delta) > U(r) \\ k_{on}(r) &= k_{on}^0 \quad \text{if} \quad U(r-\delta) < U(r) \end{aligned} \tag{3.9}$$

$$\begin{aligned} k_{off}(r) &= k_{off}^0 \cdot \exp\{-[U(r+\delta)-U(r)]/k_BT\} \quad \text{if} \quad U(r+\delta) > U(r) \\ k_{off}(r) &= k_{off}^0 \quad \text{if} \quad U(r+\delta) < U(r) \end{aligned} \tag{3.10}$$

3.2.3 Stochastic time evolution of obstacle and filament positions

The obstacle position, and filament bending/base deformation, evolve in time according to random thermal forces and deterministic forces from the filament-obstacle interaction potential, as well as linear restoring forces for the tips and bases of filaments. For conceptual simplicity, we use a "filament-centric" approach, where the actin gel is assumed to be stationary, while the obstacle moves. To treat force genera-

tion in the presence of a stationary obstacle, the calculated motion can be reversed by a simple coordinate transformation, assigning the actin gel diffusion coefficient to the obstacle. The diffusive motions of the obstacle and filament coordinates are treated by the discrete form of the Langevin equation (Ref. [80], Chapt. 3):

$$\Delta z_{obst} = \alpha\sqrt{24\Delta t}\sqrt{D_{obst}} + \frac{D_{obst}}{k_B T}\Delta t[F_{tot} + F_{load}] \tag{3.11}$$

$$\Delta z_{tip_i} = \alpha'\sqrt{24\Delta t}\sqrt{D_{tip}} + \frac{D_{tip}}{k_B T}\Delta t[-F(r_i) - k_{bend}\Delta z_{tip_i}] \tag{3.12}$$

$$\Delta z_{base_i} = \alpha''\sqrt{24\Delta t}\sqrt{D_{base}} + \frac{D_{base}}{k_B T}\Delta t[-F(r_i) - k_{elas}\Delta z_{base} + k_{elas}\Delta z_{nn}] \tag{3.13}$$

Here D_{obst} is the obstacle diffusion coefficient, D_{tip} and D_{base} are the filament tip and base diffusion coefficients, F_{tot} is the total force from the filaments acting on the obstacle, F_{load} is the external force applied on the obstacle (used only in the "Mean-Force" model described below), Δt is the time step, k_{bend} is the tip bending stiffness, k_{elas} is the filament-base spring constant embodying the elasticity of the actin gel, and Δz_{nn} is the sum of the displacements of the nearest-neighbor filament bases, relative to a central filament. α, α', and α'' are random numbers uniformly distributed between $-\frac{1}{2}$ and $\frac{1}{2}$, so that $< \alpha^2 >=< \alpha'^2 >=< \alpha''^2 >= \frac{1}{12}$. Displacements in consecutive time steps are uncorrelated.

3.2.4 Choice of parameters

The parameters are given in Table 3.1. On the basis of the actin gel size of $\sim 10^2$ nm vs. the $3nm$-size actin monomers, the inverse proportionality of diffusion coefficients to size would suggest $D_{gel} = D_{mon}/30 = (5 \times 10^6\ nm^2/sec)/30 = 1.6 \times 10^5\ nm^2/sec$; where D_{mon} is the actin monomer diffusion coefficient [109]. However, using an obstacle diffusion coefficient this large would be extremely computationally demanding, and for this reason we use a smaller value $D_{obst} = 10^4\ nm^2/sec$. We believe that this value is large enough to capture the key physical mechanisms since the dimensionless ratio of $t_1 = \delta^2/2D_{obst}$ (the time that takes the obstacle to diffuse the length of one actin step size) to $t_2 = 1/A \cdot k_{on}^0$ (the time for one free-filament subunit to

add), $t_1/t_2 = \delta^2 A k_{on}^0/2D_{obst} = 0.008$, is very small. Here A is the actin monomer concentration and k_{on}^0 is the free-filament on-rate constant (see Table 3.1). The diffusion coefficients D_{tip} and D_{base} are expected to be much larger than D_{obst} because the moving entities are much smaller than the actin gel. Again, for computational practicality we use smaller values of D_{tip} and D_{base}, which are still 10 times larger than D_{obst}, We obtain $a = 10nm$ for the filament spacing from the estimated number of actin filaments 300 [110] at an endocytic patch with radius $R = 75nm$.

We obtain the bending spring constant as $k_{bend} = 3k_BTL_p/L^3 \sin(\theta)^2 = 4.17\ \frac{pN}{nm}$ [111]. $L_p = 17.5\mu m$ is the persistence length of an actin filament [112] and as discussed above L is the free length of the filament beyond the gel surface. We take L to have a typical value of 54 nm, corresponding to the 20 subunits of a typical actin filament in endocytic actin patch. (The estimated number of actin filaments at an endocytic patch is taken to be 300 [110], with a total of 6000 actin monomers [1]). We assume that L remains constant during the polymerization process, as crosslinkers bind to newly grown parts of the actin gel near the membrane.

To obtain the actin-gel spring constant k_{elast}, we use elasticity theory to calculate the elastic restoring forces for a configuration of filaments where alternating filaments are displaced in opposite directions. We begin with the deformation $u(\vec{r})$ at the surface of an elastic gel $u(\vec{r})$ resulting from a point force $f(\vec{r}) = \delta(\vec{r})$. For a material with Poisson ratio σ and Young's modulus E the displacement (Ref. [113], Chapter 1) is

$$u(\vec{r}) = \frac{A}{r}\hat{r} \tag{3.14}$$

where $A = (1+\sigma)(1-\sigma)/\pi E$, We assume $\sigma = 1/2$ corresponding to an incompressible actin gel, so $A = 3/4\pi E$. To obtain the restoring forces for given displacements, we invert this result using a 2D Fourier transform. For u_k, we obtain

$$u_k = \int_{-\infty}^{\infty} u(\vec{r}) e^{-i\vec{k}\cdot\vec{r}} d^2r = \frac{3}{4\pi E}\int_0^{\infty}\int_0^{2\pi} \frac{1}{r} e^{-ikrcos(\theta)} d\theta r dr = \frac{3}{2E}\int_0^{\infty} J_0(kr) dr \tag{3.15}$$

where $J_0(kr)$ is the Bessel function of first kind. The Bessel-function integral is $1/k$

(Ref. [114], Chapter 8.41), so that $u_k = 3/2kE$. More generally,

$$u_k = \frac{3}{2Ek} f_k, \tag{3.16}$$

where f_k is the Fourier transform of the force. To obtain k_{elas}, we consider a specific set of displacements in a square lattice of spacing a nm. Taking each filament to be at a point $\vec{r} = (ma, na)$ (integer m,n), we define $u_{(m,n)} = +u_0$ if $m + n$ is even and $u_{(m,n)} = -u_0$ if $m + n$ is odd, so that nearest neighbors are displaced in opposite directions. This displacement can be written as $u_{(m,n)} = u_0 \exp(i\vec{K} \cdot \vec{r})$, where $\vec{K} = (\pi/a, \pi/a)$. Since the magnitude is $K = \sqrt{2}\pi/a$, Eq.3.16 gives a force density of

$$f(\vec{r}) = f_0 \exp(i\vec{K} \cdot \vec{r}) \tag{3.17}$$

where

$$f_0 = \frac{2\sqrt{2}\pi E u_0}{3a}. \tag{3.18}$$

On the other hand, the force density obtained using k_{elas} is

$$f(\vec{r}) = \pm 4 \times 2 \times k_{elas} u_0 / a^2. \tag{3.19}$$

Comparing Eqs. 3.17 and 3.18 gives

$$k_{elas} = \frac{\sqrt{2}}{12} \pi a E. \tag{3.20}$$

The Young's modulus for the actin gel is $E = 0.14\ pN/nm^2$ [50]. Thus Eq. 3.20 obtains the baseline value for the actin gel spring constant as $k_{elas} = 0.53\ pN/nm$.

3.2.5 Validity of assumptions

Here we discuss the potential impacts of the main simplifying assumptions that we have made:

Table 3.1: Symbol definitions and parameter values.

Symbol	Definition	Value
δ	Actin step size	2.7 nm
A	Bulk actin monomer concentration	5.3 μM(Ref.[115])
k_{on}^0	Free filament polymerization constant	11.6 s^{-1} μM^{-1} (Ref. [86])
k_{off}^0	Free filament depolymerization constant	1.4 s^{-1} (Ref. [86])
$D_{obst} = D_{gel}$	Obstacle diffusion constant	10^4 nm^2/s
D_{tip}	Filament tip diffusion constant	10^5 nm^2/s
D_{base}	Filament base diffusion constant	10^5 nm^2/s
k_{bend}	Tip bending spring constant	4.17 pN/nm
k_{elas}	Gel deformation spring constant (medium stiffness)	0.53 pN/nm
E	Actin gel Young's modulus	0.14 pN/nm^2 [50]
Δt	Simulation timestep	$5 \times 10^{-10} s$
F_{stall}	Filament stall force	7.03 pN
θ	Angle between filament tip direction and normal to obstacle	35°
$U(r)$	Potential of interaction between filament tip and obstacle	varies
$F(r)$	Force exerted on obstacle by filament	varies
F_{load}	External force on obstacle	varies
v_{growth}	Filament growth velocity	varies
r	Gap between filament tip and obstacle	varies
a	Spacing of filaments in square lattice	10 nm (deduced from Ref.[110])
z_{obst}	Obstacle z coordinate (height)	varies
z_{tip}	Filament tip z coordinate (height)	varies
z_{base}	Filament base z coordinate (height)	varies

- **Assumption of a sharp boundary between pusher and puller filaments.** Because the protein patches assemble stochastically, the boundary between the pusher and puller filaments will be blurred. In the regions where there are roughly equal numbers of pullers and pushers, the forces will oppose each other and the "smeared" force density will be reduced relative to the force densities in the pushing and pulling regions. This will lead to a reduction in the magnitude of the total pulling force that can be obtained.

- **Ignoring lateral component of polymerization.** This could have at least two effects. First, filament tips of pushers could move into the puller region. This would blur the boundary between pushers and pullers, reducing the total pulling force as described above. Second, if the filament tips are anchored strongly enough in the membrane that lateral motion is inhibited, forces could build up that would slow the polymerization of the pusher filaments. Again, this would reduce the total pulling force.

- **Treatment of the actin network as an elastic gel.** Viscous flow of the actin network will inhibit its ability to exert a distribution of pushing and pulling forces, once again reducing the magnitude of the total pulling force. It will have effects similar to that of using a softer elastic gel. The viscosity of the actin network at endocytic actin patches is not known, but the magnitude of the effect is discussed in **Conclusions**.

- **Absence of hydrolysis effects in model.** If subunits at filament tips hydrolyze and release inorganic phosphate before a new subunit is added, the pusher-filament stall force will be reduced [42]. The rates of hydrolysis and phosphate release are not known for subunits at filament tips. However, as the opposing force increases, the rate of subunit addition will slow, increasing the likelihood of release occurring before subunit addition. Therefore the total pulling force, even for very tightly bound pullers could be significantly below the value predicted from the thermodynamic stall forces of the pusher filaments.

3.3 Results

3.3.1 Force generation and gel deformation of a 12×12 square array of cross-linked filaments

The simulations for our system of $6 \times 6 = 36$ pullers and $12 \times 12 - 36 = 108$ pushers begin with all the filaments having a height randomly distributed within a subunit length. Pushing and pulling forces develop as the pushers and pullers grow at different rates. The pulling force is defined as the sum of all of the forces on the pulling filaments, taken negative when the force is pulling on the filaments. Figure 3.5 shows the time course of the total pulling force for systems with different puller-obstacle interaction potentials (see Fig. 3.4), and a range of values of the actin gel stiffness. The total pushing force (not shown) almost entirely balances the pulling force. We thus expect the total pulling force to be less than the sum of the pusher stall forces, about 760 pN:

$$F_{max}^{push} = 108 \times F_{stall} = 108 \times [k_BT/\delta \cdot cos(\theta)] \ln (A \cdot k_{on}^0/k_{off}^0) = 760pN. \qquad (3.21)$$

where A is the free-actin concentration. Weak filament-obstacle binding as in $5k_B$T potential generates very small forces. As the well depth increases, the pulling force approaches the limiting value of 760 pN. However, even for potentials as deep as $50k_BT$, the pulling force is substantially below the limiting value. Modifying the gel stiffness translates to lowering the concentration of actin filament cross linkers. This does not change the asymptotic total pulling force, but stiffer gels generate larger pulling forces earlier in the process. In addition, soft gels can lead to detachment of the pulling filaments from the obstacle, as occurs in the "$25k_BT$ soft" curve at about 1.8 sec, where the force suddenly drops to zero. This effect is described in detail below.

The total gel deformation is defined as the difference between the average base position of all the pullers and that of the pushers. Fig. 3.6 shows the gel deformation over time for different puller potentials and gel rigidities. Strengthening the central

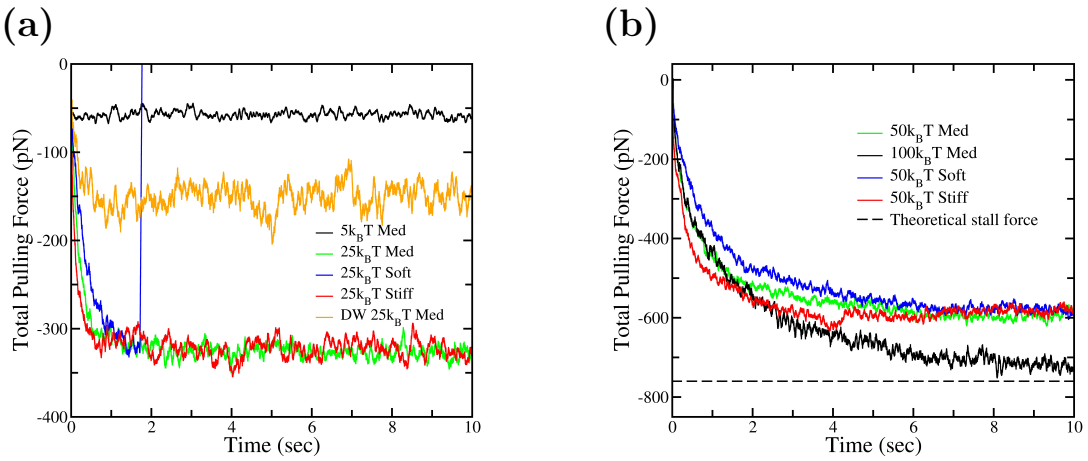

Figure 3.5: Sample runs showing total force from pullers over time, with different well depth and gel elasticity factors. Curves are averaged over 50ms length steps. Medium elasticity level corresponds to baseline $k_{elas} = 0.53pN/nm$; Soft and stiff k_{elas} values are half and double the baseline.

filament attachments and softening the gel both lead to larger gel deformations. The loss of force seen in Fig. 3.5, resulting from rupture of the softer gels at early times, corresponds the sudden loss of deformation in Fig. 3.6 at about 2 sec. Our results thus suggest that softening the gel leads to larger gel deformation, and higher rupturing rates.

An estimate of the time that takes the force to build up to near its maximum value (t_{bu}), or equivalently the time required to reach maximum deformation, can be obtained using dimensional analysis. The maximum force F_{max} is determined by the gel deformation and the actin gel properties. Taking it to be proportional to the total gel deformation Δu_z, and the actin gel Young's modulus E implies that $F_{max} = \Delta u_z \cdot E \cdot R$. where $R = 60nm$ is the radius of the actin gel in our model. Assuming that filaments grow at their zero-force values up until the stall point, we have $\Delta u_z = k_{on}^0 \delta \cdot t_{bu}$. Then

$$t_{bu} = \frac{F_{max}}{k_{on}^0 \delta \cdot E \cdot R} \tag{3.22}$$

The inverse proportionality of t_{bu} to E is seen in Figures 3.5a and 3.5b, where the force and deformation reach their maximum values for stiff gels faster than for softer gels. The numerical values predicted by Eq. 3.22 are not expected to be accurate,

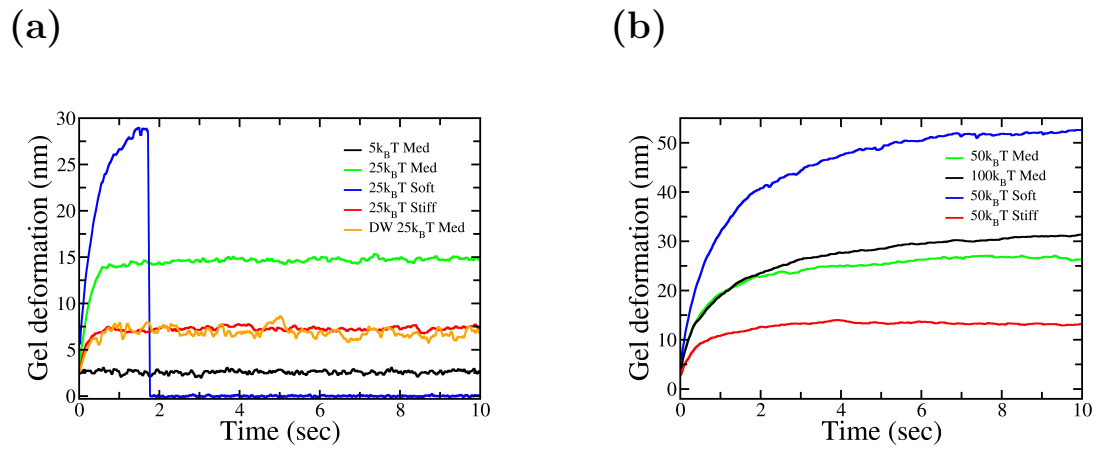

Figure 3.6: Gel deformation vs. time, for different puller depths and elasticity factors. Softer gels deform further and faster, and have higher chances of rupture.

but t_{bu} is estimated to about 1/2 sec for the case of the medium gel and a $50k_BT$ puller.

We also find that softening the gel increases the extent of actin polymerization. Fig. 3.7 shows the number of subunits added to all of the filaments in the array during the course of the simulation. We compare different gel stiffnesses and potential depths at a given value (270 pN) of the force, $\approx 80\%$ of the maximum force for $25k_BT$ pullers. The total amount of actin polymerization is increased by 160% for both $25k_BT$ and $50k_BT$ pullers going from a stiff gel to a soft one. In addition, $\approx 43\%$ more actin is polymerized for a medium gel at the same force of 270 pN when the pullers' potential depth is halved from $50k_BT$ to $25k_BT$. This number is smaller for soft and stiff gels ($\approx 26\%$). The black "No obstacle" bar corresponds to the amount of polymerization obtained after 0.5 sec (the average time it takes for the force with $25k_BT$ pullers to reach $\approx 80\%$ maximum) if no pullers are attached to the obstacle.

3.3.2 Effects of transient attachment of pushers to obstacle

It is believed that the WASP family of proteins, and their yeast homologue Las17, create weak transient attachments between filament tips and membrane [116]. We thus study the effect of adding a potential well to the pusher potentials on the magnitude of the pulling force. Fig. 3.8 shows the magnitude of the total pulling force as

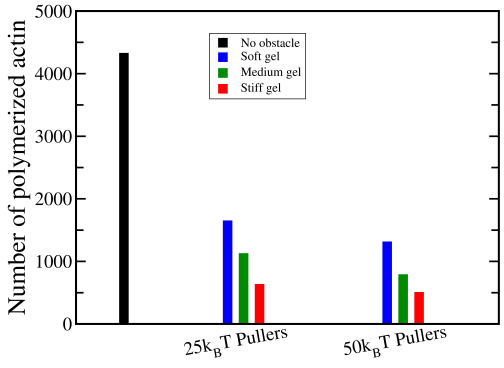

Figure 3.7: The total amount of actin polymerization when the force reaches 270 pN, for different stiffness levels and puller depths. Softening the gel increases the actin polymerization amount. Strengthening the pullers' binding to the membrane decreases the actin polymerization amount. Black bar shows the amount of actin polymerization for a 12×12 array of free filaments, i.e. in the absence of an obstacle.

a function of the pushers' well depth. For both $25k_BT$ and $50k_BT$ pullers, the force drops as pushers binding to the obstacle becomes stronger, and the fractional effect is larger for weaker puller potentials. At a well depth of $10k_BT$, the drop in total pulling force corresponds to about 1 pN per pusher. Thus the total pulling force is significantly stronger when interaction potentials of pushers are purely repulsive.

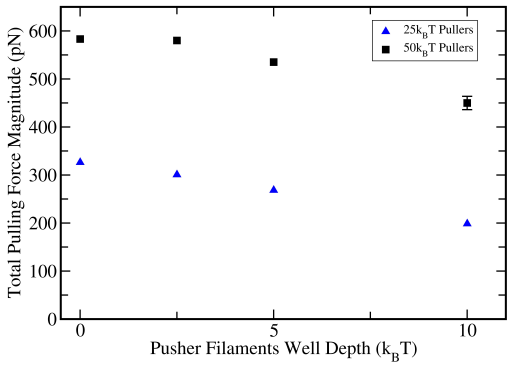

Figure 3.8: The effect of a potential well for pushers representing their transient attachments to the obstacle on the force production.

3.3.3 Force distributions

To reveal more completely the force balance between the pulling and pushing region, we present the spatial distribution of the forces using heat-map diagrams. Because of the stochastic nature of our simulations, the distributions obtained over a finite simulation (Fig. 3.9a) display noticeable fluctuations. To show the systematics of the distributions more clearly, we create symmetrized force distribution heatmaps by averaging the filament forces over symmetrically related subsets (Fig. 3.9b). For example, the symmetrically averaged force for a filament with coordinates (x, y) includes contributions from filaments at $(\pm x, \pm y)$ and $(\pm y, \pm x)$. We consider the case of $50 k_B T$ pullers, which gives close to the maximum pulling force. We see a fairly flat distribution in the pushing region (blue) balancing the total pulling force in the center (red). finite averaging time (about 1 pN) relative to more inner pullers; this can be due to the larger restoring forces from filament base displacements between the most outer pullers and the neighboring most inner pushers.

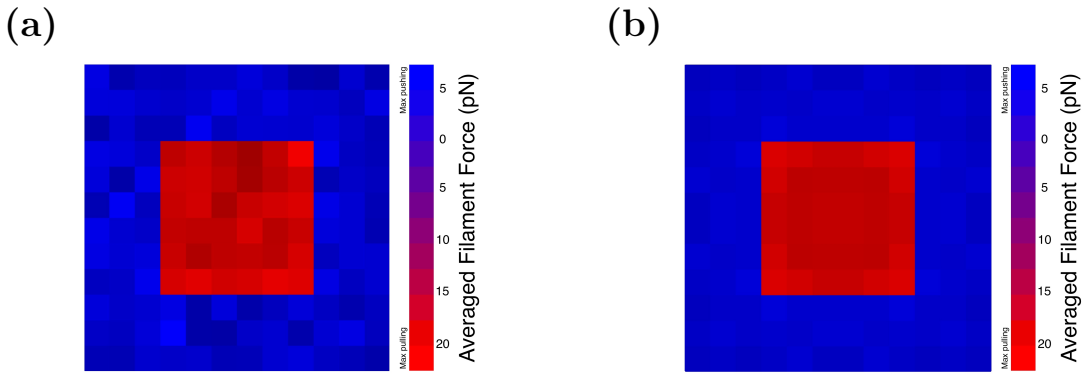

Figure 3.9: Heatmap diagrams of the force distribution of an array with $50 k_B T$ pullers. Simulation time is 10 seconds. We reduce the randomness of these distributions by averaging forces of filaments that are located on symmetric coordinates with respect to each other.

Figure 3.10 shows a cross section of the force distribution along a row in the middle of the array, for four different potentials. The magnitudes of the pulling forces are always less than the average maximum force per pulling filament

$$F_{stall} \times \frac{n_{pushers}}{n_{pullers}} = \frac{760\ pN}{36} = 21.1\ pN,$$

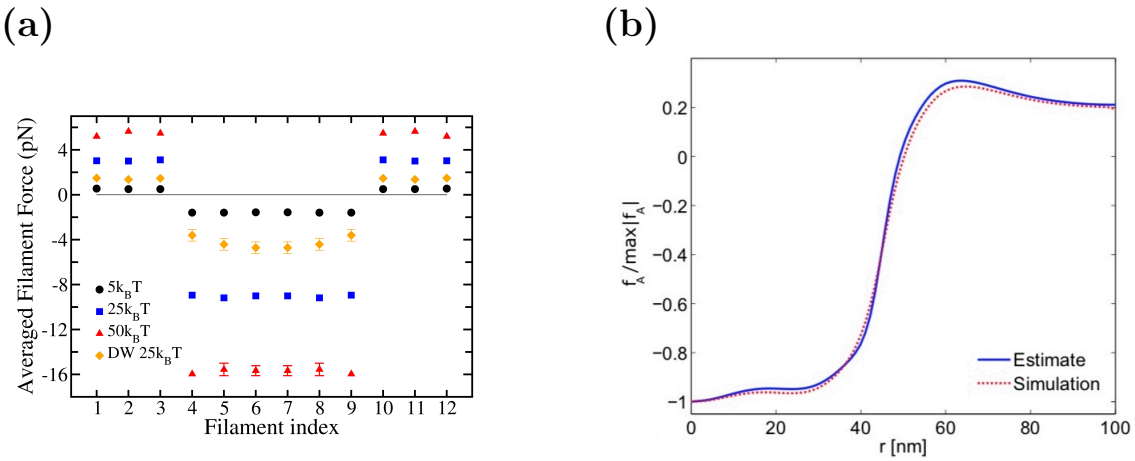

Figure 3.10: a) Comparison of force distribution profiles of a cross section of array, with medium gel stiffness and for different puller potentials. Error bars are smaller than the symbol size except indicated. b) Force distribution profiles extracted from electron microscopy images of the shapes of invagination (D. J. Tweten. et. al) shows a relatively flat distribution of forces in both pulling and pushing region.

obtained by assuming that all the pusher forces equal the stall force and the pulling force exactly balances the pushing force. The pulling and pushing force distributions are relatively flat in all cases except the double well potential. We believe this holds because in arrays with single-well pullers, all pulling filaments must grow at the same velocity once steady state is reached; since force determines growth velocity, all pullers must also experience the same force, and the force distribution is flat. In contrast, double well potentials have a velocity that is nearly force-independent after the pulling force reaches a certain magnitude [107]; therefore a range of forces is compatible with a certain velocity, so equality of growth between pulling filaments does not necessarily lead to a flat distribution of force. This is seen in the "DW" data points in Fig. 3.10.

The force distribution extracted from EM images of invagination shapes [50] (Figure 3.10b) shows a flat distribution over the pulling region similar to our prediction . However, the experimental force profile shows a $\approx 30\%$ hump in actin force density at the edge of the pushing region ($r \approx 50 - 80$ nm) which would correspond to about 1 pN force per pusher for $50k_BT$ case in Fig.3.10a. We do not see this hump in our simulation results.

Figure 3.11 shows the time evolution of the force distribution for the case of

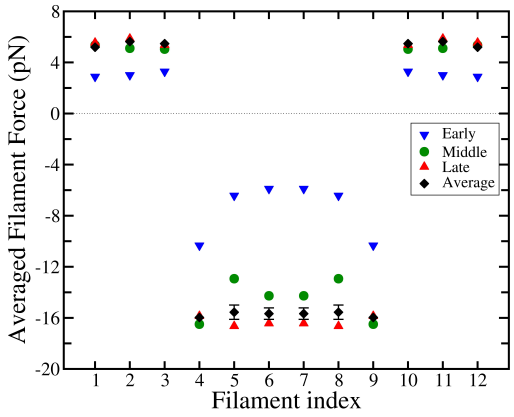

Figure 3.11: Time development of the force distribution of a middle row, with 6×6 array of $50k_BT$ pullers. Early stage (blue triangles) corresponds to the average force within 1-2 sec time interval, middle stage (green circles) 5-6 sec, and late stage (red triangles) is 9-10 sec, in a 10 second-long simulation. Black diamonds are the full time averaged force. Error bars on full time average data points are smaller than symbol size, except indicated.

$50k_BT$ pullers. The "Early" stage shows the forces averaged over the 1 second to 2 second interval of a 10-second long simulation. As seen in Fig. 3.5b this stage is well before steady-state, explaining why the distribution has not reached its asymptotic constant value. The filaments at the edge of the pulling region show enhanced forces at this stage. We believe this occurs because at early stages of the simulation, strong forces have not built up, so the force dependence of polymerization can be ignored. Then all the pullers will have added roughly the same number of subunits, and all the pusher filaments will have added a constant number of subunits (larger than the value for the pullers). The corresponding gel deformation will have a constant value in the puller region and a different constant value in the pusher region. Maintaining the difference between these deformations requires a force dipole at the boundary between the pusher and puller regions, which we believe explains the peak in the force seen in the "Early" results. The "Late" stage is closer to the asymptotic one, as the network approaches steady-state. The "Middle" stages has force peaks similar to those seen in the "Early" results, but also has a bump in the middle whose physical origin we do not know.

3.3.4 Mean-force theory

To clarify the mechanisms determining the magnitude of the pulling force, we study a simplified mean-force model based on the force-velocity relations of separate puller and pusher ensembles. In the full system simulations, 108 pushers and 36 pullers exert force on the obstacle, and the forces they exert on the obstacle are determined by the time-varying gaps between the filament tips and obstacle. On the average, the magnitude of the force felt by the the pushers equals that felt by the pullers. In the mean-force model, there are two force-velocity relations $v_{push}(F)$ and $v_{pull}(F)$, where the constant F (defined as always positive) is the magnitude of the time averaged total force felt by either the pullers or the pushers. We calcuate $v_{push}(F)$ and $v_{pull}(F)$ by performing pusher-only or puller-only simulations using an external force (pushing or pulling) of magnitude F. The magnitude of F corresponding to the joint system fo pullers and pushers is determined by the condition that $v_{push}(F) = v_{pull}(F)$. In other words, the pushers' velocity equals the pullers' velocity at a common force value. The value of F where the curves cross is obtained by linear interpolation from a finite set of force calculations. Fig. 3.12 shows the curves of $v_{push}(F)$ and $v_{pull}(F)$, as well as the comparison between the predicted force from mean-force model with that of the full-system simulations. As is clear from Fig. 3.12a, large pulling force will be generated by slow-growing pullers, which brings the crossing point between the F-V curves in Fig. 3.12a down and to the right. On the other hand, slowing the growth of pushers will bring the crossing point down and left, reducing the force. As Fig. 3.12b shows, the mean-force model closely predicts the results of simulations with a full array of filaments, over a range of puller potentials. This result suggests that the time variation of the forces from pushing filaments may not crucially impact the growth velocity of the pullers, and vice versa.

3.3.5 Effect of central-region growth on the pulling force

As the analysis of Section 3.4 shows, a large pulling force will occur when the puller filaments slow pusher filaments' growth by a large factor. The magnitude of force

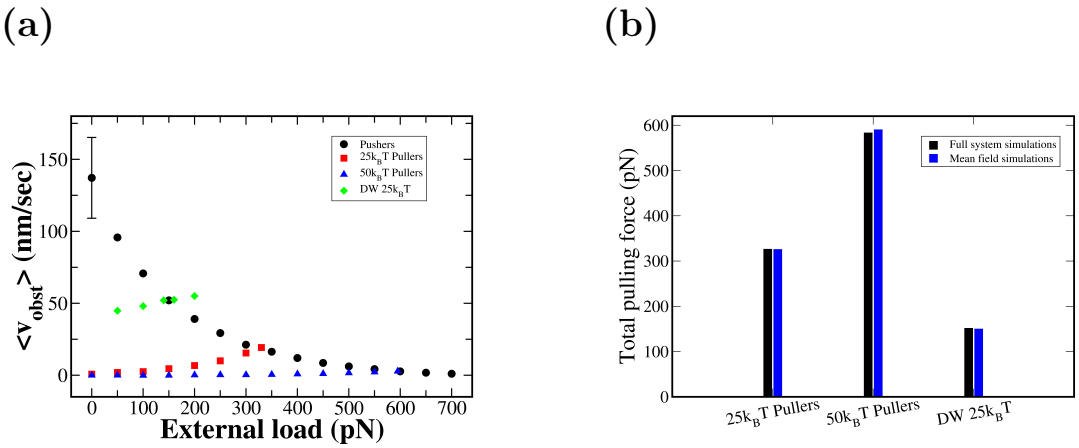

Figure 3.12: a) F-V plots of mean-force simulations of 108 active pushers with passive pullers (black points) and 36 active pullers with passive pushers (red, blue, and green points) with different potentials. Force at the crossing point of pusher and puller curves is the generated force predicted by mean-force model. b) Comparison of mean-force model to simulations with all filaments actively interacting with obstacle.

produced by the central filaments is maximized when pushing filaments reach their maximum force production capacity. This is limited by their stall force, since there is no mechanism for shrinking the pusher filaments. As a result, the maximum force occurs when the puller filaments' growth stops completely. Fig. 3.13 shows the relationship between total pulling force and average growth velocity of the central filaments. As the plot shows, even a growth rate as low as 10% of the free filament velocity can reduce the generated force substantially, by $> 40\%$.

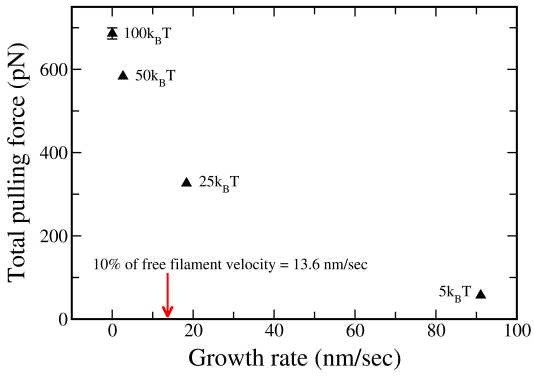

Figure 3.13: Total pulling force vs. central filaments growth rate. Maximum force is generated when pullers slow pusher filaments growth by a large factor.

3.3.6 Obstacle-gel detachment

Our finding of obstacle-gel detachment in same parameter ranges is surprising, given the magnitude of the potential and the number of filaments. Consider the case of a completely rigid, solidly anchored gel. Standard reaction rate theory [117] gives an analytical estimate of the escape time of the obstacle from the potential well:

$$\Delta t_{escape} = \frac{w^2}{D_{obst}} exp\left[\frac{\Delta U}{k_B T}\right] \tag{3.23}$$

Here w and ΔU are defined in Figure 3.14, where a positive external force of 335 pN (which caused detachment in Fig.3.5 above) pulls on a 6×6 array of rigid pullers with $25 k_B T$ potential wells and staggered initial alignment. In this case, $w \approx 5\ nm$, $D_{obst} = 10^4$ nm^2/sec, and $\Delta U \approx 180 k_B T$. Thus, Eq. 3.23 gives a very long time of $\approx 4 \times 10^{75}$ sec for the obstacle to detach from these pullers, so detachment essentially never happens. Consistent with this prediction, when the actin gel is stiff and the binding energy is $\geqslant 25 k_B T$, our simulations find that obstacle-gel detachment never occurs during 10-second simulations. However, softening the gel or weakening the puller-filament binding can lead to detachment before steady state is reached, as was seen in Figures 3.5 and 3.6 for $25 k_B T$ soft case. Thus a flexible actin network behaves differently from rigid networks in that it detaches more easily from the obstacle.

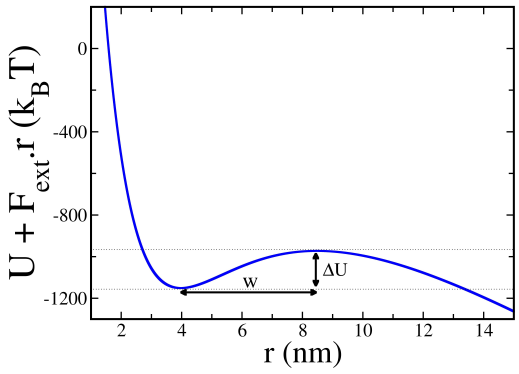

Figure 3.14: Total obstacle interaction potential from a 6×6 array of pullers with $25 k_B T$ wells plus potential from an external pulling force of 335 pN on the obstacle; w and ΔU are parameters used in Eq. 3.23.

In a particular simulation with $25k_BT$ pullers in a gel with medium elasticity, with an external pulling force of 335 pN on the obstacle, the obstacle tears apart from the gel after about 6.5 seconds. To understand the origin of this effect, we look at the distribution of r, the gap between filament tips and obstacle, during a few time steps right before the rupture happens. Figure 3.15 shows frames of a heat-map plot of the distribution of r for the pullers. Larger r values (greater stretching) have redder pixels. Frame a) is at a time well before rupture, to show the baseline appearance of the distribution. Frames b) through m) span 12,000 time steps, corresponding to 6 microseconds. The number of red pixels increases gradually during this period, indicating the appearance of possible detachment nucleation points around the tip of the actin filaments. The accumulation of these nucleation points from the right bottom corner eventually spreads over the entire pulling region, and the obstacle detaches completely. This is reminiscent of the process of a crack between two dissimilar materials due to stress concentration at the edge of the crack.

Some light can be shed on the effect of gel stiffness on the detachment process via the "Griffith" theory of the critical stress for fracture [118]. In the Griffith theory, the stress σ_c required to propagate a crack of length l_c is given by

$$\sigma_c = \sqrt{2E\gamma/\pi l_c} \tag{3.24}$$

where γ is the energy density associated with breaking the bonds along the crack. In this criterion, σ_c increases with E, consistent with our finding that stiff gels do not detach from the membrane. In applying it to the actin-filament system, we take γ to be the ratio of the puller potential depth to the area a^2 per filament. Since we are studying an incipient crack, we take $l_c = a = 10$ nm. For a puller potential well depth of $25k_BT$, using the value $E = 0.140\ pN/nm^2$, we obtain $\sigma_f = 0.095pN/nm^2$. By comparison, the stress at a force of 335 pN, for which detachment occurs, is $\sigma = 0.17pN/nm^2$. Given that in the simulation system there is not a well-defined preexisting crack, this level of agreement is reasonable.

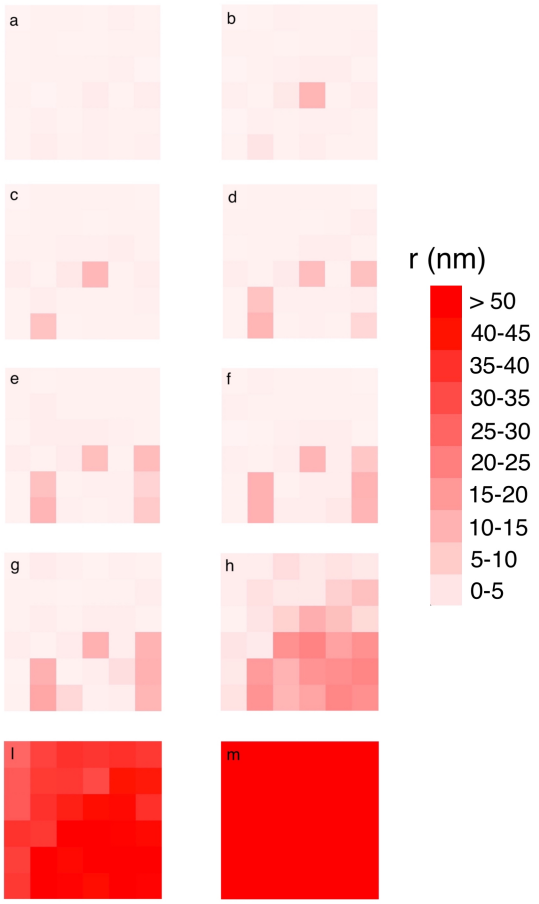

Figure 3.15: Distribution of r-values for pullers with $25k_BT$ binding in a medium-stiffness gel. Redder pixels correspond to larger r values. Frame a is the baseline distribution, at a time well before the rupture. Frame m is the distribution after the obstacle detaches completely. Frames b through m span 12000 time steps, a total of 6 microseconds. Accumulations of nucleation points around several filament tips in the pulling region, which takes place in a time in the order of microseconds, can lead to detachment.

3.4 Conclusions

The pulling force generated by an actin filament array results from the difference in growth properties between puller and pusher filaments. Large pulling forces are generated if the velocity of pullers at a given force is far below that of pushers. When the pullers do not grow at all, the total pulling force is maximized and equals the sum of the stall forces of the pushing filaments, as expected on thermodynamic grounds. A mean-force model treating pushers and pullers separately with constant forces reveals in more detail how the pulling force is determined by the difference between the puller and pusher force-velocity relations. It accurately predicts the total pulling force from full-system simulations, suggesting that time statistics of the force generation are not important for the final results.

One mechanism that can lead to slower growth of pulling filaments is strong binding to the obstacle. As the binding becomes weaker leading to faster puller-filament growth, the pulling force drops rapidly (Fig. 3.6. A similar effect would be expected from viscous flow of the actin gel. Fig. 3.13 shows that a growth rate of 13.6 nm/s is sufficient to slow polymerization considerably. Considering our model system to have a radius of about 60 nm gives a shear rate of 0.2s^{-1}. The stress in the puller region is about $20\text{pN}/100\text{nm}^2$. Then substantial force reduction would occur if the actin gel viscosity becomes less than about $1\text{pN-s}/\text{nm}^2 = 10^6\text{Pa-s}$. This value is much larger than any that have been previously measured. However, the viscous properties of actin networks at the very high densities present in endocytic actin patches have not been explored. Pulling forces are also maximized when the pushers' interaction potential with the obstacle is monotonically repulsive, which gives the largest growth velocity [107]. Transient attachments of the pushers to the obstacle slow their growth and thus inhibit pulling force generation. Even the largest forces obtained in our simulations, $\approx 760\ pN$, are smaller than the $1000\ pN$ forces required for endocytosis.

The steady-state force distribution profiles reveal a complete force balance between pushing and pulling regions, and fairly constant force densities over the pulling and pushing regions. They are consistent with the force profiles obtained from measured

membrane deformations [50]. The time evolution of the force distributions show enhanced forces at the edge of the pulling region at early stages, part of a dipole of forces surrounding the interface between the pusher and puller filaments. The force distributions could be measured using a combination of superresolution microscopy and suitable designed molecular force sensors. If a force sensor could be inserted into Sla2, and the signal from the force sensor measured using superresolution microscopy, a rough picture of the force distribution in the central Sla2 region could be obtained.

In the steady-state limit, the magnitude of the pulling force is independent of the actin gel stiffness, provided that obstacle-gel detachment does not occur. However, large forces are obtained at earlier times for stiff gels. This suggests that invagination should be slowed by mutations reducing the number of crosslinkers. The endocytic event could also be aborted completely because the actin patch has a finite lifetime, which may not be long enough to allow the maximum force to build up. This is consistent with requirement of the yeast fimbrin homolog *Sac*6 for endocytosis in yeast [103, 102]. In Ref. [102], more than 70% of the endocytic sites in the mutants were found to have a flat membrane profile. The majority of the remaining ones invaginated to a distance of ≈ 100 nm, but then retracted. The "retraction phenotype could result insufficient force building up during the lifetime of the actin patch. The slower buildup of force for the soft gels could also prevent endocytosis if viscous flow of the gel is important. Flow of the gel during the period of force buildup might prevent the force from ever becoming large enough to overcome the turgor pressure.

Detachment of pullers from the obstacle could completely disrupt the force-generation machinery. We find that detachment does not occur for rigid gels. But for soft gels, it does occur. The mechanism appears to consiste of an initial "nucleation" event in which one or more filament tip move out of the potential well binding them to the obstacle. The detachment then spreads over a microsecond time scale, in a mechanism analogous to crack propagation in a solid. These results suggest that softening the actin gel driving endocytosis in yeast by mutations reducing the number of crosslinkers could cause actin gel detachment from the membrane, aborting the endocytic event. This mechanism could provide an alternate explanation of the findings of

Refs. [103, 102]. The detachment mechanism could be distinguished from the direct effect of gel softening by tracking the motion of patches of the actin proxy Abp1, in $Sac6\Delta$ cells. If the detachment mechanism operates, the patches should move into the cell rapidly; if the direct effect of gel softening are more important, the patches should remain at the membrane.

We also find that the actin count is increased by either softening the gel or reducing the puller binding energy. We are not aware of data showing the effect of gel softening on the actin count, but an extreme version of reducing the puller binding energy is obtained in $Sla2$ deletion mutants. In these experiments, extensive actin accumulation occurs in the form of "comet tails" [56, 119].

Chapter 4

Simulation methods

In this chapter, I elaborate on the programming aspects of my research, by interpreting the steps in the simulation code, segment by segment. C++ is the language we chose to write our programs with; and for visualization purposes, we chose OpenGL, the great compatible graphical language for C++ users. Here in this chapter, first, I present the link to a C++ code that I wrote for a 10-second-long simulation of network growth. It seems to be the more appropriate decision to not include the hundreds of lines of code in this chapter, so that in case of the need for physical printing of the dissertation, less harm to the planet will originate from this action. Thus, here, I introduce various model parameters and explain the implications and reasoning behind different functions, loops, and structures. With the wish for it to be a tool for future students in their learning phase, if they refer to these codes.

The link to the sample C++ code (main_final_sample.cpp) for generating multiple simultaneous threads that run over different cores of the CPU (in this sample code, this number is 8, but it can be any number as high as 40, which was the number of available cores at the time):

https://www.dropbox.com/s/46lnbc4lcayoq9v/sample.cpp?dl=0

What this simulation generally does, is to create an array of 12×12 elastic actin filaments, that increase in length one actin step-size at a time stochastically (polymerizing) and decrease similarly (depolymerizing), against a fluctuating stochastically treated flat obstacle. The obstacle and the tip of these filaments interact with a po-

tential that has a well for a central 6×6 square array of filaments, and for the rest of the 12×12 array, the potential is purely repulsive. The stochastic growth of the filaments and the motions of the obstacle, filament tips, and filament bases are all implemented via the discrete form of the Langevin equation. This code then calculates the magnitude of force for each filament at every time step, to calculate and report the magnitude of total pulling and pushing forces, the force buildup curves in time, and force distributions.

Lines 1-12: The code starts in lines 1-12 by defining the C++ header libraries. From line 14 onwards, different parameters in the form of 1-dimensional (vector) or 2-dimensional arrays are defined and initialized. In some lines of the code, the comments in green are provided for additional helpful information.

Line 16: The number of actin filaments in the array $n_{filament}$ is defined, as well as the number of filaments in the central pulling region ($n_{central}$). For a 12×12 square array, then the number of filaments on a row is defined in line 19. $seed_1$ is an integer that will be re-written every new run to generate a certain set of random numbers to be used in our stochastic calculations. It is chosen to have a fixed value for control over reproducibility of each run.

Lines 23 and 24: Define parameters that later will be used in the potential function. These parameters define the shape of the filament-membrane interaction potential.

Line 26: Number of time steps in the simulation, to be skipped for every value at line 27, when writing the data in the output text files. This keeps the files from getting too big.

Line 28: Defines a number which will be used in nesting two for loops inside each other, to avoid the RAM over-flowing problem, with array sizes that surpass the computational limit (see **lines 474-483** for discussion on how to choose this number).

Line 30: The size of each time step (dt) is defined. Also, $t_{equilibrium}$ is the time that we wait before beginning to calculate time averages, to ensure that the system has evolved long enough to be near the steady-state. For example, for simulations that were 10 seconds long, most plots of various quantities vs. time showed that 3

seconds is a reasonable estimate for time that takes most systems of actin filaments to reach equilibrium. t_{break} is a time that will be defined later, to record the time-step that the pulling region of the actin network has broken apart from the membrane.

Lines 37-61: Define model parameters for stochastic treatments of the obstacle motion, the motion of filament bases, and the motion of filament tips. Diffusion coefficient values are related to the values of the motility factor with the Einstein relation, $D = \mu k_B T$, where D is the diffusion coefficient (in nm^2/sec), and μ is motility (in $\frac{nm}{pN \cdot sec}$). θ is the angle between the direction of branched filaments' elongation and the normal direction to the membrane, taken to be 35° accounting for the 70° Arp2/3 orientations. This affects the polymerization step size; accounting for projection of lengths and displacements on the xy plane perpendicular to the membrane. So, $\delta \cdot cos(\theta) = 2.2nm$ is the correct step size, with $\delta = 2.7nm$. Further, $\beta = \frac{1}{k_B T}$.

Lines 45 and 56: Give values of k_{elas} and k_{bend} parameters, which are discussed in Chapter 3. Additionally, all parameter values are set or calculated based on values published in existing literature (references can be found in the model section in Chapter 3). They are given in units of picoNewtons (pN) and nanometers, so for example the energy unit is $pN \cdot nm = 10^{-21} J$.

Line 61: Defines an array (S) with size equal to the number of filaments. This array is assigned to the sum of the displacements of the base positions for every filament relative to the bases of the adjacent filaments (**Line 605**). This parameter is necessary to track the actin gel deformation at the base level, which we assume to be the actin gel surface level.

Lines 63-76: Model parameters are named in a self-explanatory way. dz_{bend} is the filament tip fluctuation, and dz_{elas} is the filament base fluctuations, at every time step.

Lines 83-85: Uniform random numbers that are generated as randomly and independently as possible, for every time step in every run. More than 1000 different sets of 144 random numbers at every time step with 2×10^{10} time steps in a 10-second-long simulation.

Line 88: Defines the array (*initial_staggered_length*) that will be filled with random numbers assigned later to be added to the initial height of each individual filament. This creates the randomly distributed staggered initial alignment of actin filaments.

Lines 89-91: Define critical variables r, U, and F: the gap between the obstacle and the filament tip, the interaction potential between the filament tip and the obstacle, and the filament force on obstacle. The functions for potential and force are defined later as well.

Lines 98-101: Define the array of symmetrized filament force values (*F_symmetrized*), to calculate the time averaged filament forces along with averaging spatially for filaments located on symmetrical positions across the lattice (more details in Chapter 3).

Line 121: Parameter *ss* defined in line 121, the scaling constant in the calculations for the random part of the Langevin equation, is used to update the position of the membrane, filament tip, and filament bases. Simulation time steps are uncorrelated, which leads to a certain height (limit) on the size of the random number in the thermal term of the Langevin equations. The functions for filament-membrane interaction potential as a function of gap r, and the resulting force from differentiation relative to r are given in lines 129-162. This is where we separate between the potentials of filaments at the center of the array and the ones in the surrounding band, to create the inhomogeneous actin polymerization. We named the central filaments "pullers", representing the attached filaments to the membrane via protein Sla2, and the others as "pushers", since they are in the region of activity for actin nucleators, so the actin filaments polymerize and push against the plasma membrane in this region. The potential profile for pushers is proportional to an exponential decay, a purely repulsive potential; the puller potentials have a well with typical depths of 5, 10, 25, or $50k_BT$. This depth can be controlled by adjusting the parameters in these two functions of Potential (line 129), and Force (line 146). We will discuss how multiple simultaneous simulations with different potential parameters can be set to run using this code as the core program.

Line 163: These lines are to set-up the MPI parameter tables for parallel computations that will take place on the multi-cored CPU.

Lines 165-192: Initialize the parallel computing environment. This segment can be kept as is for different jobs.

Lines 194-289: Define eight different sets of parameter values that are to be used in 8 different but simultaneous simulations, to be run on 8 different cores. This number 8 could be easily as high as 40; the number of simultaneous simulations, given the capacity of our processors at the time. In every set or table of parameters, the values are entered at the order from top to bottom (refer to comments in front of each line for parameters Id's).

Lines 297-307: Load the parameter values for each separate processor, which is responsible for computations with one particular set of parameter values. The parameters that are modified from run to run are, k_{elas} (gel stiffness identifier), t_{eq} (equilibrium time), four potential pre-factors defining the puller and pusher potentials, external load in pN, and the specific number to be used as seed number in generating the series of random numbers in a trackable way; so that in case we wanted to re-create a simulation, we know what seed number to be used for random number generators.

Lines 309-327: Create separate directories for each simulation, to store neatly, thousands of data files as output of each run. Text files for the positions, gaps, and forces of each individual filaments (144 filaments in a 12×12 array), in addition to the separate data files for averages and error bars. Keeping track of the resulting data and organizing them neatly, greatly helps to improve the simulations by interpreting the data from different perspectives and approaches. For example, accessing data for cross-examining of two plots at the same time is one important tool that is readily possible if one implements such lines in the code to store data for as many parameters as possible, in an organized, easily findable manner.

Lines 332-363: The *.txt* files for data to be written into are created. The argument "path" is required in the ofstream function, for compatibility with MPI parallel computings. "ofstream::app" is the argument necessary for files that contain the data for a particular quantity that needs to be saved at every time step, such as

averages vs. time.

Line 365: Define the random number generator (RNG). The specific RNG we chose for creating random numbers with more accuracy (more than 10^{10} different numbers between 0 and 1) was mt19937. For simpler stochastic treatments, such as random initial alignments of the filament heights, we used the common srand RNG. Every time we run the simulations with a fixed recorded seed number for random generators, to keep the simulations reproducible. For further studies on random number generators, I recommend the C++ online manual.

Lines 373-415: More initiation of arrays, some being 3D to store data from the entire array of filaments over all time steps. The loop in line 416 is particularly important, because of the initial values set for on- and off- rates of actin filament dynamics, based on the free-filament values reported from experiments. The real-time values are later modified at every time step based on the stochastic changes in filament-membrane gap. Separate puller and pusher sub-loops are assigned, although most parameter values are the same in most cases (in fact, all parameter values are similar for pushers and pullers, except potential pre-factors defined at the beginning in the MPI parameter table sets). Notice that the operations at each line repeat for all the filaments in each row and each column, but only once before entering the time-dependent iteration loops in the main function.

Lines 452-463: Generate large number of empty output text files to store data later for averaged parameters and error bars.

Lines 464-468: Set up the distribution functions for random numbers, which will be used later in stochastic calculations. The range defined in the distribution functions specifies the resolution of the randomness for the generated random numbers. The range $0 - 10^9$ means that between 0 and 1, the code creates a random number that is uniformly apart from any other number in the set with a distance at least 10^{-9}; a high-resolution uniform distribution. This is the capability of the mt19937 RNG among several others in C++ libraries, that worked well for the physical nature of this research problem, since it deals with stochastic thermal behaviors in the time scales of nano-seconds. The small changes in the time development of the system can

be simulated only with certain random number distributions, generated by RNGs precise enough for simulating physical phenomena that are highly stochastic on sub-molecular scales.

Lines 474-483: Define an important time iteration loop, to generate and store data at every $\frac{1}{limit}\%$ ($limit$ is defined in line 28) of the total duration of the simulation. The reason for this smaller nested loop inside the bigger time loop was to first break the entire volume of data into enough small segments to be able to generate valid error bars; and second to fit every calculation possible into the size of the biggest 2D array that we could possibly compile and run with the C++11 language. So, the bigger sizes for the loop in line 477 were problematic because the compiler would give us errors in regard to the size of the arrays that are to be filled. The maximum number allowed as size of a double array in C++11 is $\approx 2 \times 10^9$ elements.

Line 488: This line causes polymerization steps to be skipped to save time. The if condition with parameter ss, speeds up the simulations, considering the fact that polymerization steps take much longer to proceed compared with the stochastic steps for membrane position and filaments' tips and bases. So it is safe to do the calculations inside this if statement every 100 times that we do the other calculations in the main function outside of this statement, but with a probability 100 times larger.

Lines 489-588: The next few for loops until line 588 are all straightforward to follow line by line. They are calculating and applying the modifications in the positions of the obstacle, all 144 filaments' number of subunits, tip positions, and base positions, for every time step that iterates forward inside the loop of line 477.

Line 494: Define the range for the random numbers to be between 0 and 1, by dividing the random number over the range specified by RNG.

Line 502-513: Implement our k_{on} and k_{off} functions, using the parameters of lines 497-500.

Lines 518-525: Stochastic treatment of polymerization growth, subunit by subunit; implemented by the two if statements. We build the polymerization and depolymerization probability parameters before (lines 515-516) to compare their values to uniformly distributed random numbers (corrected for the speed-up parameter, ss).

This comparison decides the addition or elimination of one subunit, stochastically.

Lines 605-647: In the longer for loop of line 615, as mentioned before, we compute at every time step the value of S, the sum of the base displacements, for every filament relative to its adjacent filaments. For the filaments on the corners of the square lattice, the ones on the sides, and the inner ones the number of adjacent filaments vary. This is dissected into if and $else\_if$ sub-conditions, with the last $else$ term being the only part which computes S for all inner filaments.

Lines 658-669: The Langevin equations for filament tip and base positions are implemented. The if statement in lines 660-667 asserts the limits of tip fluctuations; bounded by filament height and orientation angles.

Line 724: Obstacle is moved according to the Langevin equation. z is the obstacle position.

Line 769: In this line, the time iteration loop is closed, and $\approx 10\%$ of the entire simulation is done. The remaining 90% is an exactly similar process, repeated 9 more times for the purpose of finding error bars.

Line 823: The entire time loop ends at the line 823 (more than 99.8% of the simulation run-time is over).

Lines 825-945: Calculating the averages and the error bars, and writing data in the assigned text files of-streamed before, plus commands for printing some information on the terminal for quick reviews and assessments at the beginning of each long-term run.

Note: MPI routine has to be finalized (MPI_Finalize(); has to be added - see line 126). This is analogous to return 0 for the main function in C++.

Chapter 5

Conclusions

In this thesis, we showed that the growth of biopolymer media, such as crosslinked actin filament networks, can lead to generation of large pushing and pulling forces, to facilitate the membrane bending required in many processes, against opposing forces from internal turgor pressure, membrane tension forces, and membrane curvature forces. The examples of cellular phenomena that require membrane bending as a result of large exerted forces from the actin network on the membrane, include the membrane trafficking signals and repairs, cell migrational protrusions, and clathrin-mediated endocytosis events. This thesis started with the discussion of the previous major observational and theoretical studies of pushing force generation, in a variety of *in vitro* and *in vivo* experiments, and relevant mathematical modeling efforts. This discussion showed that actin polymerization is required in many cell motility processes. This motivates the study of the dynamic behavior of the system of plasma membrane, actin network, and several other involved proteins in the endocytic machinery, using biased Brownian ratchet mechanism, with stochastic treatment of time evolutions of parameter values at every time step, and an elastic gel perspective towards the entire actin network.

We exploited this approach in our numerical calculations in Chapter 2, for the growth of a biopolymer under the effects of its interaction with a flat obstacle, represented either with a purely repulsive potential, or a potential with an attractive well to represent a molecular binding. The growth rate is plotted against the external load

on the surface of the obstacle for various interaction potentials. The force-velocity (FV) plots interestingly show that the interaction potentials that are purely repulsive (corresponding to growing filaments that on average only ever push against the obstacle) lead to a dynamic behavior that is very precisely modeled with modified Brownian ratchet models in the high obstacle diffusion constant regime. In other words, a pusher actin filament is slowed down with increasing force with a curve closely similar to the BR model. But for puller filaments, the ones which have interaction potentials with a well of typical depth of few tens of k_BT, the FV plots show rapid decline in growth velocity as force grows above zero. At the same time, substantial pulling forces exerted by a single puller (above ≈ 3 pN) can only be sustained for pullers with strong binding (typically wells deeper than $25k_BT$). Under such forces, they essentially stop growing. This requirement of strong filament-membrane binding to sustain large pulling forces becomes very important in our general picture provided with the multiple filament simulation results from Chapter 3.

Chapter 3 continues our effort to expand the thermodynamical framework that we worked with so far, to a model consisting a discreet square array of actin filaments, crosslinked with springs that allow them to move relative to each other in the direction normal to the obstacle. We asked questions such as how large of a pulling force can this network of crosslinked flexible actin filaments generate, under conditions governed by parameter values estimated from experiments? What is the distribution of these actin forces on the surface of the fluctuating two-dimensional flat obstacle? We studied the effect of various binding strengths in puller potentials on the growth of the ensemble of filaments. The resulting force distributions are consistent with the ones extracted from electron microscopy images of membrane deformation [50]. The specific pre-patterned ring distribution of actin nucleators on the surface of the membrane at the endocytic site, surrounding the central dot of filaments attached to the membrane via specific proteins, creates an inhomogeneous actin polymerization distribution across the membrane surface. This subsequently generates the central actin pulling force surrounded by the pushing force of the growing filaments. Pushing and pulling forces are in balance, due to the very small total drag force on the actin gel.

We studied the effect of actin gel stiffness on the magnitude and distribution of actin forces during simulations. The stiffness of the crosslinked actin gel is regulated by the spring constants of connectors between the neighboring filaments in the lattice. Softening the actin gel experimentally can be performed by decreasing the concentration of actin filament crosslinkers or mutating cells to knock out the crosslinking proteins. We find that by softening the gel, actin gel deforms more significantly, and a higher amount of actin is polymerized, but at the expense of higher chances for filament-membrane links to detach. The chance of detachment is lower for stiffer gels with stronger central binding. We found that the predictions of our simulations with a full system of puller and pusher filaments are consistent with the results of a mean-force model, confirming that the statistical details of force development are not significant in average force calculations. Our numerical results are calculated by assigning values to our model parameters (Table I in Chapter 3) coming from experimental data. We found that an array of actin filaments, without the assistance of curvature generating proteins or molecular motors such as myosin, can generate large total pulling forces, but insufficient to overcome the turgor pressure. With a simplified approach, we established a mathematical platform for calculation and visualization of dynamic behaviors in the process of endocytosis, that can be further improved by including the effect of additional mechanisms known to be influential on the force generation.

The most important factor missing from our simulations is Type-I myosin. It is observed that endocytic internalization in budding yeast requires Type-I myosin motor activity [120], consistent with our finding that actin polymerization is insufficient. We can ask how the myosin activity affect the force generation? How much of the additional force, presumably generated by the myosin motion and attachments, contribute to the pulling forces to bend the membrane inward in endocytosis? These questions can be investigated within the scope of our model, by representing myosin molecules as springs connecting actin filaments to the membrane, moving along the filaments. The motion of the myosin molecules along the actin filaments is driven by ATP hydrolysis. If the myosin is bound to filament and membrane both, its motion

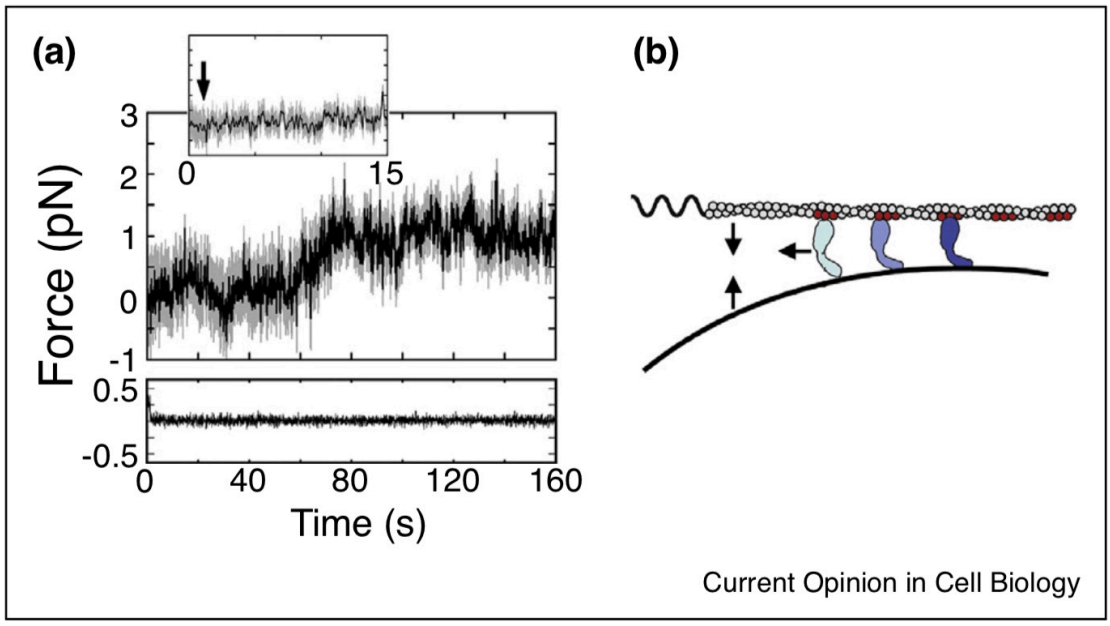

Figure 5.1: Leftward motion of Type-I myosin in frame b generates lateral pulling forces on the membrane. Experiments *in vitro* showed that forces in the order of 1 pN can be generated by myosin activity (frame a). Taken from Ref. [2].

generates lateral pulling forces on both the actin filament and the membrane, causing them to move towards each other in a zippering effect (Figure 5.1 right).

If myosin molecules move along the scaffold of the actin gel, while bound to the membrane at certain regions, the myosin motion can pull the membrane inward, given appropriate orientations [2]. Direct measurements showed that lateral forces of ≈ 1 pN are generated by membrane-bound Type-I myosin, parallel to a lipid bilayer (Figure 5.1) [2]. Larger myosin forces might be generated in cells, because membrane proteins might increase myosin frictional forces.

Myosin activity in the region of the pushing filaments could also enhance the actin polymerization rate. If a myosin molecule binds to the membrane and a pusher filaments' growing end simultaneously, given the right orientations, the myosin's pulling force on the filament could increase the gap between the filaments' growing end and the membrane (Figure 5.2), and thus maintain the polymerization rate against larger opposing forces. This mechanism by which myosin motors can enhance actin polymerization forces can be studied further within the scope of our model in this thesis.

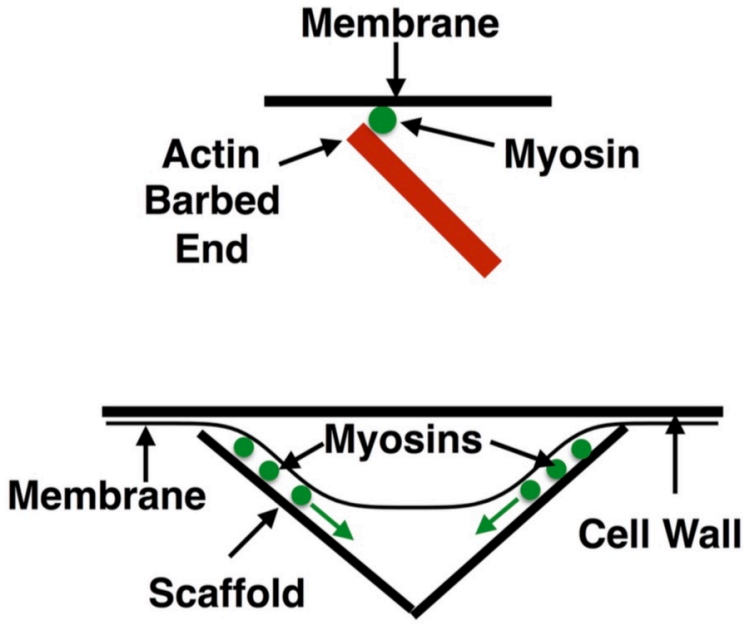

Figure 5.2: One hypothesis on myosin force generation mechanism is that type-I myosin moves along the actin filament towards the barbed end in proximity of the membrane, then it exerts forces on the membrane and filament to increase the gap for new actin subunits to polymerize. The image at the bottom shows how myosin can use actin network to exert forces on both actin filaments and the membrane with a "zippering" mechanism. Taken from Ref. [2].

Each individual myosin molecule can be treated in the simulations via a new stochastically changing entity, with its own gap-dependent force field in interaction with the membrane.

Curvature-generating proteins are also important for endocytosis, and should eventually be included in a complete model. However, the experiments of Ref. [48] showed that no invagination occurs before actin arrives. Therefore, we consider the Type-I myosin to be a higher priority than the curvature-generating proteins.

Appendices

Appendix A

Appendix of Chapter 2

Here we extend the results beyond the simplifying approximations made in the body of the paper, by including filament-tip fluctuations, oblique incidence, and slower diffusion.

A.1 Filament-tip fluctuations and oblique incidence

We treat oblique incidence together with filament-tip fluctuations, since these fluctuations are much greater at oblique incidence than at perpendicular incidence. We use an incidence angle of $\theta = 45^o$ as in Figure A.1. The filament-tip fluctuations are modeled by a variable z_{tip} describing the deflection of the tip, assumed to move according to Brownian dynamics in a quadratic potential well:

$$\Delta z_{tip} = \alpha' \sqrt{24 \Delta t} \sqrt{D_{tip}} + \frac{D_{tip}}{k_B T} \Delta t [-F(r) - k_{bend} \cdot z_{tip}] \tag{A.1}$$

Here $D_{tip} = 5 \times 10^4 \frac{nm^2}{sec} = 10 D_{obst}$ is the filament tip diffusion coefficient. The true value of D_{tip} is probably greater than this, since the part of the filament free to bend is much smaller than the $5\mu m$ obstacle that we consider. However, using the actual value would render the simulations extremely demanding. For this reason we have chosen a value an order of magnitude larger than D_{obst}, so that the tip fluctuations will equilibrate on time scales much faster than that of obstacle motion. The variation of the deflection z_{tip} is limited: the tip can not bend down past its

own base or up so far that its height from the base exceeds the filament length. The time step $\Delta t = 10^{-9} sec$ is is chosen so that filament tips will move much less than the subunit size in one time step. The tip bending stiffness k_{bend} is obtained [111] as $k_{bend} = 3k_BTL_p/L^3 \sin^2\theta = 0.5\ \frac{pN}{nm}$, where $L_p \simeq 20\mu m$ [112, ?] is the persistence length and L is the filament length, which we take to have a typical lamellipodium value of 100 nm. Finally α' is a random number uniformly distributed between $-\frac{1}{2}$ and $\frac{1}{2}$, so that $<\alpha'^2>=\frac{1}{12}$. Consecutive time steps are uncorrelated.

Figure A.2 shows the resulting force-velocity relation for different pusher and puller potentials described in Figure 2.2. Notice that the stall force is larger in this case because δ in Eq. 2.9 is replaced by $\delta\cos(\theta) = \delta/\sqrt{2}$. The BR relation remains an upper bound for the growth velocity, and the force-velocity relations for both the hard wall and soft walls are very similar to the BR relation. The $5k_BT$ well and spike potentials continue to have a zero-force velocity that is a substantial fraction of the free-filament velocity, with velocities decaying more rapidly than the BR prediction. In potentials with deep wells, the polymerization is slowed by roughly the same amount as in our baseline results (Figure 2.5). The tradeoff between polymerization rate and maximum sustainable pulling force is also preserved.

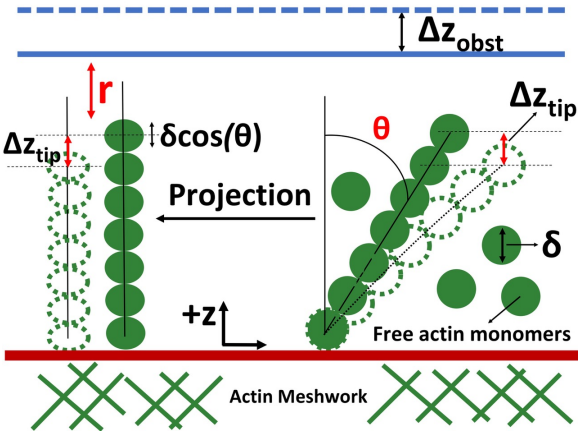

Figure A.1: Schematic of model of filament at oblique orientation with incident angle θ. Δz_{tip} the filament tip fluctuation.

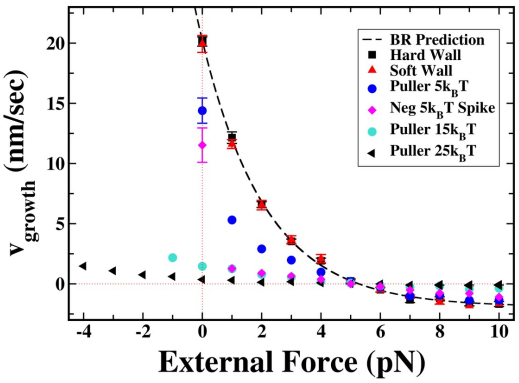

Figure A.2: Simulations of 20 seconds showing the force-velocity relation for different forms of filament-obstacle interaction potential for oblique filament orientation, including filament-tip fluctuations. Error bars are smaller than the symbols, except where indicated. The dashed line is the prediction of the BR model at large diffusion constant values for obstacle. Data points for pullers are shown out to forces where they detach from the obstacle in less than 20 sec.

A.2 Effect of slow obstacle diffusion

We have repeated the force-velocity relations for the oblique filament case (45° orientation, including filament-tip fluctuations) with a smaller diffusion coefficient to see which findings in the main text depend strongly on the assumption of rapid diffusion. Figure A.3 shows results for a diffusion coefficient of D =21 nm/s^2. For this value of D, the dimensionless parameter characterizing diffusion $\delta^2 k_{on}/2D_{obst}$ has the value unity, so the effects of diffusion should be substantial. The polymerization rate for the more rapidly growing potentials - including the "Hard Wall", the "Soft Wall", and the "Puller" with 5 k_BT well depth, is slowed by about a factor of 2. As in the main text, the completely repulsive continuous potentials have force-velocity relations similar to the hard wall. However, the sharp drop in velocity for the $5k_BT$ potentials is eliminated, as expected from the analysis of Sec. 3.2 showing that this effect depends on rapid diffusion. The effect on the other force-velocity relations for deeper wells is smaller. The general shape of the force-velocity is unchanged, and there is no effect on the ordering of the curves.

As Figure A.3 indicates, the effect of using a softer wall on the growth velocity

is minimal even when diffusion is slow. For a still softer wall with decay coefficient $\kappa_1 = 0.2$ nm^{-1} (data not shown), the acceleration is about 10%.

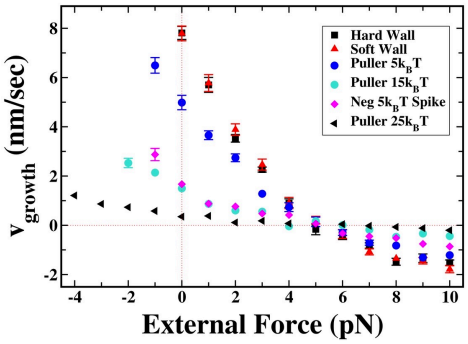

Figure A.3: Effect of reduced diffusion coefficient on force-velocity relation of growing actin filaments. Diffusion coefficient of D =21 nm/s^2. Force field parameters are as in Figure 2.5.

Bibliography

[1] B. L. Goode, J. A. Eskin, and B. Wendland, "Actin and endocytosis in budding yeast," *Genetics*, vol. 199, no. 2, pp. 315–358, 2015.

[2] A. E. Carlsson, "Membrane bending by actin polymerization," *Current opinion in cell biology*, vol. 50, pp. 1–7, 2018.

[3] S. Boulant, C. Kural, J.-C. Zeeh, F. Ubelmann, and T. Kirchhausen, "Actin dynamics counteract membrane tension during clathrin-mediated endocytosis," *Nature cell biology*, vol. 13, no. 9, p. 1124, 2011.

[4] S. Kaur, A. B. Fielding, G. Gassner, N. J. Carter, and S. J. Royle, "An unmet actin requirement explains the mitotic inhibition of clathrin-mediated endocytosis," *Elife*, vol. 3, p. e00829, 2014.

[5] D. Yarar, C. M. Waterman-Storer, and S. L. Schmid, "A dynamic actin cytoskeleton functions at multiple stages of clathrin-mediated endocytosis," *Molecular biology of the cell*, vol. 16, no. 2, pp. 964–975, 2005.

[6] S. Piccinotti, T. Kirchhausen, and S. P. Whelan, "Uptake of rabies virus into epithelial cells by clathrin-mediated endocytosis depends upon actin.," *Journal of virology*, pp. JVI–01648, 2013.

[7] D. K. Cureton, R. H. Massol, S. Saffarian, T. L. Kirchhausen, and S. P. Whelan, "Vesicular stomatitis virus enters cells through vesicles incompletely coated with clathrin that depend upon actin for internalization," *PLoS pathogens*, vol. 5, no. 4, p. e1000394, 2009.

[8] D. K. Cureton, R. H. Massol, S. P. Whelan, and T. Kirchhausen, "The length of vesicular stomatitis virus particles dictates a need for actin assembly during clathrin-dependent endocytosis," *PLoS pathogens*, vol. 6, no. 9, p. e1001127, 2010.

[9] S. Bedi and A. Ono, "Friend or foe: The role of the cytoskeleton in influenza a virus assembly," *Viruses*, vol. 11, no. 1, p. 46, 2019.

[10] R. D. Mullins, J. A. Heuser, and T. D. Pollard, "The interaction of arp2/3 complex with actin: nucleation, high affinity pointed end capping, and formation of branching networks of filaments," *Proceedings of the National Academy of Sciences*, vol. 95, no. 11, pp. 6181–6186, 1998.

[11] M. E. Young, J. A. Cooper, and P. C. Bridgman, "Yeast actin patches are networks of branched actin filaments," *The Journal of cell biology*, vol. 166, no. 5, pp. 629–635, 2004.

[12] C. S. Peskin, G. M. Odell, and G. F. Oster, "Cellular motions and thermal fluctuations: the brownian ratchet," *Biophysical journal*, vol. 65, no. 1, pp. 316–324, 1993.

[13] J. A. Theriot, "The polymerization motor," *Traffic*, vol. 1, no. 1, pp. 19–28, 2000.

[14] A. Mogilner, "On the edge: modeling protrusion," *Current opinion in cell biology*, vol. 18, no. 1, pp. 32–39, 2006.

[15] D. R. Kovar and T. D. Pollard, "Insertional assembly of actin filament barbed ends in association with formins produces piconewton forces," *Proceedings of the National Academy of Sciences*, vol. 101, no. 41, pp. 14725–14730, 2004.

[16] H.-C. Yang and L. A. Pon, "Actin cable dynamics in budding yeast," *Proceedings of the National Academy of Sciences*, vol. 99, no. 2, pp. 751–756, 2002.

[17] L. Blanchoin and T. D. Pollard, "Hydrolysis of atp by polymerized actin depends on the bound divalent cation but not profilin," *Biochemistry*, vol. 41, no. 2, pp. 597–602, 2002.

[18] J. Howard *et al.*, "Mechanics of motor proteins and the cytoskeleton," 2001.

[19] M. Dogterom and B. Yurke, "Measurement of the force-velocity relation for growing microtubules," *Science*, vol. 278, no. 5339, pp. 856–860, 1997.

[20] M. E. Janson, E. Mathilde, and M. Dogterom, "Dynamic instability of microtubules is regulated by force," *The Journal of cell biology*, vol. 161, no. 6, pp. 1029–1034, 2003.

[21] L. G. Tilney and D. A. Portnoy, "Actin filaments and the growth, movement, and spread of the intracellular bacterial parasite, listeria monocytogenes.," *The Journal of cell biology*, vol. 109, no. 4, pp. 1597–1608, 1989.

[22] M. J. Footer, J. W. Kerssemakers, J. A. Theriot, and M. Dogterom, "Direct measurement of force generation by actin filament polymerization using an optical trap," *Proceedings of the National Academy of Sciences*, vol. 104, no. 7, pp. 2181–2186, 2007.

[23] R. Wang and A. Carlsson, "Load sharing in the growth of bundled biopolymers," *New journal of physics*, vol. 16, no. 11, p. 113047, 2014.

[24] A. Perilli, C. Pierleoni, and J.-P. Ryckaert, "Filament flexibility enhances power transduction of f-actin bundles," *arXiv preprint arXiv:1806.08767*, 2018.

[25] A. Carlsson, "Growth velocities of branched actin networks," *Biophysical journal*, vol. 84, no. 5, pp. 2907–2918, 2003.

[26] S. H. Parekh, O. Chaudhuri, J. A. Theriot, and D. A. Fletcher, "Loading history determines the velocity of actin-network growth," *Nature cell biology*, vol. 7, no. 12, p. 1219, 2005.

[27] L. Blanchoin, R. Boujemaa-Paterski, C. Sykes, and J. Plastino, "Actin dynamics, architecture, and mechanics in cell motility," *Physiological reviews*, vol. 94, no. 1, pp. 235–263, 2014.

[28] F. Heinemann, H. Doschke, and M. Radmacher, "Keratocyte lamellipodial protrusion is characterized by a concave force-velocity relation," *Biophysical journal*, vol. 100, no. 6, pp. 1420–1427, 2011.

[29] Y. Marcy, J. Prost, M.-F. Carlier, and C. Sykes, "Forces generated during actin-based propulsion: a direct measurement by micromanipulation," *Proceedings of the National Academy of Sciences*, vol. 101, no. 16, pp. 5992–5997, 2004.

[30] M. Prass, K. Jacobson, A. Mogilner, and M. Radmacher, "Direct measurement of the lamellipodial protrusive force in a migrating cell," *J Cell Biol*, vol. 174, no. 6, pp. 767–772, 2006.

[31] A. Michelot, J. Berro, C. Guérin, R. Boujemaa-Paterski, C. J. Staiger, J.-L. Martiel, and L. Blanchoin, "Actin-filament stochastic dynamics mediated by adf/cofilin," *Current Biology*, vol. 17, no. 10, pp. 825–833, 2007.

[32] S. Romero, C. Le Clainche, D. Didry, C. Egile, D. Pantaloni, and M.-F. Carlier, "Formin is a processive motor that requires profilin to accelerate actin assembly and associated atp hydrolysis," *Cell*, vol. 119, no. 3, pp. 419–429, 2004.

[33] S. W. Moore, P. Roca-Cusachs, and M. P. Sheetz, "Stretchy proteins on stretchy substrates: the important elements of integrin-mediated rigidity sensing," *Developmental cell*, vol. 19, no. 2, pp. 194–206, 2010.

[34] L. Vonna, A. Wiedemann, M. Aepfelbacher, and E. Sackmann, "Micromechanics of filopodia mediated capture of pathogens by macrophages," *European Biophysics Journal*, vol. 36, no. 2, pp. 145–151, 2007.

[35] H. Kress, E. H. Stelzer, D. Holzer, F. Buss, G. Griffiths, and A. Rohrbach, "Filopodia act as phagocytic tentacles and pull with discrete steps and a load-

dependent velocity," *Proceedings of the National Academy of Sciences*, vol. 104, no. 28, pp. 11633–11638, 2007.

[36] M. J. Lehmann, N. M. Sherer, C. B. Marks, M. Pypaert, and W. Mothes, "Actin-and myosin-driven movement of viruses along filopodia precedes their entry into cells," *The Journal of cell biology*, vol. 170, no. 2, pp. 317–325, 2005.

[37] A. B. Bohil, B. W. Robertson, and R. E. Cheney, "Myosin-x is a molecular motor that functions in filopodia formation," *Proceedings of the National Academy of Sciences*, vol. 103, no. 33, pp. 12411–12416, 2006.

[38] F.-S. Wang, J. S. Wolenski, R. E. Cheney, M. S. Mooseker, and D. G. Jay, "Function of myosin-v in filopodial extension of neuronal growth cones," *Science*, vol. 273, no. 5275, pp. 660–663, 1996.

[39] A. Mogilner and G. Oster, "Cell motility driven by actin polymerization," *Biophysical journal*, vol. 71, no. 6, pp. 3030–3045, 1996.

[40] T. L. Hill and M. W. Kirschner, "Bioenergetics and kinetics of microtubule and actin filament assembly–disassembly," in *International review of cytology*, vol. 78, pp. 1–125, Elsevier, 1982.

[41] A. Mogilner and G. Oster, "Force generation by actin polymerization ii: the elastic ratchet and tethered filaments," *Biophysical journal*, vol. 84, no. 3, pp. 1591–1605, 2003.

[42] A. Carlsson, "Model of reduction of actin polymerization forces by atp hydrolysis," *Physical biology*, vol. 5, no. 3, p. 036002, 2008.

[43] L. A. Cameron, T. M. Svitkina, D. Vignjevic, J. A. Theriot, and G. G. Borisy, "Dendritic organization of actin comet tails," *Current Biology*, vol. 11, no. 2, pp. 130–135, 2001.

[44] P. A. Giardini, D. A. Fletcher, and J. A. Theriot, "Compression forces generated by actin comet tails on lipid vesicles," *Proceedings of the National Academy of Sciences*, vol. 100, no. 11, pp. 6493–6498, 2003.

[45] J. Taunton, B. A. Rowning, M. L. Coughlin, M. Wu, R. T. Moon, T. J. Mitchison, and C. A. Larabell, "Actin-dependent propulsion of endosomes and lysosomes by recruitment of n-wasp?," *The Journal of cell biology*, vol. 148, no. 3, pp. 519–530, 2000.

[46] S. Pistor, T. Chakraborty, U. Walter, and J. Wehland, "The bacterial actin nucleator protein acta of listeria monocytogenes contains multiple binding sites for host microfilament proteins," *Current biology*, vol. 5, no. 5, pp. 517–525, 1995.

[47] A. Proag, A. Bouissou, T. Mangeat, R. Voituriez, P. Delobelle, C. Thibault, C. Vieu, I. Maridonneau-Parini, and R. Poincloux, "Working together: spatial synchrony in the force and actin dynamics of podosome first neighbors," *ACS nano*, vol. 9, no. 4, pp. 3800–3813, 2015.

[48] W. Kukulski, M. Schorb, M. Kaksonen, and J. A. Briggs, "Plasma membrane reshaping during endocytosis is revealed by time-resolved electron tomography," *Cell*, vol. 150, no. 3, pp. 508–520, 2012.

[49] M. Mund, J. A. van der Beek, J. Deschamps, S. Dmitrieff, J. L. Monster, A. Picco, F. Nédélec, M. Kaksonen, and J. Ries, "Systematic nanoscale analysis of endocytosis links efficient vesicle formation to patterned actin nucleation," 2018.

[50] D. Tweten, P. Bayly, and A. Carlsson, "Actin growth profile in clathrin-mediated endocytosis," *Physical Review E*, vol. 95, no. 5, p. 052414, 2017.

[51] A. E. Carlsson and P. V. Bayly, "Force generation by endocytic actin patches in budding yeast," *Biophysical journal*, vol. 106, no. 8, pp. 1596–1606, 2014.

[52] S. Dmitrieff and F. Nédélec, "Membrane mechanics of endocytosis in cells with turgor," *PLoS computational biology*, vol. 11, no. 10, p. e1004538, 2015.

[53] X. Wang, B. J. Galletta, J. A. Cooper, and A. E. Carlsson, "Actin-regulator feedback interactions during endocytosis," *Biophysical journal*, vol. 110, no. 6, pp. 1430–1443, 2016.

[54] P. Bieling, S. D. Hansen, O. Akin, C. C. Hayden, D. A. Fletcher, R. D. Mullins, *et al.*, "Wh2 and proline-rich domains of wasp-family proteins collaborate to accelerate actin filament elongation," *The EMBO journal*, p. e201797039, 2017.

[55] M. Yu, X. Yuan, C. Lu, S. Le, R. Kawamura, A. K. Efremov, Z. Zhao, M. M. Kozlov, M. Sheetz, A. Bershadsky, *et al.*, "mdia1 senses both force and torque during f-actin filament polymerization," *Nature communications*, vol. 8, no. 1, p. 1650, 2017.

[56] M. Kaksonen, Y. Sun, and D. G. Drubin, "A pathway for association of receptors, adaptors, and actin during endocytic internalization," *Cell*, vol. 115, no. 4, pp. 475–487, 2003.

[57] C. M. Waterman-Storer, J. Gregory, S. F. Parsons, and E. Salmon, "Membrane/microtubule tip attachment complexes (tacs) allow the assembly dynamics of plus ends to push and pull membranes into tubulovesicular networks in interphase xenopus egg extracts.," *The Journal of Cell Biology*, vol. 130, no. 5, pp. 1161–1169, 1995.

[58] F. Perez, G. S. Diamantopoulos, R. Stalder, and T. E. Kreis, "Clip-170 highlights growing microtubule ends in vivo," *Cell*, vol. 96, no. 4, pp. 517–527, 1999.

[59] A. Mogilner and L. Edelstein-Keshet, "Regulation of actin dynamics in rapidly moving cells: a quantitative analysis," *Biophysical journal*, vol. 83, no. 3, pp. 1237–1258, 2002.

[60] E. Atilgan, D. Wirtz, and S. X. Sun, "Morphology of the lamellipodium and organization of actin filaments at the leading edge of crawling cells," *Biophysical journal*, vol. 89, no. 5, pp. 3589–3602, 2005.

[61] A. Mogilner and B. Rubinstein, "The physics of filopodial protrusion," *Biophysical journal*, vol. 89, no. 2, pp. 782–795, 2005.

[62] B. Rubinstein, K. Jacobson, and A. Mogilner, "Multiscale two-dimensional modeling of a motile simple-shaped cell," *Multiscale Modeling & Simulation*, vol. 3, no. 2, pp. 413–439, 2005.

[63] A. F. Marée, A. Jilkine, A. Dawes, V. A. Grieneisen, and L. Edelstein-Keshet, "Polarization and movement of keratocytes: a multiscale modelling approach," *Bulletin of mathematical biology*, vol. 68, no. 5, pp. 1169–1211, 2006.

[64] J. A. Ditlev, N. M. Vacanti, I. L. Novak, and L. M. Loew, "An open model of actin dendritic nucleation," *Biophysical journal*, vol. 96, no. 9, pp. 3529–3542, 2009.

[65] J.-F. Joanny and J. Prost, "Active gels as a description of the actin-myosin cytoskeleton," *HFSP journal*, vol. 3, no. 2, pp. 94–104, 2009.

[66] V. Khamviwath, J. Hu, and H. G. Othmer, "A continuum model of actin waves in dictyostelium discoideum," *PloS one*, vol. 8, no. 5, p. e64272, 2013.

[67] B. A. Camley, Y. Zhao, B. Li, H. Levine, and W.-J. Rappel, "Crawling and turning in a minimal reaction-diffusion cell motility model: coupling cell shape and biochemistry," *Physical Review E*, vol. 95, no. 1, p. 012401, 2017.

[68] J. Zimmermann, C. Brunner, M. Enculescu, M. Goegler, A. Ehrlicher, J. Käs, and M. Falcke, "Actin filament elasticity and retrograde flow shape the force-velocity relation of motile cells," *Biophysical journal*, vol. 102, no. 2, pp. 287–295, 2012.

[69] A. Carlsson, "Force-velocity relation for growing biopolymers," *Physical Review E*, vol. 62, no. 5, p. 7082, 2000.

[70] N. Burroughs and D. Marenduzzo, "Three-dimensional dynamic monte carlo simulations of elastic actin-like ratchets," *The Journal of chemical physics*, vol. 123, no. 17, p. 174908, 2005.

[71] N. J. Burroughs and D. Marenduzzo, "Growth of a semi-flexible polymer close to a fluctuating obstacle: application to cytoskeletal actin fibres and testing of ratchet models," *Journal of Physics: Condensed Matter*, vol. 18, no. 14, p. S357, 2006.

[72] E. J. Banigan, K.-C. Lee, and A. J. Liu, "Control of actin-based motility through localized actin binding," *Physical biology*, vol. 10, no. 6, p. 066004, 2013.

[73] R. B. Dickinson and D. L. Purich, "Clamped-filament elongation model for actin-based motors," *Biophysical Journal*, vol. 82, no. 2, pp. 605–617, 2002.

[74] R. B. Dickinson, L. Caro, and D. L. Purich, "Force generation by cytoskeletal filament end-tracking proteins," *Biophysical journal*, vol. 87, no. 4, pp. 2838–2854, 2004.

[75] J. Zhu and A. Carlsson, "Growth of attached actin filaments," *The European Physical Journal E: Soft Matter and Biological Physics*, vol. 21, no. 3, pp. 209–222, 2006.

[76] G. L. Ryan, D. Holz, S. Yamashiro, D. Taniguchi, N. Watanabe, and D. Vavylonis, "Cell protrusion and retraction driven by fluctuations in actin polymerization: A two-dimensional model," *Cytoskeleton*, vol. 74, no. 12, pp. 490–503, 2017.

[77] E. M. Craig, D. Van Goor, P. Forscher, and A. Mogilner, "Membrane tension, myosin force, and actin turnover maintain actin treadmill in the nerve growth cone," *Biophysical journal*, vol. 102, no. 7, pp. 1503–1513, 2012.

[78] Y. Adler and S. Givli, "Closing the loop: Lamellipodia dynamics from the perspective of front propagation," *Physical Review E*, vol. 88, no. 4, p. 042708, 2013.

[79] E. L. Barnhart, J. Allard, S. S. Lou, J. A. Theriot, and A. Mogilner, "Adhesion-dependent wave generation in crawling cells," *Current Biology*, vol. 27, no. 1, pp. 27–38, 2017.

[80] M. Doi and S. F. Edwards, *The theory of polymer dynamics*, vol. 73. oxford university press, 1988.

[81] A. Mogilner and G. Oster, "The polymerization ratchet model explains the force-velocity relation for growing microtubules," *European Biophysics Journal*, vol. 28, no. 3, pp. 235–242, 1999.

[82] G. S. van Doorn, C. Tănase, B. M. Mulder, and M. Dogterom, "On the stall force for growing microtubules," *European Biophysics Journal*, vol. 29, no. 1, pp. 2–6, 2000.

[83] J. Son, G. Orkoulas, and A. B. Kolomeisky, "Monte carlo simulations of rigid biopolymer growth processes," *The Journal of chemical physics*, vol. 123, no. 12, p. 124902, 2005.

[84] J. Krawczyk and J. Kierfeld, "Stall force of polymerizing microtubules and filament bundles," *EPL (Europhysics Letters)*, vol. 93, no. 2, p. 28006, 2011.

[85] T. L. Hill, *Linear aggregation theory in cell biology*. Springer Science & Business Media, 2012.

[86] T. D. Pollard, "Rate constants for the reactions of atp-and adp-actin with the ends of actin filaments.," *The Journal of cell biology*, vol. 103, no. 6, pp. 2747–2754, 1986.

[87] A. E. Carlsson, "Growth of branched actin networks against obstacles," *Biophysical journal*, vol. 81, no. 4, pp. 1907–1923, 2001.

[88] T. E. Schaus, E. W. Taylor, and G. G. Borisy, "Self-organization of actin filament orientation in the dendritic-nucleation/array-treadmilling model," *Proceedings of the National Academy of Sciences*, vol. 104, no. 17, pp. 7086–7091, 2007.

[89] T. E. Schaus and G. G. Borisy, "Performance of a population of independent filaments in lamellipodial protrusion," *Biophysical journal*, vol. 95, no. 3, pp. 1393–1411, 2008.

[90] L. Hu and G. A. Papoian, "Mechano-chemical feedbacks regulate actin mesh growth in lamellipodial protrusions," *Biophysical journal*, vol. 98, no. 8, pp. 1375–1384, 2010.

[91] J. Zhu and A. Mogilner, "Mesoscopic model of actin-based propulsion," *PLoS computational biology*, vol. 8, no. 11, p. e1002764, 2012.

[92] L. Hu and G. A. Papoian, "Molecular transport modulates the adaptive response of branched actin networks to an external force," *The Journal of Physical Chemistry B*, vol. 117, no. 42, pp. 13388–13396, 2013.

[93] M. M. Kozlov and A. D. Bershadsky, "Processive capping by formin suggests a force-driven mechanism of actin polymerization," *J Cell Biol*, vol. 167, no. 6, pp. 1011–1017, 2004.

[94] H. Kubota, M. Miyazaki, T. Ogawa, T. Shimozawa, K. Kinosita Jr, and S. Ishiwata, "Biphasic effect of profilin impacts the formin mdia1 force-sensing mechanism in actin polymerization," *Biophysical journal*, vol. 113, no. 2, pp. 461–471, 2017.

[95] D. Bryant, L. Clemens, and J. Allard, "Computational simulation of formin-mediated actin polymerization predicts homologue-dependent mechanosensitivity," *Cytoskeleton*, vol. 74, no. 1, pp. 29–39, 2017.

[96] N. Courtemanche, J. Y. Lee, T. D. Pollard, and E. C. Greene, "Tension modulates actin filament polymerization mediated by formin and profilin," *Proceedings of the National Academy of Sciences*, vol. 110, no. 24, pp. 9752–9757, 2013.

[97] L. Cao, M. Kerleau, E. L. Suzuki, H. Wioland, S. Jouet, B. Guichard, M. Lenz, G. Romet-Lemonne, and A. Jegou, "Modulation of formin processivity by profilin and mechanical tension," *Elife*, vol. 7, p. e34176, 2018.

[98] J. S. Kim and S. X. Sun, "Continuum modeling of forces in growing viscoelastic cytoskeletal networks," *Journal of theoretical biology*, vol. 256, no. 4, pp. 596–606, 2009.

[99] J. Mueller, G. Szep, M. Nemethova, I. de Vries, A. D. Lieber, C. Winkler, K. Kruse, J. V. Small, C. Schmeiser, K. Keren, *et al.*, "Load adaptation of lamellipodial actin networks," *Cell*, vol. 171, no. 1, pp. 188–200, 2017.

[100] L. Radoshevich and P. Cossart, "Listeria monocytogenes: towards a complete picture of its physiology and pathogenesis," *Nature Reviews Microbiology*, vol. 16, no. 1, p. 32, 2018.

[101] A. Upadhyaya, J. R. Chabot, A. Andreeva, A. Samadani, and A. van Oudenaarden, "Probing polymerization forces by using actin-propelled lipid vesicles," *Proceedings of the National Academy of Sciences*, vol. 100, no. 8, pp. 4521–4526, 2003.

[102] A. Picco, W. Kukulski, H. E. Manenschijn, T. Specht, J. A. Briggs, and M. Kaksonen, "The contributions of the actin machinery to endocytic membrane bending and vesicle formation," *Molecular biology of the cell*, vol. 29, no. 11, pp. 1346–1358, 2018.

[103] S. Aghamohammadzadeh and K. R. Ayscough, "Differential requirements for actin during yeast and mammalian endocytosis," *Nature cell biology*, vol. 11, no. 8, p. 1039, 2009.

[104] G. Danuser, J. Allard, and A. Mogilner, "Mathematical modeling of eukaryotic cell migration: insights beyond experiments," *Annual review of cell and developmental biology*, vol. 29, pp. 501–528, 2013.

[105] T. D. Pollard, "Mechanics of cytokinesis in eukaryotes," *Current opinion in cell biology*, vol. 22, no. 1, pp. 50–56, 2010.

[106] R. Basu, E. L. Munteanu, and F. Chang, "Role of turgor pressure in endocytosis in fission yeast," *Molecular biology of the cell*, vol. 25, no. 5, pp. 679–687, 2014.

[107] F. Motahari and A. Carlsson, "The effect of the filament-obstacle interaction on the force-velocity relation of a growing biopolymer," *arXiv preprint arXiv:1812.00061*, 2018.

[108] J. Zimmermann, M. Enculescu, and M. Falcke, "Leading-edge–gel coupling in lamellipodium motion," *Physical Review E*, vol. 82, no. 5, p. 051925, 2010.

[109] J. L. McGrath, Y. Tardy, C. Dewey Jr, J. Meister, and J. Hartwig, "Simultaneous measurements of actin filament turnover, filament fraction, and monomer diffusion in endothelial cells," *Biophysical journal*, vol. 75, no. 4, pp. 2070–2078, 1998.

[110] B. J. Galletta, A. E. Carlsson, and J. A. Cooper, "Molecular analysis of arp2/3 complex activation in cells," *Biophysical journal*, vol. 103, no. 10, pp. 2145–2156, 2012.

[111] B. Lautrup, "Physics of continuous matter," *Exotic and Everyday Phenomena in the Macroscopic World, IOP.*, 2005. We evaluated Eq. (10.12) of this reference at the end of the rod ($|z| = L$), and used the relationship $EI = k_B T L_p$, to obtain the formula for k_{bend}.

[112] F. Gittes, B. Mickey, J. Nettleton, and J. Howard, "Flexural rigidity of microtubules and actin filaments measured from thermal fluctuations in shape.," *The Journal of cell biology*, vol. 120, no. 4, pp. 923–934, 1993.

[113] L. D. Landau and E. M. Lifshitz, "Theory of elasticity (in russian)," 1965.

[114] I. S. Gradshteyn and I. M. Ryzhik, *Table of integrals, series, and products*. Academic press, 2014.

[115] K. Kim, A. Yamashita, M. A. Wear, Y. Maéda, and J. A. Cooper, "Capping protein binding to actin in yeast: biochemical mechanism and physiological relevance," *J Cell Biol*, vol. 164, no. 4, pp. 567–580, 2004.

[116] P. Bieling, S. D. Hansen, O. Akin, C. C. Hayden, D. A. Fletcher, R. D. Mullins, *et al.*, "Wh2 and proline-rich domains of wasp-family proteins collaborate to accelerate actin filament elongation," *The EMBO journal*, vol. 37, no. 1, pp. 102–121, 2018.

[117] P. Hänggi, P. Talkner, and M. Borkovec, "Reaction-rate theory: fifty years after kramers," *Reviews of modern physics*, vol. 62, no. 2, p. 251, 1990.

[118] R. Thomson, "Physics of fracture," in *Solid state physics*, vol. 39, pp. 1–129, Elsevier, 1986.

[119] M. Skruzny, T. Brach, R. Ciuffa, S. Rybina, M. Wachsmuth, and M. Kaksonen, "Molecular basis for coupling the plasma membrane to the actin cytoskeleton during clathrin-mediated endocytosis," *Proceedings of the National Academy of Sciences*, vol. 109, no. 38, pp. E2533–E2542, 2012.

[120] Y. Sun, A. C. Martin, and D. G. Drubin, "Endocytic internalization in budding yeast requires coordinated actin nucleation and myosin motor activity," *Developmental cell*, vol. 11, no. 1, pp. 33–46, 2006.